Presynaptic structure-function relationships at the vertebrate neuromuscular junction

by

Anne E. Homan

Bachelor of Science, Allegheny College, 2013

Submitted to the Graduate Faculty of the

Kenneth P. Dietrich School of Arts and Sciences in partial fulfillment

of the requirements for the degree of

Master of Science

University of Pittsburgh

2019

UNIVERSITY OF PITTSBURGH

DIETRICH SCHOOL OF ARTS AND SCIENCES

This thesis was presented

by

Anne E. Homan

It was defended on

May 9, 2019

and approved by

Brian M. Davis, Professor, Neurobiology

Anne-Marie Oswald, Associate Professor, Neuroscience

Thesis Advisor: Stephen D. Meriney, Professor, Neuroscience

Presynaptic structure-function relationships at the vertebrate neuromuscular junction

Anne E. Homan, MS

University of Pittsburgh, 2019

The impact of presynaptic transmitter release site organization on synaptic function has been a vibrant area of research for synaptic physiologists. Because there is a highly nonlinear relationship between presynaptic calcium influx and subsequent neurotransmitter release at synapses, the organization and density of calcium sources (voltage-gated calcium channels [VGCCs]) relative to calcium sensors located on synaptic vesicles is predicted to play a major role in shaping the dynamics of neurotransmitter release at a synapse. Here we investigate neurotransmitter release at the neuromuscular junction across model preparations in an effort to discern the relationship between VGCC organization and synaptic function. We demonstrate that neurotransmitter release varies considerably across, but not within, individual synapses at the frog and mouse neuromuscular junction (NMJ). Further, we use a computational modeling approach to provide evidence that alterations in the spatiotemporal calcium dynamics within an AZ at the time of release, caused by manipulations in the density and organization of VGCCs, can explain variability in release. In addition, we use our model to demonstrate that VGCC organization is an important determinant of short-term plasticity, and that the differences in AZ arrangement between species can recapitulate the physiological differences between them. We use these studies to provide support for the notion that structure imparts function and argue that a fuller understanding of neurotransmitter release and plasticity must rely on an understanding of the spatio-temporal calcium dynamics at the time of vesicle release.

Table of Contents

List of Tables

List of Figures

1.0 Introduction[1]

The neuromuscular junction (NMJ), the site of contact between presynaptic motoneurons and postsynaptic muscle fibers, has been a historically important preparation for the study of presynaptic neurotransmitter release due to its stereotypical structure and peripheral accessibility for experimental study (Atwood and Karunanithis, 2002). The presence of hundreds of well-organized release sites, or active zones (AZs), has driven investigators to characterize the density and organization of different proteins involved in the process of neurotransmitter release, with a particular focus on voltage-gated calcium channels (VGCCs). As there is a highly nonlinear relationship between extracellular calcium concentration and subsequent neurotransmitter release at the NMJ (Dodge and Rahmimoff, 1967), the stoichiometry and localization of VGCCs relative to release sensors on synaptic vesicles is expected to have a large impact on the spatio-temporal calcium dynamics and subsequent neurotransmitter release.

Despite a high level of conservation of AZ proteins and VGCCs from lower order organisms to humans (Hadley et al., 2006), the dynamics of neurotransmitter release across different model systems are considerably diverse. Even within a single species, neurotransmitter release is heterogeneous, with differences observed from synapse to synapse within the same muscle, as well across different muscle-nerve preparations. Strikingly, the structure of AZs, particularly the spatial arrangement of VGCCs relative to synaptic vesicles, is quite diverse across

[1] This chapter was published as: Homan AE, Meriney SD. Active zone structure-function relationships at the neuromuscular junction. *Synapse* 72, 2018. Reproduced with permission of John Wiley & Sons, Inc.

species (Zhai and Bellen, 2004), raising the possibility that the AZ structure across different species is evolutionarily tuned to support the dynamics of neurotransmitter release required for appropriate function within that organism and at each particular synapse. This review will compare AZ structure across three different NMJ preparations in an effort to determine to what extent the organization of VGCCs and release sensors can explain unique functional characteristics. While there are numerous other mechanisms that influence synaptic function, we have focused this review exclusively on the impact of AZ structure-function relationships.

1.1 The Crayfish NMJ

At the adult crayfish NMJ, a large number of studies have used the limb opener muscle to investigate presynaptic physiology and structure-function relationships. This muscle receives both excitatory and inhibitory inputs, with multiple synapses onto each individual muscle fiber. This review will focus on the excitatory inputs, of which there can be several types, including phasic (stronger synapses that fire in short bursts of activity) and tonic (generally weaker and fire more consistently Bradacs et al., 1997; Wu and Cooper, 2010). Unlike the frog or mouse NMJ, which will be discussed in detail below, at the crayfish NMJ the presynaptic motoneuron makes multiple small contacts with the postsynaptic muscle fiber, rather than one large contact or endplate (Cooper and Cooper, 2009; Jahromi and Atwood, 1974, see Fig. 1.1). Each of these small contacts contain multiple characteristic electron dense regions (termed “dense bodies”) in the presynapse indicative of neurotransmitter release sites (termed “active zones” by Couteaux and Pécot-Dechavassine based on similar observations at the frog NMJ, 1974). Using freeze fracture techniques, investigators observed clusters and longitudinal arrangements of intramembranous particles on the

edges of the dense body (Jahromi and Atwood, 1974). These arrangements were found similarly across the two types of motoneurons with approximately 30 particles for every 10,000 nm^2 of AZ area (Govind et al, 1994; Fig. 1.1).

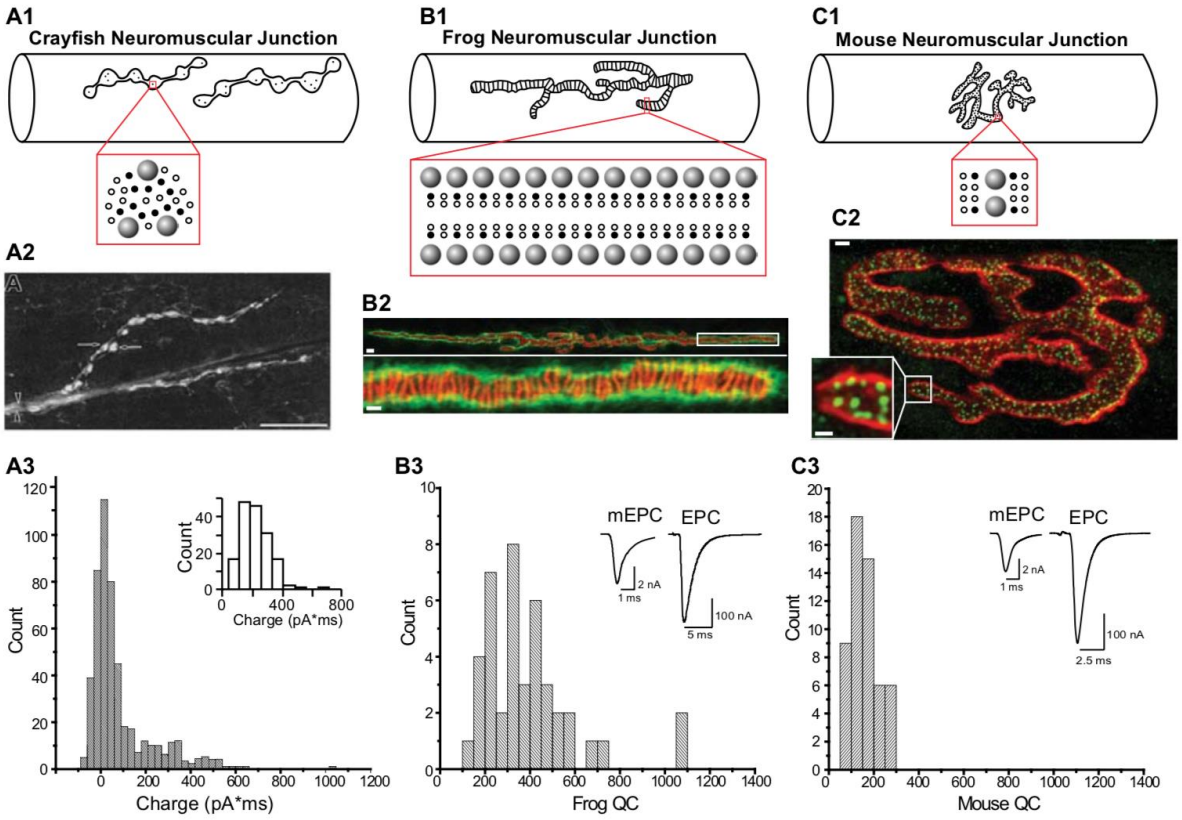

Figure 1.1 Schematics representing the neuromuscular junction structure of three model preparations.

(A1) At the crayfish NMJ, the presynaptic motor neuron makes multiple small synapses onto the postsynaptic muscle fiber. Each synapse contains few AZs (denoted by black dots). Within a single AZ (see red box) VGCCs have a clustered arrangement around synaptic vesicles, each vesicle associated with several VGCCs. (A2) A crayfish motoneuron stained with 4-Di-2-Asp to label varicosities. Adapted from Cooper et al., 1996. (A3) Quantal content calculated from charge transfer measurements recorded from a single bouton. Inset shows distributions of spontaneous events. Adapted from Cooper et al., 1995. (B1) At the frog NMJ, the presynaptic motor neuron makes one large contact onto the postsynaptic muscle fiber. This synapse contains hundreds of AZs (denoted by black stripes). Within a single

AZ (see red box), VGCCs and synaptic vesicles are well organized into a linear arrangement with each synaptic vesicle having one closely associated VGCC. (B2) Confocal image showing peanut lectin (PNA) labeling of synaptic extracellular matrix (green) and α-bungarotoxin (BTX) labeling of postsynaptic muscle acetylcholine receptors (red). At this synapse, postsynaptic receptors directly colocalize with presynaptic AZs; therefore, the BTX signal is a reliable indicator of AZs. (B3) Distribution of quantal content recorded from synapses at the frog NMJ. Inset shows representative spontaneous and evoked electrophysiological traces. B2 and B3 adapted from Laghaei et al., 2018. (C1) At the mouse NMJ, the presynaptic motor neuron makes one large synapse onto the postsynaptic muscle fiber and contains hundreds of AZs (denoted by black dots). Within a single AZ, VGCCs are organized in a bilateral arrangement relative to synaptic vesicles, each synaptic vesicle with two closely associated VGCCs. For each AZ schematic, large spherical structures represent synaptic vesicles, small filled circles represent VGCCs, and small unfilled circles represent possible locations for VGCCs or other ion channels. (C2) Confocal image of presynaptic AZs labeled with an antibody against bassoon to label presynaptic AZs (green), and BTX to label postsynaptic acetylcholine receptors (red). (C3) Distribution of quantal content recorded from synapses at the mouse NMJ, inset shows representative spontaneous and evoked electrophysiological traces. C2 and C3 adapted from Laghaei et al., 2018.

1.1.1 How many VGCCs contribute to vesicle fusion at the crayfish NMJ?

Neurotransmitter release at the crayfish NMJ is primarily triggered by P/Q type VGCCs (Allana and Lin, 2004; Araque et al., 1994; Wright et al., 1996) with the estimated total number of VGCCs to be on the order of 13 channels per release site. The number of docked synaptic vesicles per release site is estimated to average ~6–7, yielding ~1-2 VGCCs per synaptic vesicle (Cooper et al., 1996; Cooper et al., 1996). Further, investigators found that if the distance between VGCCs and synaptic vesicles was small, a single VGCC was sufficient to trigger release in simulated crayfish NMJ AZs (Kennedy et al., 1999). These data are in line with the notion that at synapses like the NMJ which require high temporal fidelity (“fast” synapses), release is largely gated by a

single VGCC ("single domain gating," see Stanley, 2016 for a comprehensive review). Note that this is a different definition of "fast" synapses than the "fast" and "slow" descriptors used to describe phasic and tonic synapses at this preparation (Bradacs et al., 1997; Wu and Cooper, 2010). In contrast, Kennedy et al. (1999) suggested that individual VGCC openings during an action potential at this synapse likely do not contribute productively towards release, but instead add to the intracellular calcium concentration which collectively triggers release. Whether the crayfish NMJ utilizes single or multi-domain gating (release triggered by the calcium ions from several nearby channels), remains to be resolved.

1.1.2 Variability in synaptic strength at the crayfish NMJ

The magnitude of neurotransmitter release across a single motoneuron axon is quite variable at the crayfish NMJ, with proximal regions releasing more neurotransmitter than distal regions (Cooper, Harrington et al., 1996; Cooper et al., 1995; Parnas et al., 1982). Investigators used electron microscopy to demonstrate that this variability in synaptic strength correlated with the number of dense bodies or bars, with proximal synapses having a greater number and longer dense bars than distal regions (Govind et al., 1994). As these dense bars are believed to represent AZs, these data suggest that the strong proximal regions have a higher density and larger AZs which could contribute to the increased strength (Govind et al., 1995). Further, since intramembranous particles (believed to be putative VGCCs, Pumplin et al., 1981) associate with these dense bars (Govind et al., 1994), investigators speculated that the strong proximal synapses could have more VGCCs, or that there is a closer association between VGCCs and release machinery (Govind et al., 1994).

Within a single synapse at the crayfish NMJ, there can be one or several individual AZs (Govind et al., 1994; Jahromi and Atwood, 1974). At synapses with more than one release site,

researchers observed a range of separation distances between these AZs, with distances as small as 50 nm and sizes as large as 160 nm in diameter. Further, they proposed that nearby AZs could "cross-talk," such that calcium influx at one AZ could diffuse to and contribute to vesicular release at a neighboring AZ (Cooper et al., 1996). Variability in AZ spacing and the degree of cross-talk could serve as a potential explanation for the large variability in quantal content across different synapses at this preparation (Cooper et al., 1996). Consistent with this hypothesis, stronger, phasic terminals have more AZs per synapse than weaker tonic terminals, and AZs are more tightly clustered (King et al., 1996). These data suggest that beyond VGCC organization and density, lateral interaction of AZs could also be a mechanism underlying varying synaptic strengths (Cooper et al., 1996).

Variability in AZ size was also demonstrated to underlie differences in neurotransmitter release across different motoneurons innervating the same postsynaptic muscle fiber. Crayfish muscle fibers can be innervated by two excitatory neurons—one phasic and one tonic (Govind and Pearce, 2003). Phasic terminals release more transmitter than their tonic counterparts, larger AZs, and proportionately more intramembranous particles. However, the size difference is not sufficient to explain the magnitude of variability in release across these two types of synapses (King et al., 1996; Msghina et al, 1998). Interestingly, Msghina et al., (1999) found that AZs at tonic and phasic terminals were of similar size and had comparable numbers of intramembranous particles (interpreted to be proportional to the number of VGCCs), but found that the terminal calcium influx at tonic terminals was larger. The authors ascribed this seemingly contradictory small calcium influx and large magnitude of release at phasic terminals to a greater sensitivity of release machinery to calcium. Further, they were unable to discern differences in the organization of intramembranous particles between the two types of synapses and thus argued that the organization

of ion channels was similar across phasic and tonic synapses (Msghina et al., 1999). However, without knowing precisely which of the particles were VGCCs and their relation to synaptic vesicles, it is difficult to rule out differences in VGGC density and/or organization between synapses. Overall, these data suggest that the magnitude of release could positively correlate with the density of VGCCs and their distance from synaptic vesicles at AZs, although the data are somewhat contradictory.

1.1.3 Short-term synaptic plasticity at the crayfish NMJ

The crayfish NMJ has been an important preparation for studying short-term synaptic plasticity (STP), as inputs onto the same postsynaptic muscle fiber can exhibit distinctive STP characteristics. Tonic terminals display a high degree of short-term facilitation with high-frequency stimulation while phasic terminals tend to depress (Bradacs et al., 1997). Given that phasic terminals are stronger than tonic terminals, the attenuated facilitation observed in phasic terminals could be due to their higher probability of release. These data were placed into context by Pan and Zucker (2009) who proposed a generalized model for relating the strength of synapses with their STP characteristics. Strong synapses, like those on phasic terminals tended to release more transmitter and depress during high-frequency stimulation while weak synapses, like those on tonic terminals tended to facilitate.

In exploring the sub-active zone mechanisms that could lead to these differences in STP, one can use the generalizing principle proposed by Pan and Zucker (2009), which would lead to the hypothesis that facilitating synapses likely have a lower probability of release and smaller AZs with fewer intramembranous particles. However, others have suggested that the organization of

AZs does not influence changes in strength or plasticity (Msghina et al., 1999), but that a difference in the sensitivity to calcium underlies these functional differences. A mechanism that could account for this difference in sensitivity to calcium is a different release sensor, an idea that gained traction at the crayfish NMJ (Yamada and Zucker, 1992). Early in the study of STP at this synapse, some raised the notion that facilitation was due to an accumulation of free calcium ions over successive stimuli that potentiated later responses in the train (Kamiya and Zucker, 1994). However, when imaging presynaptic calcium entry during successive stimuli, investigators found that each calcium transient appeared roughly similar (Tank, Regehr, & Delaney, 1995). While these data suggest that residual free calcium is likely not the mechanism for short-term facilitation at the crayfish NMJ, other hypotheses suggest residual calcium slowly-unbinding from vesicle (Blundon et al., 1993; Matveev et al., 2006) or an entirely separate "facilitation sensor" with different binding kinetics than the evoked release sensor (Yamada and Zucker, 1992). Therefore, differences in STP at the crayfish NMJ could be due in part to differences in expression of release sensors. In fact, recent work has identified synaptotagmin-7 (syt-7) as the putative facilitation sensor (Jackman and Regehr, 2017); however, a thorough investigation of syt-7 (or similar orthologues) has not been conducted at the crayfish NMJ.

1.2 The frog NMJ

The frog (*Rana pipiens*) NMJ has a distinct organization as compared to the crayfish NMJ. Rather than many small contacts, presynaptic frog motoneurons make a single large contact on the postsynaptic muscle cell (see Fig. 1.1). This contact, or endplate, contains hundreds of individual AZs spaced at regular intervals (Heuser et al., 1979; Pawson et al., 1998). However, unlike the

crayfish NMJ, the adult frog NMJ is, in most cases, singly innervated by an excitatory motoneuron and does not receive inhibitory inputs. Structure-function relationships have been studied at frog NMJs across synapses and AZs and between different muscle preparations.

Some of the first glimpses into the ultrastructure of frog NMJ synapses and AZs were observed using freeze fracture electron microscopy. Investigators discovered an array of well-organized neurotransmitter release sites where "plasmalemmal pockets" indicative of exocytosing synaptic vesicles were present following nerve stimulation (Heuser et al., 1979). These release sites were characterized by two linear double rows of roughly 10 nm intramembranous particles (akin to those observed in crayfish), some of which were believed to be VGCCs (Pumplin et al., 1981; Fig. 1.1). Strikingly, Heuser et al. (1979) found that vesicles fused along the outer lateral edge of the double row of particles, with the vesicles most closely localized to these particles having a higher probability of fusion, consistent with at least some intramembranous particles being VGCCs. Further evidence that some of these particles could be VGCCs was later provided by direct fluorescent labeling that confirmed VGCCs were preferentially present at presynaptic AZs (Cohen et al., 1991; Robitaille et al., 1990). While these data collectively provided evidence for a well-ordered AZ structure at the frog NMJ they lacked sufficient resolution to determine the stoichiometry of VGCCs to synaptic vesicles, and the functional contribution of individual VGCCs to neurotransmitter release, that is, how many VGCCs were responsible for triggering release.

1.2.1 How many VGCCs contribute to vesicle fusion at the frog NMJ?

While the direct labeling studies identified that there were likely many N type (CaV2.2) VGCCs present at AZs due to the labeling density (Cohen et al., 1991; Robitaille et al., 1990), one of the first direct observations of VGCC to vesicle stoichiometry was made by Harlow et al., (2001)

using electron microscope tomography to provide a three-dimensional glimpse into the AZ cytomatrix. They characterized a network of macromolecules including “beams” and “ribs” which connect docked synaptic vesicles with “pegs,” which are believed to be connected via plasma membrane macromolecular complexes to VGCCs. Each synaptic vesicle appeared to be localized to a small number of pegs, suggesting that at the frog NMJ each synaptic vesicle has a small number of associated VGCCs that could provide the require calcium ions for neurotransmitter release (Harlow et al., 2001). Further experiments using the “fast” and “slow” calcium chelators BAPTA and EGTA provided evidence that synaptic vesicles triggered to fuse were closely associated with VGCCs at the frog NMJ. Since EGTA has a slower binding rate for calcium than BAPTA at the same concentrations (Adler et al., 1991), one would expect to see a reduction in neurotransmitter release with EGTA only if there was a large separation between VGCCs and synaptic vesicles, giving EGTA time to bind cytoplasmic calcium ions. In fact, addition of BAPTA to the nerve terminal cytoplasm reduced neurotransmitter release, while addition of EGTA had a much smaller impact (Mukhamedyarov et al., 2009). These data suggest that there may be a close association between VGCCs and synaptic vesicles at the frog NMJ.

The number of VGCCs associated with each vesicle was further investigated by Dittrich et al. (2013) using a computational model of a frog NMJ AZ. This model allows for the tracking of individual calcium ions emanating from specific VGCCs as they diffuse throughout the model space. Constraining free parameters with known anatomical and physiological values, they discovered that functional measures such as the magnitude and timing of neurotransmitter release could be recapitulated if each synaptic vesicle was paired with a single, closely associated VGCC (Dittrich et al., 2013; Shahrezaei et al., 2006). Consistent with these data, Luo et al., (2015) demonstrated that when a vesicle was triggered to fuse, it was nearly always accompanied by the

opening of its most closely associated channel (94% of the time). However, while each vesicle was associated with a single channel and this channel could provide sufficient calcium ions for vesicle fusion, vesicle fusion proceeded more quickly when other nearby channels (on average ~2) contributed ions (Homan et al., 2018). These data suggest that at the frog NMJ, release is gated primarily by a single VGCC (referred to as single-domain gating; see Stanley, 2016), but other nearby channels provide a small but significant portion of the calcium ions required for release.

The above data are consistent with the finding that VGCCs open with a low probability during an action potential at the frog NMJ (Wachman et al., 2004), such that if a vesicle is going to be released, it would necessarily need to be close to one of the few rarely open channels. Using high-resolution calcium imaging techniques that allowed for visualization of calcium influx through VGCCs, Wachman et al., (2004) demonstrated that calcium influx during an action potential is sparse and variable across an AZ, providing evidence for a low density of VGCCs in the AZ, each with a low probability of opening. This hypothesis was confirmed by a subsequent study which determined that there are ~20–40 VGCCs (out of the ~200 intramembranous particles) with a probability of opening of ~0.2 (Luo et al., 2011). Therefore, when discussing how many VGCCs are required for triggering synaptic vesicle release, it is important to appreciate the role that the probability of VGCC opening plays in shaping the spatio-temporal calcium profile within a particular AZ organization.

1.2.2 Variability in synaptic strength at the frog NMJ

While the above studies provided a framework for understanding how many VGCCs contribute to vesicle fusion, they did not explore how variability in structure could contribute to variability in function. Using two frog muscles with divergent synaptic strength, investigators demonstrated that

the higher quantal content in the cutaneous pectoris muscle was underpinned by larger individual AZ sizes or a greater AZ length per unit length of terminal, as compared to the weaker synapses in sartorius muscle (Herrera et al., 1985) and cutaneous dorsi (Propst et al., 1986), respectively. Interestingly, AZs at the cutaneous pectoris appeared to be longer, more continuous and less broken up than at the cutaneous dorsi (Propst et al., 1986). Similar results were found in the comparison of AZs of synapses in slow and fast twitch muscles. Rather than the stereotypical paired double rows of intramembranous particles characteristic of AZs in nerve terminals onto fast twitch muscle, synapses onto slow twitch muscles appeared to contain AZs with a significant percentage of single rows of particles. Rows of particles also tended to be shorter and the average AZ length per unit length of nerve terminal was smaller in AZs of nerve terminals onto slow twitch muscle fibers (Verma and Reese, 1984). These data mirror the structural differences observed in strong and weak synapses at the crayfish NMJ and suggest that functional differences in neurotransmitter release could be underpinned by differences in AZ structure.

Within the same muscle, there can also exist functional differences across individual synapses. At both the cutaneous pectoris and sartorius muscles, both the magnitude and timing of neurotransmitter release vary considerably across synapses (Homan et al., 2018; Laghaei et al., 2018; Pawson and Grinnell, 1984; Trussell and Grinnell, 1985). At the sartorius muscle, differences in synaptic strength correlate with differences in presynaptic calcium influx (Pawson and Grinnell, 1990). The authors speculated that increases in calcium influx could be underpinned by greater numbers of VGCCs, suggesting VGCCs density could be a mechanism by which synapses could regulate strength. A recent study investigated the role that variable VGCC density and organization could play in modifying synaptic delay using a combination of electrophysiological recordings and computational modeling of a frog NMJ AZ (Homan et al.,

2018). Reducing the number of VGCCs present in the AZ led to longer synaptic delays, as did increasing the distance between VGCCs and release sensors on synaptic vesicles. Using a modified version of the model described in Dittrich et al. (2013), Homan et al. (2018) were also able to estimate the role of variable VGCC organization on the resulting spatiotemporal calcium profile surrounding vesicles triggered to fuse. In doing so, they were able to determine that the longer synaptic delays in their model were due to a slower accumulation of calcium ions around vesicle release sensors. These data suggest that variability in function across synapses within a single muscle could be explained by differences in the density and/or organization of VGCCs of AZs present at those synapses.

Interestingly, changing either the density or organization of VGCCs relative to synaptic vesicles was also predicted by their model to disrupt the coupling of VGCCs to released synaptic vesicles (Homan et al., 2018). Increasing the number of VGCCs in the AZ led to more "multi-domain gating" with an average of ~3 VGCCs contributing calcium ions for vesicle fusion (as compared to ~2 in control simulations). Conversely, reducing the number of VGCCs in the AZ led to a greater reliance on the most closely associated VGCC, and the number of VGCCs participating in release dropped to ~1. Moving VGCCs farther from release sensors led to a greater number of VGCCs contributing calcium ions for vesicle fusion. These data suggest that regulation of vesicle fusion by VGCCs is determined in part by the organization and density of VGCCs (Homan et al., 2018). Therefore, in determining how calcium triggers release, these experiments predict that it is necessary to not only determine which channels open and where, but the complicated spatio-temporal calcium dynamics within an AZ at the time of vesicle fusion.

1.2.3 Short-term plasticity at the frog NMJ

The frog NMJ is known for strong facilitation during short trains of stimuli (Laghaei et al., 2018; Fig. 1.2). While there has been no thorough investigation of the nature to which AZ ultrastructure correlates with differences in STP, investigators were able to provide evidence for an earlier notion raised at the crayfish NMJ that suggested there was a separate facilitation sensor distinct from that triggering evoked release (Yamada and Zucker, 1992). Using a simulated frog NMJ AZ, Ma et al., (2015) found that that residual bound calcium to a separate facilitation sensor could recapitulate the short-term facilitation observed at the frog NMJ. In exploring the sub-AZ properties that were underpinning facilitation at frog neuromuscular synapses, a more recent paper (Laghaei et al., 2018) concluded that the number of residual bound calcium ions was greater in frog AZs during trains of stimuli (see Fig. 7 in Laghaei et al., 2018). Further, shortening the frog AZ while maintaining the 1:1 vesicle to VGCC stoichiometry also led to greater depression. Reducing the number of VGCCs but keeping the same number of synaptic vesicles also led to increased depression (see Fig. 1.3). These data suggest that the spatio-temporal calcium profile within AZs at the time of vesicle fusion is a critical factor shaping STP. As the spatio-temporal calcium is a consequence of the underlying VGCC organization, it follows that STP could be greatly influenced by AZ structure at the frog NMJ.

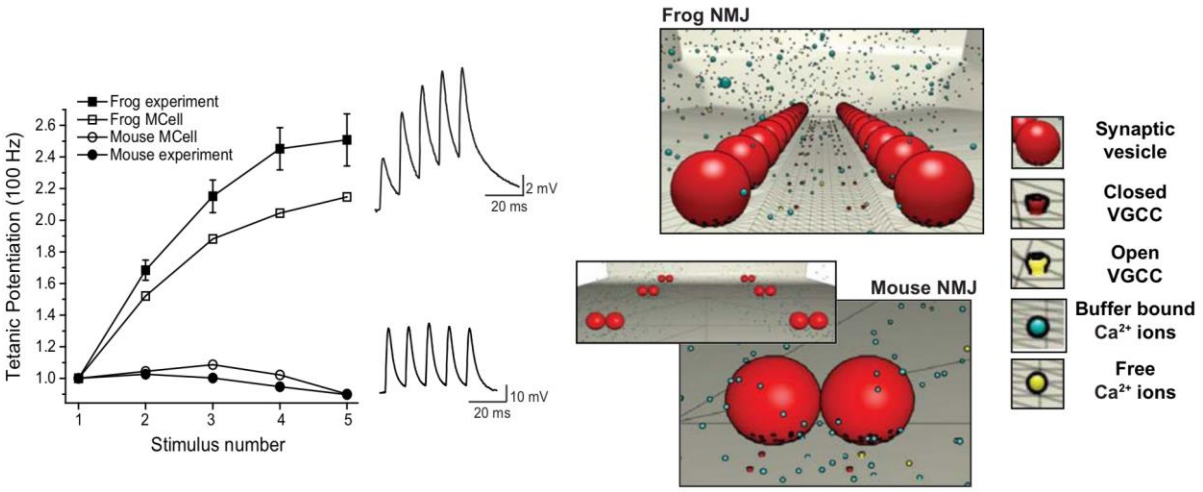

Figure 1.2 Frog and mouse NMJs exhibit divergent short-term plasticity characteristics.

Left plot shows the differences in short-term plasticity between the frog and mouse NMJs in response to 50 Hz stimulation. Filled symbols are results from intracellular electrophysiology recordings in ex vivo nerve-muscle preparations, while open symbols represent data from simulations conducted in MCell models of the frog and mouse NMJ AZs (adapted from Laghaei et al., 2018). Sample recordings from frog (top) and mouse (bottom) are shown next to the plot. Right images show representative snapshots of each AZ MCell model at one time point after an action potential stimulus, with a legend on the right side to identify key model elements.

1.3 The rodent NMJ

While the frog and crayfish NMJs have served as classical preparations by which to study presynaptic AZ structure and function, mouse or rat NMJs have also been studied, but to a lesser extent. Similar to the frog NMJ, the mouse and rat NMJs also consist of a single large contact from the presynaptic motoneuron onto the postsynaptic muscle fiber. Freeze fracture microscopy studies identified that rather than the long rows of linearly arranged intramembranous particles as seen in

frog, that mouse NMJ AZs were organized in a similar linear array but were much shorter (80 nm long in mouse versus 1–2 µm in frog, Rash and Ellisman, 1974). Further, rather than vesicles fusing along the outer edge of the intramembranous particle array (as observed at frog AZs), vesicles at rodent AZs fused between the 2 double rows of intramembranous particles believed to include VGCCs (Nagwaney et al., 2009). Therefore, as compared to frog NMJ AZs, rodent AZs organize VGCCs on both sides of docked synaptic vesicles, whereas, frog AZ vesicles only have VGCCs on one side (Harlow et al., 2001; Nagwaney et al., 2009; Fig. 1.1). Further, the number of docked synaptic vesicles, presumably representing the size of the ready-releasable pool of vesicles, was estimated to be on average ~1700 during high frequency stimulation (Ruiz et al., 2011). Given that there are on average around 900 AZs per synapse (Laghaei et al., 2018; Ruiz et al., 2011), these data correspond well with previous work suggesting that approximately two docked vesicles exist per AZ (Nagwaney et al., 2009).

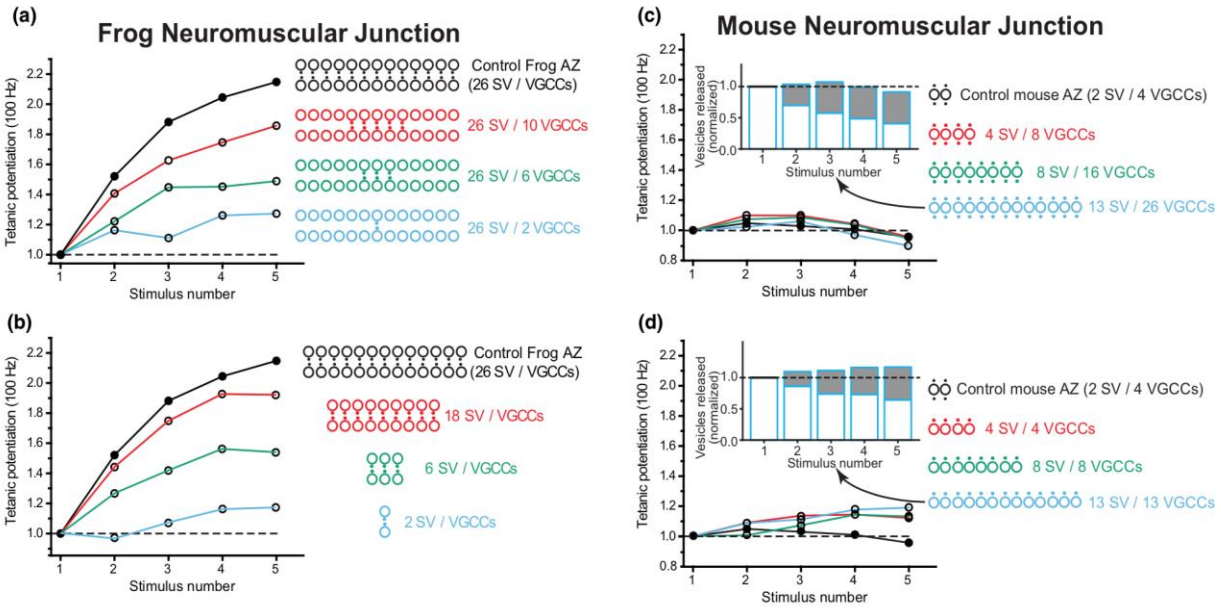

Figure 1.3 The effect of variable AZ organization on short-term plasticity at modeled frog and mouse neuromuscular junctions.

(a) The control configuration of a computational model of a frog NMJ AZ (black) has 26 VGCCs (small black dots) and synaptic vesicles (large open circles) and exhibits strong facilitation during a 100 Hz stimulus train. The diagrams at right represent the different manipulations made to the number of VGCCs, and the effects of those manipulations are plotted against the control model. Reducing the number of VGCCs in a frog AZ but retaining the same number of synaptic vesicles reduces short-term facilitation. (b) Shortening the frog AZ by removing both VGCCs and synaptic vesicles reduces short-term facilitation. (c) The control configuration of a computational model of a mouse NMJ AZ (black) has 4 VGCCs (small black dots) and 2 synaptic vesicles (large open circles) and exhibits mild facilitation followed by mild depression during a 100 Hz stimulus train. The diagrams at right represent the different manipulations made to the number of VGCCs and the effects of those manipulations are plotted against the control model at left. The inset represents the fraction of vesicle fusion events that had residual bound calcium ions for the manipulation represented in blue (newly bound calcium ions are shown in the open bars, while residual bound calcium is shown in the shaded bars for each stimulation in the short train). Lengthening the mouse AZ by adding synaptic vesicles and VGCCs does not have a large effect on STP. (d) Reducing the number of VGCCs while increasing the length of the AZ leads to a mild increase in facilitation. Adapted from Laghaei et al. (2018).

1.3.1 How many VGCCs contribute to vesicle fusion at the rodent NMJ?

While it was found that a single, closely associated VGCC was sufficient to trigger neurotransmitter release at the frog and crayfish NMJs, it is presently unknown the precise coupling of VGCCs to synaptic vesicle release at the rodent NMJ. Electron microscope tomography experiments revealed similar “beams,” “ribs,” and “pegs” structures as were observed at the frog NMJ. However, in contrast to the frog NMJ, vesicles at the mouse NMJ AZ have up to 4 associated “pegs,” believed to include VGCCs. As investigators determined that there were ~2

docked vesicles per AZ, these data suggest that there could be up to 4 VGCCs associated with each synaptic vesicle. These data provided evidence that the VGCC to synaptic vesicle ratio is significantly different as compared to the frog NMJ AZ (which had up to 2 associated channels, Dittrich et al., 2013; Harlow et al., 2001). There is also some evidence to suggest that the distance between VGCCs and synaptic vesicles is different at mouse versus frog NMJ AZs. At the frog NMJ, vesicle release occurs on the outer edge of the two double rows of intramembranous particles (putative VGCCs, see Fig. 1.1). The distance between the center of a fusing synaptic vesicle and the first row of intramembranous particles was measured to be ~42 nm (Heuser et al., 1979). Given that a synaptic vesicle is ~50 nm in diameter (Heuser et al., 1979; Rash & Ellisman, 1974), these data suggest that the coupling distance between VGCCs and synaptic vesicles is ~17 nm. At the mouse NMJ, however, vesicle release occurs between the two rows of intramembranous particles and the distance between those rows was measured to be ~60 nm (Fukoka et al., 1987). Subtracting the diameter of the intramembranous particles (~10 nm) leaves a particle edge to particle edge distance of ~40 nm (Fukoka et al., 1987). These data suggest that there may be a closer spatial association of VGCCs and synaptic vesicles at mouse as compared to frog NMJ AZs, which could account for their differences in function.

1.3.2 Variability in neurotransmitter release at the rodent NMJ

With respect to variability in release at rodent NMJs, investigators have compared differences in synaptic strength across two different motor-nerve preparations, the soleus, characterized primarily by slow twitch fibers (analogous to tonic synapses in crayfish) and the extensor digitorum longus muscle, characterized primarily by fast twitch fibers (analogous to phasic synapses in crayfish). While these two types of rodent synapses have different measured quantal contents (Wood and

Slater, 1997), the size of their AZs and density and distribution of putative VGCCs were not significantly different (Ellisman et al., 1976). These data are similar to those at the crayfish NMJ, suggesting there was no difference in structure underlying function (Msghina et al., 1999). However, as in crayfish, without knowing the precise stoichiometry of VGCCs to synaptic vesicles, it is difficult to contextualize these data.

Across synapses at the mouse NMJ, it appears the magnitude of neurotransmitter release varies (Laghaei et al., 2018; Ruiz et al., 2011). While definitive links to variable AZ structure underlying differences in function have not been made at the rodent NMJ, estimations of the probability of release across AZs at the mouse NMJ did appear to differ. A binomial analysis of neurotransmitter release at the mouse NMJ demonstrated that the probability of release was quite high (~0.9). However, the same study identified that the number of release sites was rather low (on the order of ~70; Wang et al., 2010). These data are difficult to reconcile with other studies which have directly measured the number of AZs to be as high as ~900 (Chen et al., 2012; Laghaei et al., 2018; Ruiz et al., 2011). One interpretation of these findings is that only a small portion of the hundreds of available AZs actually participate in neurotransmitter release, while the majority (80–90%) are functionally silent. This notion was raised by Wang et al. (2010), who suggested that the varying sensitivities of the release machinery to calcium (which could be caused by different vesicle to VGCC arrangements) across different AZs could account for the variable probability of release. Further, using optical reporters of synaptic vesicle fusion, investigators discovered “hot spots” of exocytosis during high frequency stimulation where vesicle fusion preferentially occurred (Tabares et al., 2007; Wyatt and Balice-Gordon, 2008). These data provide evidence for the hypothesis that across a single motor nerve terminal, transmitter release may preferentially occur at distinct sites while others remain functionally silent.

1.3.3 Short-term plasticity at the rodent NMJ

At most mouse NMJ synapses, mild short-term depression is often observed following a short train of stimuli, such that subsequent responses are smaller than the initial response (Laghaei et al., 2018; Wang et al., 2010). It was recently discovered that this mild depression at the mouse NMJ may be due in part to its distinct AZ organization as compared to the frog NMJ, such that mouse NMJ AZs have a greater number of associated VGCCs per synaptic vesicle and a corresponding higher probability of release (Laghaei et al., 2018; Fig. 1.2). While the mechanism behind this short-term depression has not been fully elucidated, the contribution of residual bound calcium ions on the putative facilitation sensor was studied in a computational model of a mouse NMJ AZ (Laghaei et al., 2018). If residual bound calcium ions were contributing to facilitation at the frog NMJ as discussed above, then one would expect that the mouse should have fewer bound calcium ions over a series of successive stimuli. Indeed, simulated mouse NMJ AZs appear to have fewer residual bound calcium ions over successive stimuli in a train. However, simply increasing the length of the mouse NMJ AZ while maintaining the 2:1 VGCC to synaptic vesicle stoichiometry led to a slight increase in residual bound calcium and this increase was not matched by a corresponding increase in facilitation (Fig. 1.3). If the mouse NMJ AZ was rearranged such that there was a 1:1 VGCC to synaptic vesicle stoichiometry (similar to the frog structure), there was an associated increase in facilitation (Fig. 1.3). As mouse NMJ AZs were also found to have a greater probability of release than frog NMJ AZs, these data also are in agreement with Pan and Zucker's (2009) generalizing principle of short-term synaptic plasticity. Collectively, these data suggest that the vesicle to VGCC stoichiometry is an important determinant of the probability of release and STP.

In addition to exploring how a single AZ organization can influence STP, Laghaei et al. (2018) also explored the spacing of AZs relative to one another. When AZs were spaced closer together, there was an increased number of residual bound calcium ions, but greater short-term depression. These data collectively indicate that the total residual bound calcium in and of itself may not be a good indicator of which form of STP (facilitation or depression) will dominate, rather it is important to also account for the VGCC to synaptic vesicle stoichiometry and the arrangement of VGGCs relative to synaptic vesicles, all of which shape the spatiotemporal calcium profile within AZs at the time of vesicle fusion.

1.4 Can structure inform function at the NMJ?

A unifying principle across the majority of NMJs studied appears to be the presence of hundreds of release sites (AZs) onto a single postsynaptic muscle fiber. However, each species appears to have a unique synaptic and AZ structure. Vertebrates build their NMJs with a single, large contact onto the postsynaptic muscle fiber which contains hundreds of individual AZs with well-ordered ion channel organizational structures. Invertebrates seem to prefer numerous small contacts, each with few AZs that do not seem to have distinct structural patterns (clustered organization). Therefore, is there an evolutionary advantage for crayfish to have many small contacts versus a large endplate? And between two species that favor endplates (frog and mouse), do the long AZs in frog versus the short AZs in mouse yield functional consequences?

Crustacean muscle fibers have been demonstrated to produce graded postsynaptic muscle contractions and do not need to rely on action potential propagation to produce strong contractions (Katz and Kuffler, 1946). Further, the small bouton contacts of the crayfish NMJ have been

suggested to have more capability for specialized plasticity than the large endplates of vertebrates (Atwood and Karunanithis, 2002). The small endplates, therefore, could allow for dynamic control of excitability of the postsynaptic muscle, which would be potentially useful in a system using graded potentials. The large endplates in vertebrates, however, could be important for ensuring that the postsynaptic muscle is depolarized beyond threshold, ensuring an all-or-none action potential and subsequent muscle contraction. Further, the nature of the environment, each species has adapted to live in, could also inform some of the differences observed in AZ structure. Crayfish and frogs likely experience a great diversity of temperatures in their environment, and as cold-blooded organisms, need to be able to function efficiently regardless the conditions. Rodents, however, are warm-blooded organisms, and therefore, their NMJs do not experience such large variations in temperature. Perhaps the significant facilitation observed in frog could be an evolutionary strategy to ensure that the postsynaptic muscle cell is brought to threshold despite the temperature, while the varied plasticity in crayfish could be a flexible strategy to ensure control over postsynaptic excitability. In contrast, the relatively stable level of neurotransmitter release observed in mouse could be an adaptation to relatively constant body temperature (Laghaei et al., 2018).

In addition to the differences in the structure of the overall NMJ between species, there are also considerable differences in the structure of individual AZs within the NMJ. Mouse and frog NMJ AZs have well-ordered structure with linear arrays of vesicles and VGCCs, while crayfish NMJ AZs appear to lack a stereotypical structure, with VGCCs clustering around docked synaptic vesicles. This clustered arrangement could allow for more nuanced control over neurotransmitter release, which could account for the varied short-term plasticity observed across synapses at this preparation. Regardless of the species, the magnitude of neurotransmitter release and synaptic

plasticity are shaped by the spatio-temporal calcium profile within AZs at the time of vesicle fusion. This spatio-temporal profile is governed by the organization and density of VGCCs relative to synaptic vesicles, as well as the probability of calcium channel opening. Therefore, the nature to which structure determines function cannot be fully appreciated without understanding the complicated interplay between VGCC density and gating, and the resulting spatial and temporal aspects of calcium ion interactions with calcium release sensors. New technological advances in super-resolution microscopy (Jones et al., 2017; Nishimune et al., 2016; York and Zheng, 2017) and advanced computational techniques (Garcia et al., 2016) will surely inform new perspectives of structure-function relationships at the NMJ.

2.0 Impact of spatiotemporal calcium dynamics within presynaptic active zones on synaptic delay at the frog neuromuscular junction[2]

2.1 Introduction

The calcium dynamics within presynaptic release sites (active zones, AZs) at the time of vesicle fusion is one of the key factors underlying neurotransmitter release and plasticity. During an action potential, voltage-gated calcium channels (VGCCs) activate and open, leading to a strong but transient increase in the calcium concentration around the mouth of the open channel called a calcium microdomain (Borst and Sakmann, 1996). The calcium ions then diffuse away from the channel and interact with proteins including neurotransmitter release sensors, calcium buffering proteins, and kinases. Many investigators have sought to determine the amplitude and time course of the calcium microdomain across a variety of different preparations, as well as the functional consequences of disrupting or manipulating this calcium microdomain (Eggermann et al., 2012).

At the calyx of Held giant synapse in the auditory brain stem it is well established that the synapse is refined throughout the course of development to support high-fidelity information transfer. At early stages of development, AZs at the calyx of Held have a "looser" organization, with larger distances between VGCCs and synaptic vesicles (Fedchyshyn and Wang, 2005; Wang et al., 2008). Calcium transients measured from these immature AZs are also smaller than those

[2] This chapter was published as: Homan AE, Laghaei R, Dittrich M, Meriney SD. Impact of spatiotermporal calcium dynamics within presynaptic active zones on synaptic delay at the frog neuromuscular junction. *J Neurophysiol* 119, 2018. Reproduced with permission from the American Physiological Society.

measured in the adult synapse (Nakamura et al., 2015; Wang et al., 2008). Functionally, these immature synapses exhibit a longer synaptic delay than adult synapses (Nakamura et al., 2015). As the synapse matures, VGCCs become more tightly coupled to synaptic vesicles and the timing of transmitter release is faster to support the efficient transmission of high-frequency auditory information (Nakamura et al., 2015). These data demonstrate that AZ structure, specifically VGCC density and organization, can play a large role in shaping the calcium dynamics within the AZ and subsequent transmitter release throughout synapse development. However, it is not well understood how variability in AZ structure (and thus calcium dynamics) could underpin functional variability in a single adult preparation.

The adult frog neuromuscular junction (NMJ) has been another historically important preparation for studying factors shaping presynaptic neurotransmitter release because of the ease of manipulation and the well-defined structure of its AZs (Birks et al., 1960; Heuser et al., 1979; Katz and Miledi, 1969). A number of studies have shown that there is considerable variability in the magnitude of neurotransmitter release (quantal content) across synapses in this preparation (Grinnell and Herrera, 1980; Pawson and Grinnell, 1989; Propst and Ko, 1987). Using freeze fracture ultrastructural analysis, Propst and Ko (1987) found that both the size of the AZ and the number of intramembranous particles (thought to be proportional to the number of putative VGCCs) per synapse positively correlated with quantal content. Another intriguing result from Pawson and Grinnell (1984) suggested that variability in the strength of neurotransmitter release could be explained by differences in presynaptic calcium influx, providing possible evidence that variability in AZ structure (and particularly the organization and density of VGGCs and the resulting spatiotemporal calcium profile) may underpin functional variability observed in the adult frog NMJ.

Here we sought to identify whether variability in the spatiotemporal calcium dynamics caused by variability in AZ structure can provide a framework to understand functional heterogeneity in a mature preparation. We leveraged a previously published, spatially realistic, diffusion reaction-based computational model of a frog NMJ AZ (Dittrich et al., 2013; Ma et al., 2015) to perform a parameter search to understand how certain variables including VGCC density and organization and buffer concentration influence the spatiotemporal calcium profile and synaptic delay. Furthermore, we aimed to extrapolate our results to provide a framework to understand how variability in AZ structure may underpin variability in presynaptic function.

2.2 Materials and Methods

2.2.1 Intracellular electrophysiology

Adult male and female frogs (*Rana pipiens*; Connecticut Valley Biological Supply) were anesthetized in 0.1% tricaine methanesulfonate, decapitated, and double-pithed in accordance with procedures approved by the University of Pittsburgh Institutional Animal Care and Use Committee. All experiments were performed on summer frogs (June to August) to control for seasonal differences in neurotransmitter release (Pawson and Grinnell, 1989). Cutaneous pectoris muscles were bilaterally removed and bathed in normal frog Ringer solution (NFR; in mM: 116 NaCl, 2 KCl, 1.8 $CaCl_2$, 1 $MgCl_2$, 5 HEPES, pH 7.3). For low-calcium experiments, $CaCl_2$ concentration was reduced to 0.5 mM and $MgCl_2$ increased to 4 mM. The nerve was drawn into a suction electrode and stimulated at 10 times the intensity required to elicit a muscle contraction. Before recording, preparations were bathed in μ-conotoxin PIIIA (Alomone Laboratories) to

prevent most muscle contraction, with any residual contractions further blocked by inclusion of 0.1–0.5 μM tubocurarine chloride hydrate (Sigma-Aldrich) in the bath during recording. All recordings were performed at temperatures ranging between 21°C and 23°C with constant perfusion of saline (3–5 mL/min).

Single nerve-evoked synaptic activity (end-plate potentials, EPPs) was recorded at 0.5 Hz with the intracellular current-clamp microelectrode technique with 40- to 60-MΩ borosilicate pipettes backfilled with 3 M potassium acetate. All data were collected with an Axoclamp 900A amplifier and digitized at 25 kHz for subsequent analysis with pCLAMP 10 software (Molecular Devices). All recordings were corrected for nonlinear summation (McLachlan and Martin, 1981) before analysis.

2.2.2 Extracellular recording of action potential-mediated currents

To record action potential-mediated currents, focal extracellular recordings were made by placing a relatively large-diameter borosilicate micropipette (1–2 MΩ) filled with NFR over the last myelinated segment of the innervating nerve. The pipette was lowered until an observable voltage deflection corresponding to the influx of sodium into the nerve terminal was observed. For all *ex vivo* recordings, synaptic delay was measured starting from the peak of the extracellularly measured presynaptic sodium current to the peak of the intracellularly measured postsynaptic EPP. All extracellular recordings were made at the conclusion of intracellular current-clamp recordings to minimize any possible damage to the synapse caused by mechanical pressure from the extracellular pipette.

2.2.3 Monte Carlo simulations

We used the frog NMJ single-AZ model developed and described by Ma et al. (2015) and simulated with MCell (www.mcell.org; Kerr et al., 2008; Stiles et al., 1996; Stiles and Bartol, 2001). A detailed description of the model can be found there, but briefly our frog AZ model contains 26 docked vesicles positioned in two parallel rows with 26 CaV2.2 VGCCs placed in a double row ~39 nm from vesicles in a 1:1 stoichiometry. To model endogenous calcium buffers, we used a 2 mM fixed buffer (except when varied in Fig. 2.5). Single-vesicle delay in the model was determined as the time duration between the onset of the presynaptic action potential waveform and the moment at which release sensors on docked synaptic vesicles bound sufficient calcium ions for vesicle fusion (see the calcium binding model described by Ma et al., 2015). We do not model the processes involved in vesicle fusion with plasma membrane after calcium ion binding and assume that the processes following calcium binding do not vary as a result of our experimental manipulations. For ease of discussion, any reference to vesicle fusion in our model from this point forward refers to the moment at which vesicle release sensors bound sufficient calcium ions for vesicle fusion. Since our model only represents a single AZ, we mimicked the *ex vivo* experimental measurements of synaptic delay from an entire nerve terminal by resampling the simulated single-vesicle delays into bins of 600 (roughly 100–900 vesicles are released on average from a frog NMJ nerve terminal as a result of an action potential) and then calculated the mean of the resampled single-vesicle delays to yield a simulated "synaptic" delay from an entire nerve terminal.

The percent contribution of calcium ions derived from specific open VGCCs to vesicle fusion (Fig. 2.2F, Fig. 2.3F, Fig. 2.4F, Fig. 2.5E) was calculated as the average ratio of ions contributed by a particular VGCC to the total number of calcium ions required for vesicle fusion.

We analyzed the percentage of calcium ions contributed by the 10 channels immediately surrounding the vesicle triggered to fuse (see Fig. 2.2F for a schematic), as the remaining channels had insignificant contributions (<1% total for the remaining 16 channels in the AZ). The average number of VGCCs participating in release (Table 2.1) was calculated by determining the total number of VGCCs that contributed any ions to fusion of a vesicle in each seed where a vesicle fusion event occurred and then averaging this measurement over the total number of seeds with vesicle fusion events for each condition.

The spatiotemporal calcium profile (Fig. 2.2D, Fig. 2.3D, Fig. 2.4D, Fig. 2.5C) around vesicle release sensors was determined by placing a defined 40 nm × 40 nm × 15 nm "sampling box" directly under each synaptic vesicle in the model and counting the number of calcium ions that were inside the box during each time step (10 ns), and binning these into 500 ns bins, for those vesicles that were triggered to fuse (see Fig. 1D of Ma et al., 2015). The data were filtered with a Gaussian convolution kernel (standard deviation of the filter window = $9.47e^{-7}$ s). The 10% to 90% of the rise was also plotted and fit by linear regression. It is important to note that the R^2 values for these best fit lines are rather low despite the large effect sizes because of the stochastic and probabilistic nature of the data. Because VGCC activation is stochastic and the probability of channel opening during an action potential is small (0.2), the number of calcium ions in the sampling box at any one time step is essentially binary (either 0 or 1 ion). The average number of calcium ions within the sampling box at each time step is plotted on the right-hand scale of the plots in Fig. 2.2, D and E, Fig. 2.3, D and E, Fig. 2.4, D and E, and Fig. 2.5, C and D. Because the time step is small and the number of open VGCCs in the AZ is low, this average is always < 1 ion. The R^2 values for lines fit to the mean values (and thus to the average behavior of the data over time) were nearly 1 (R^2 values fit to the mean values for Fig. 2.2E, Fig. 2.3E, Fig. 2.4E, and Fig.

2.5D: control: 0.999, 0.9 mM Ca^{2+}: 0.998, 2.4 mM Ca^{2+}: 0.998, 3.6 mM Ca^{2+}: 0.996, 5 nm: 0.997, 10 nm: 0.997, 15 nm: 0.997, 20 nm: 0.996, 4 VGCCs: 0.997, 13 VGCCs: 0.998, 52 VGCCs: 0.999, 0.2 mM fixed buffer: 0.998, 1.0 mM fixed buffer: 0.990, 8.0 mM fixed buffer: 0.999).

The calcium ion diffusion coefficient is the rate at which free calcium ions diffuse within our model environment when not bound to any sites, while the buffered diffusion coefficient is the measured rate of diffusion in the model when these calcium ions bind and unbind from the fixed buffer that populates the model environment and slows their rate of movement across the model space. Buffered diffusion was calculated with our frog simulation model with only one VGCC. All of the appropriate concentrations of buffers were included as described for the full AZ model (see Ma et al., 2015). An action potential waveform was delivered to the modeling space, triggering activation of the VGCC and leading to diffusion of calcium ions throughout the space. The diffusion coefficient of tracked calcium ions was calculated with standard averaged mean square displacement method. Trajectories of ions were used to calculate mean squared displacement (msd) vs. time interval (t). The msd is defined as: $msd(t) = \langle |r(t + t_0) - r(t_0)|^2 \rangle$ where the average $\langle ... \rangle$ runs over all particles in the system.

2.2.4 Statistical analysis

All statistical analysis was performed with MATLAB (MathWorks) or GraphPad Prism (GraphPad Software). Data are presented as means ± SE unless otherwise noted.

2.3 Results

2.3.1 Inherent variability in synaptic delay

We found that there was considerable variability in synaptic delay across individual synapses at the frog NMJ (Fig. 2.1B). Experimentally, we defined synaptic delay as the time between the arrival of a presynaptic action potential at the motor nerve terminal (as determined by extracellular recordings of sodium current from the last myelinated segment of the nerve) and the peak of a postsynaptic EPP (as measured by intracellular microelectrode recording from the muscle; Fig. 2.1A). This definition differs slightly from that in previous studies investigating synaptic delay, which was the time duration from the arrival of a presynaptic action potential to the beginning of the rise of the EPP (Katz and Miledi, 1965). We used the peak of the EPP to more easily compare our experimental measurements with data from our modeling simulations, since our simulations represent the mean of the single-vesicle delays (see full explanation in Monte Carlo simulations) rather than the first synaptic delay (which is recorded when measuring from the presynaptic action potential to the start of the postsynaptic EPP) or the release time course, which does not take into account the timing of the presynaptic action potential. However, all relative trends reported here were independent of the precise definition of delay and were recapitulated when synaptic delay measurements were made using the start of the EPP rise (synaptic delay mean when measured to rise: 0.66 ± 0.02 ms, range: 0.43–0.91 ms).

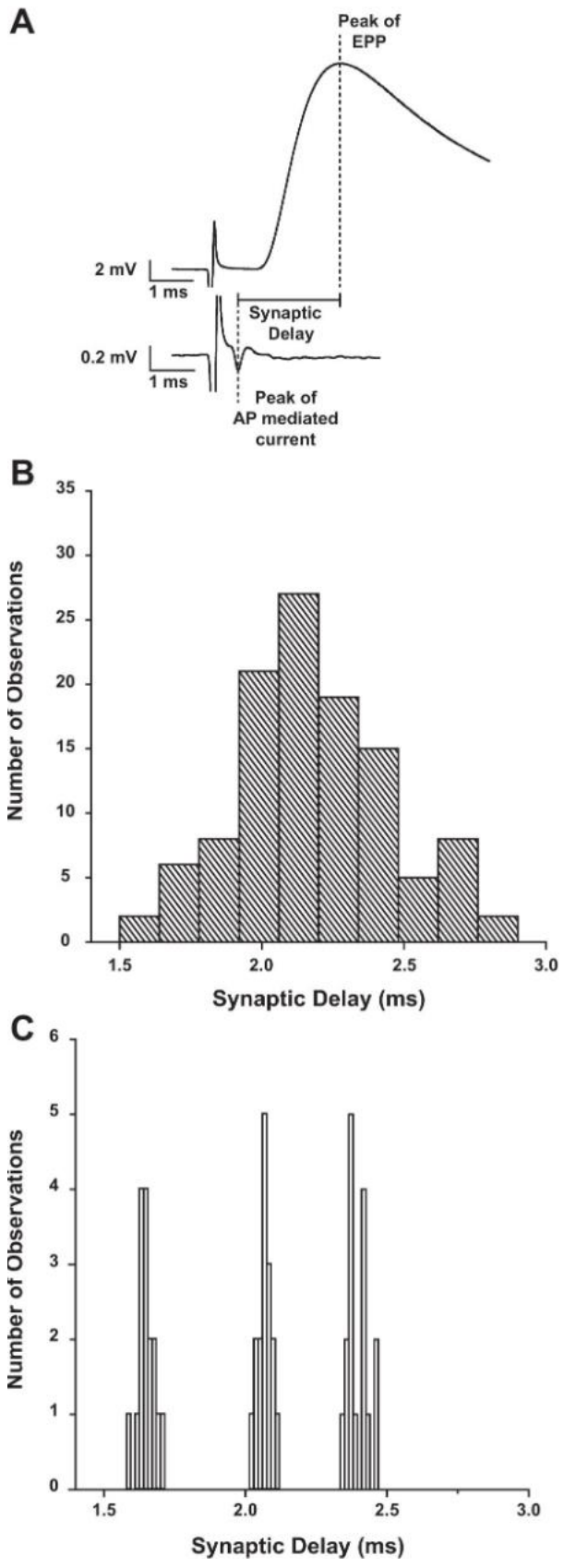
A
Peak of
EPP
2 mV
1 ms
Synaptic
Delay
0.2 mV
1 ms
Peak of
AP mediated
current
B
Number of Observations
35
30
25
20
15
10
5
0
1.5
2.0
2.5
3.0
Synaptic Delay (ms)
C
Number of Observations
6
5
4
3
2
1
0
1.5
2.0
2.5
3.0
Synaptic Delay (ms)

Figure 2.1 Synaptic delay varies across but not within synapses at the frog NMJ.

A: Schematic that includes sample data to demonstrate how synaptic delay was calculated as the time duration between the peak of the presynaptic action potential (AP)-mediated current and the peak of the average postsynaptic EPP. B: Average synaptic delays measured across multiple synapses. At each synapse, synaptic delay was calculated as the average of 15 trials, and the mean at each synapse was pooled from 54 synapses to create the histogram presented in B. C: Individual synaptic delay measurements made from 3 of the 54 individual synapses shown in B. Repeated measurements (n = 16) made at each synapse demonstrate little variability within synapses but significant differences between them.

It is also important to note that synaptic delay values are not identical when comparing data from modeling simulations and experimental manipulations, as the two measurements are not quantitatively equivalent. These differences are due in part to the fact that our experimental measurements of synaptic delay include synaptic vesicle fusion, release and diffusion of acetylcholine across the synaptic cleft, binding of acetylcholine to postsynaptic receptors, and flux of cations across the postsynaptic muscle cell membrane. Our modeling simulations, however, end when the release sensors bind sufficient calcium to trigger vesicle fusion (see the calcium binding scheme in Ma et al., 2015). The difference in mean synaptic delay measured experimentally compared with our simulations is ~0.5 ms, which may be explained by several inherent differences in the measurements in the model vs. our physiology recordings. First, our modeled synaptic delay measurement begins with the onset of the action potential waveform, while our physiological measurement begins with the peak of the presynaptic sodium current (likely to occur several hundred microseconds later). Second, transmitter release in the model is measured as the time at which sufficient calcium ions have bound calcium sensors on synaptic vesicles to be considered the trigger for vesicle fusion. This excludes what is often termed “minimum synaptic delay,” or the time required for calcium-triggered synaptic vesicle fusion, transmitter diffusion across the

synaptic cleft, binding of transmitter to postsynaptic receptors, and gating of postsynaptic current through receptors. A number of studies have estimated the timing of these processes, including vesicle fusion and exocytosis (estimated to occur within 50 to hundreds of microseconds; Sabatini and Regehr, 1996; Heidelberger et al., 1994), diffusion of neurotransmitter across the synaptic cleft (which would add at most several microseconds; Sabatini and Regehr, 1999), and activation of postsynaptic receptors (which adds an insignificant time step that is unlikely to influence delay; Sabatini and Regehr, 1999). While these studies have not been investigated in isolation at the NMJ, these processes add a constant to our modeled synaptic delay measurements. Given these differences, our approach has been to focus this study on the relative changes in synaptic delay within each experimental approach (rather than comparing absolute values between model and physiology experiments). This approach is most relevant when using the modeling simulations to inform and interpret our physiological experimental manipulations.

Synaptic delay measured across a population of synapses at the frog NMJ was on average ~2.2 ms (Fig. 2.1B) but varied across individual synapses (ranging from 1.60 to 2.72 ms). However, when synaptic delay was measured from three individual representative synapses (16 sweeps per synapse) we found a narrower distribution (for example, 1.65 ± 0.03 ms, 2.06 ± 0.02 ms, and 2.40 ± 0.04 ms; Fig. 2.1C). These data indicate that synaptic delay did not vary significantly within an individual synapse over repeated trials but was more variable between synapses (comparing the 3 representative synapses shown in Fig. 2.1C: $P < 0.0167$, 1-way ANOVA with Bonferroni correction, $\alpha = 0.0167$). In considering the source of variability between synapses, we found no significant relationship between synaptic delay and muscle fiber input resistance. Furthermore, experiments using two-electrode voltage clamp to more precisely control the postsynaptic muscle fiber voltage yielded results similar to those presented here with current-

clamp recordings (data not shown). There was also no apparent correlation between synapse location along the axon branch (distance from the nerve entry point into the muscle) and synaptic delay (data not shown), ruling out muscle fiber size and location-dependent effects as contributors to the variability in synaptic delay.

To understand what could contribute to this variability in synaptic delay, we performed a detailed parameter sweep using a previously validated, spatially realistic model of the frog NMJ AZ. This stochastic diffusion reaction-based model is highly constrained by the results of over 50 years of ultrastructural, physiological, and biochemical studies conducted at the frog NMJ (Dittrich et al., 2013).

2.3.2 Role of calcium concentration in synaptic delay

We first wanted to determine whether spatio-calcium dynamics with the AZ could contribute to synaptic delay at the NMJ (Fig. 2.2A). Reducing extracellular calcium led to a slowing in the mean synaptic delay from 1.67 ms (SD = 0.04) in the 1.8 mM Ca^{2+} model (control) to 1.86 ms (SD = 0.05) in the 0.9 mM Ca^{2+} model (Fig. 2.2B). Conversely, increasing the extracellular calcium concentration led to a significantly faster mean synaptic delay of 1.51 ms (SD = 0.04) in the 3.6 mM Ca^{2+} model (Fig. 2.2B). To determine possible mechanisms for this slowing in synaptic delay, we next analyzed the sub-AZ spatiotemporal calcium profile resulting from each manipulation. To define the calcium profile near a vesicle triggered to fuse, we calculated the calcium concentration within a sampling box below the vesicle (previously described in Ma et al., 2015; Fig. 2.2D). We found that decreasing extracellular calcium led to a lower peak calcium concentration within the sampling box, from 8.48 μM in the 1.8 mM Ca^{2+} model (control) to 2.42 μM in the 0.9 mM Ca^{2+} model (Fig. 2.2D). Conversely, increasing extracellular calcium led to an increase in the peak

calcium concentration within the sampling box to 13.5 μM in the 3.6 mM Ca^{2+} model (Fig. 2.2D). Decreasing extracellular concentration also led to a significant decrease in the slope of the line fit to the 10–90% rise of the calcium profile (126.97 ± 0.20 μM/ms in 1.8 mM Ca^{2+} vs. 36.13 ± 0.15 μM/ms in 0.9 mM Ca^{2+}), while increasing extracellular calcium led to a faster slope (236.27 ± 0.44 μM/ms in 3.6 mM Ca^{2+}; Fig. 2.2E).

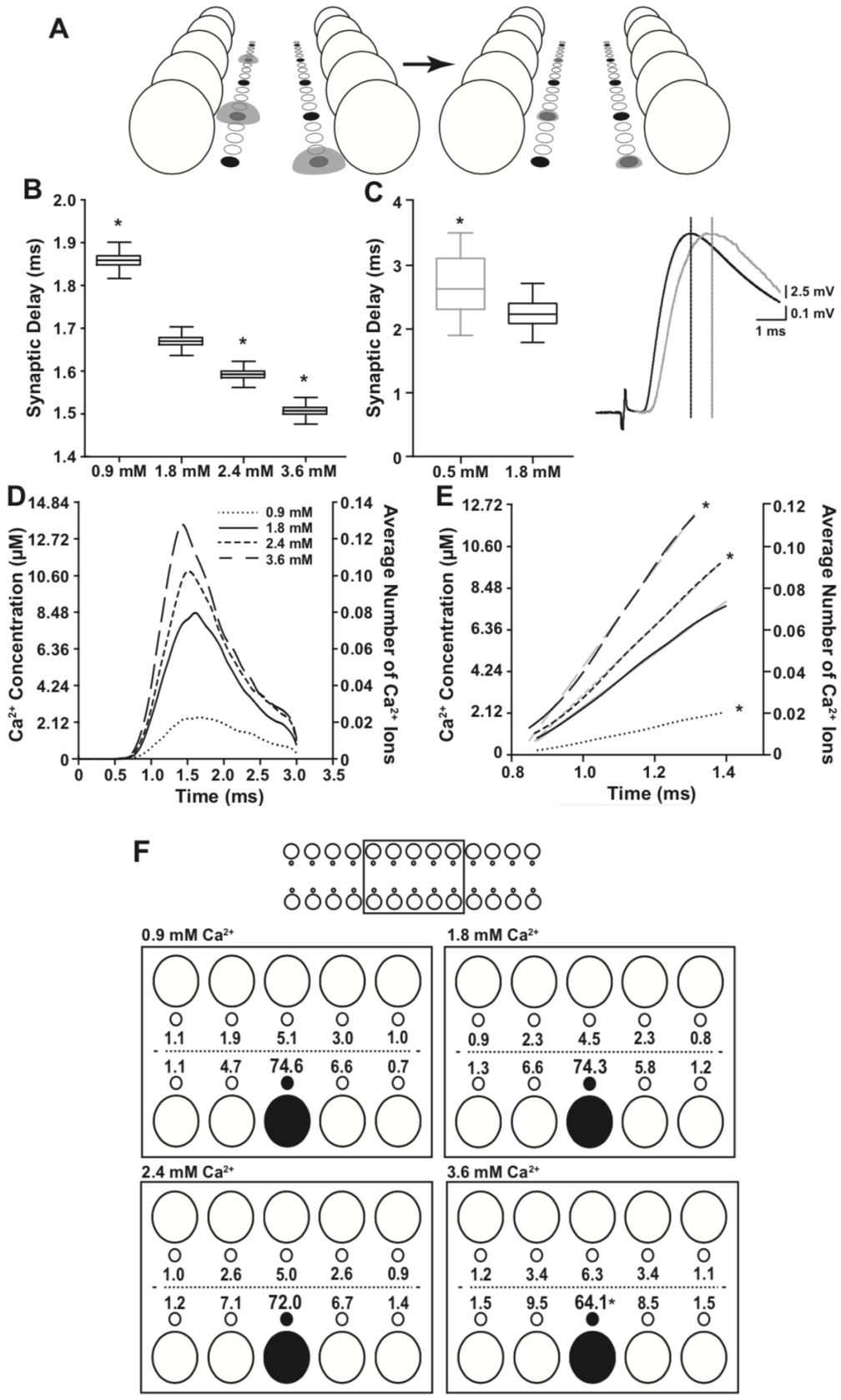
A
B
Synaptic Delay (ms)
0.9 mM 1.8 mM 2.4 mM 3.6 mM
C
Synaptic Delay (ms)
0.5 mM 1.8 mM
2.5 mV
0.1 mV
1 ms
D
Ca2+ Concentration (μM)
Average Number of Ca2+ Ions
0.9 mM
1.8 mM
2.4 mM
3.6 mM
Time (ms)
E
Ca2+ Concentration (μM)
Average Number of Ca2+ Ions
Time (ms)
F
0.9 mM Ca2+
1.1 1.9 5.1 3.0 1.0
1.1 4.7 74.6 6.6 0.7
1.8 mM Ca2+
0.9 2.3 4.5 2.3 0.8
1.3 6.6 74.3 5.8 1.2
2.4 mM Ca2+
1.0 2.6 5.0 2.6 0.9
1.2 7.1 72.0 6.7 1.4
3.6 mM Ca2+
1.2 3.4 6.3 3.4 1.1
1.5 9.5 64.1* 8.5 1.5

Figure 2.2 Role of extracellular calcium on synaptic delay.

A: Schematic of the manipulation of extracellular calcium. Large open circles denote synaptic vesicles, small open circles denote possible slots for VGCCs in the model, small black circles denote VGCCs, and gray half-circles are a stylized representation of the calcium influx through open VGCCs. B: Average simulated synaptic delays at a range of extracellular calcium concentrations (1.8 mM Ca^{2+} is physiological). All comparisons made to 1.8 mM Ca^{2+} model: 0.9 mM Ca^{2+}: $P < 0.001$, 2.4 mM Ca^{2+}: $P < 0.001$, 3.6 mM Ca^{2+}: $P < 0.001$; 2-sided bootstrap test with Bonferroni correction, $\alpha = 0.001$, n = 100,000 bootstrap repetitions of average simulated synaptic delay. C: Average synaptic delays measured from an *ex vivo* frog NMJ preparation at 1.8 mM Ca^{2+} (physiological concentration) and at 0.5 mM Ca^{2+}; $P < 0.05$ 2-sided paired t-test, $\alpha = 0.05$, n = 22 pairs. D: Spatiotemporal calcium profile within the sampling box beneath synaptic vesicles triggered to fuse. E: Expansion of the time base to illustrate the 10–90% rise of the calcium profile plotted in D with best fit lines in light gray. Comparisons were made to the best fit line to the control (1.8 mM Ca^{2+}) model, 2-sided sum of squares F-test with Bonferroni correction, 0.9 mM Ca^{2+}: $P < 0.001$, 2.4 mM Ca^{2+}: $P < 0.001$, 3.6 mM Ca^{2+}: $P < 0.001$; $\alpha = 0.001$, n = 2,000 seeds for each condition). F: % calcium ion contributions from specific VGCCs to total bound calcium ions on vesicles triggered to fuse (denoted by large filled circle) for simulations using 0.9, 1.8 (control model), 2.4, or 3.6 mM Ca^{2+}. The main channel, the channel most closely associated with the vesicle triggered to fuse, is denoted by the small filled circle. All comparisons made to the main channel in the 1.8 mM Ca^{2+} model: 0.9 mM Ca2+: $P < 0.001$, 2.4 mM Ca^{2+}: $P < 0.001$, 3.6 mM Ca^{2+} $P < 0.001$; 2-sided bootstrap test with Bonferroni correction, $\alpha = 0.001$ with; n = 100,000 bootstrap repetitions of average ratio of calcium ions contributed to release. *Significant difference.

We next sought to investigate whether manipulating extracellular calcium caused shifts in the functional coupling of VGCCs to vesicle fusion, since changes in calcium concentration led to such dramatic changes in synaptic delay. We previously identified that vesicle fusion at the frog NMJ is primarily triggered by the single most closely associated VGCC (here termed “main channel”), with neighboring channels providing minimal contributions (Luo et al., 2015). However, changes in extracellular calcium concentration did not lead to a significant change in the average percentage of ions contributed by the main channel to vesicle fusion unless the

concentration was doubled to 3.6 mM Ca^{2+} [64.1% (SD = 1.5) vs. 74.3% (SD = 1.5) in 1.8 mM Ca^{2+}; Fig. 2.2F]. We also did not observe a significant change in the average number of VGCCs contributing to release, with 2.05 ± 0.01 VGCCs contributing in the control simulations (1.8 mM Ca^{2+}), 1.98 ± 0.05 VGGCs contributing in the 0.9 mM Ca^{2+}simulations, and 2.19 ± 0.01 VGCCs contributing in the 3.6 mM Ca^{2+} simulations (Table 2.1).

Table 2.1 Average number of VGCCs participating in release across experimental conditions.

Experimental Condition	Average No. of VGCCs Contributing Ions to Vesicle Fusion
Control (1.8 mM Ca^{2+}, 0-nm displacement, 26 VGCCs, 2 nM fixed buffer)	2.05 ± 0.0136
0.9 mM Ca^{2+}	1.98 ± 0.05
2.4 mM Ca^{2+}	2.09 ± 0.02
3.6 mM Ca^{2+}	2.19 ± 0.01*
5-nm VGCC displacement	2.13 ± 0.02*
10-nm VGCC displacement	2.21 ± 0.02*
15-nm VGCC displacement	2.36 ± 0.03*
20-nm VGCC displacement	2.41 ± 0.02*
4 VGCCs	1.11 ± 0.02*
13 VGCCs	1.54 ± 0.02*
52 VGCCs	3.11 ± 0.02*
0.2 mM fixed buffer	2.57 ± 0.10*
1 mM fixed buffer	2.26 ± 0.04*
8 mM fixed buffer	1.63 ± 0.10*

All comparisons made to control. Welch's two-sided t-test with Bonferroni correction, $\alpha = 0.001$. $P = 0.171$ for 0.9 mM Ca^{2+}, $P = 0.111$ for 2.4 mM Ca^{2+}, $P < 0.001$ for 3.6 mM Ca^{2+}, $P < 0.001$ for 5 nm, $P < 0.001$ for 10 nm, $P < 0.001$ for 15 nm, $P < 0.001$ for 20 nm, $P < 0.001$ for 4 VGCCs, $P < 0.001$ for 13 VGCCs, $P < 0.001$ for 52 VGGCs, $P < 0.001$ for 0.2 mM buffer, $P < 0.001$ for 1 mM buffer, $P < 0.001$ for 8 mM buffer. *Significant difference.

We next aimed to identify whether predictions from our simulations would hold when tested in an *ex vivo* frog NMJ preparation. Reducing extracellular calcium concentration from 1.8 mM in control recordings to 0.5 mM led to a significant slowing in synaptic delay from 2.25 ± 0.05 ms (control; 1.8 mM) to 2.69 ± 0.09 ms after perfusion with 0.5 mM Ca^{2+} NFR (Fig. 2.2C), a trend similar to what was observed in our modeling simulations (Fig. 2.2B). Our combined results from physiological experiments and modeling simulations indicate that synaptic delay is quite sensitive to changes in calcium concentration within the AZ at the time of vesicle release. Thus, we next manipulated a series of parameters that contribute to the spatiotemporal calcium dynamics within the AZ, including VGCC organization and density and buffer concentration.

2.3.3 Role of VGCC organization in synaptic delay

Since it has been demonstrated in a number of preparations that the spatial distance or coupling between VGCCs and release sensors on synaptic vesicles can affect the timing of neurotransmitter release (Eggermann et al. 2012; Wang and Augustine 2015), we first wanted to explore how the distance between VGCCs and release sensors contributed to synaptic delay in our preparation. We iteratively increased the distance between VGCCs and release sensor (synaptotagmin) sites on synaptic vesicles within the AZ (Fig. 2.3, A and B). We found that moving VGCCs by up to 20 nm from their original position (VGCCs were initially placed 39 nm from the bottom center of the vesicle) toward the midline of the AZ led to a roughly linear slowing in synaptic delay (Fig. 2.3C). We observed significant slowing when channels were displaced ≥ 10 nm from their original position, with mean synaptic delay increasing from 1.67 ms (SD = 0.04) in the control model (0-nm displacement) to 1.82 ms (SD = 0.05) when VGCCs were displaced by 20 nm (Fig. 2.3C).

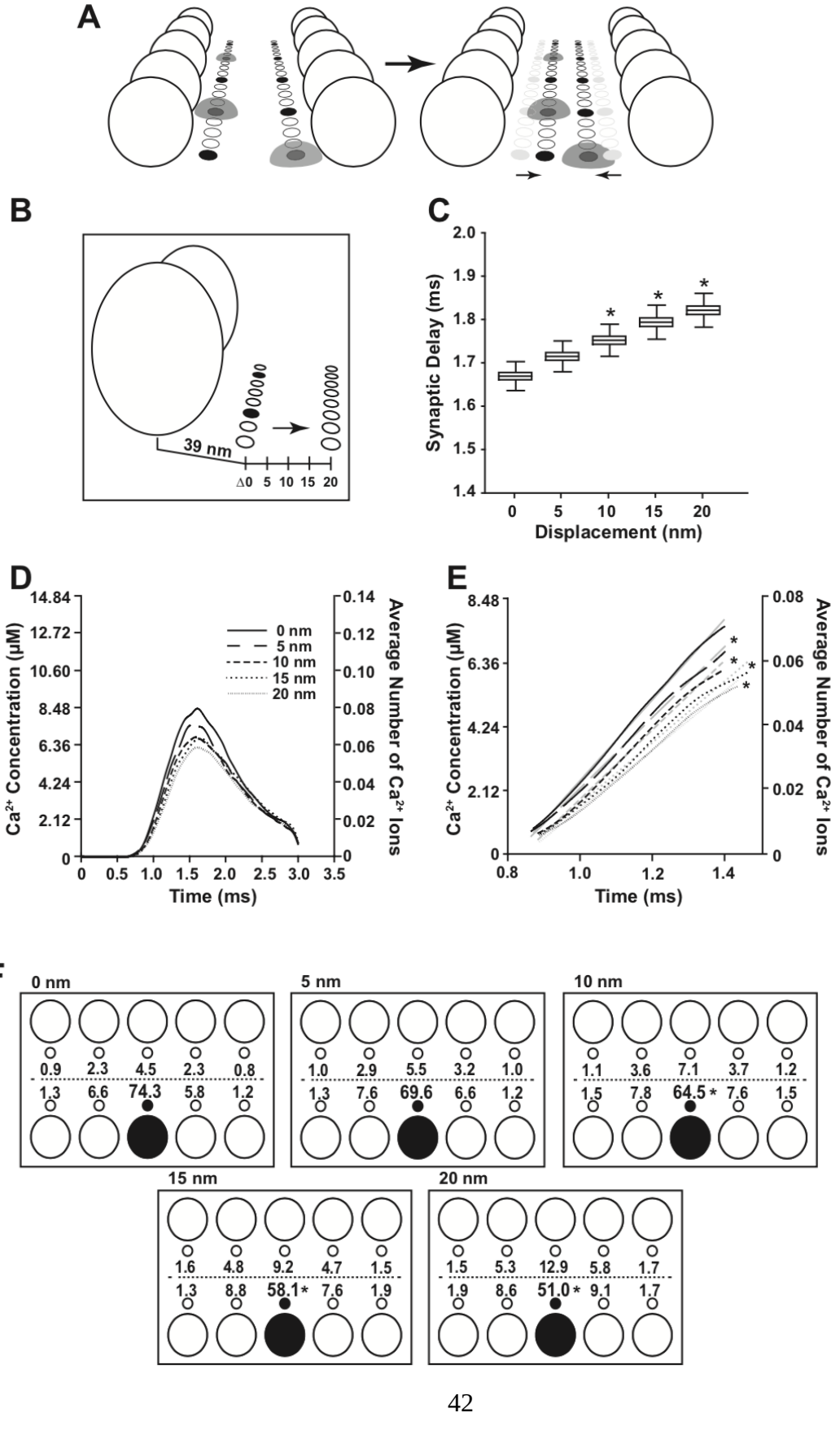
A
B
39 nm
Δ0 5 10 15 20
C
Synaptic Delay (ms)
Displacement (nm)
D
Ca2+ Concentration (μM)
Average Number of Ca2+ Ions
0 nm
5 nm
10 nm
15 nm
20 nm
Time (ms)
E
Ca2+ Concentration (μM)
Average Number of Ca2+ Ions
Time (ms)
F
0 nm
5 nm
10 nm
15 nm
20 nm

Figure 2.3 Role of VGCC organization on synaptic delay.

A: Schematic of the manipulation of VGCC placement. B: Schematic demonstrating the range of movement of channels within the AZ in our model. Control simulations (0-nm displacement) had VGCCs placed 39 nm from the bottom center of the vesicle based on published anatomical values (see Dittrich et al., 2013). C: Average simulated synaptic delay when VGCCs were displaced 5, 10, 15, or 20 nm from the control position (0 nm). All comparisons made to the 0-nm configuration: 5-nm displacement: $P = 0.0059$, 10-nm displacement: $P < 0.001$, 15-nm displacement: $P < 0.001$, 20-nm displacement: $P < 0.001$; 2-sided bootstrap test with Bonferroni correction, $\alpha = 0.001$, n = 100,000 bootstrap repetitions of average simulated synaptic delay. D: Spatiotemporal calcium profile within the sampling box beneath synaptic vesicles triggered to fuse. E: Expansion of the time base to illustrate the 10–90% rise of the calcium profile plotted in D with best fit lines in light gray. Comparisons were made to the best fit line to the control (0-nm displacement) model, 2-sided sum of squares F-test with Bonferroni correction: 5-nm displacement: $P < 0.001$; 10-nm displacement: $P < 0.001$; 15-nm displacement: $P < 0.001$; 20-nm displacement: $P < 0.001$; $\alpha = 0.001$, n = 2,000 seeds for each condition. F: % calcium ion contributions from specific VGCCs to total bound calcium ions on vesicles triggered to fuse (denoted by large filled circle). All comparisons made to the main channel in the 0-nm configuration (calculated as described for Fig. 2.2): 5-nm displacement: $P = 0.004$; 10-nm displacement: $P < 0.001$; 15-nm displacement: $P < 0.001$; 20-nm displacement: $P < 0.001$; 2-sided bootstrap test with Bonferroni correction, $\alpha = 0.001$, n = 100,000 bootstrap repetitions of average ratio of calcium ions contributed to release. *Significant difference.

Furthermore, when we explored the spatiotemporal calcium profile near the release sensors at the time of vesicle fusion we found that as we increased the VGCC displacement distance, the peak calcium concentration fell from 8.48 μM in the control (0-nm displacement) model to 5.75 μM in the 20-nm displacement model configuration (Fig. 2.3D). In addition, the slope of a line fit to the 10–90% rise time of the calcium profile was significantly different from the control model configuration in each of the displacement manipulations (92.74 ± 0.10 μM/ms in 20-nm displacement configuration vs. 126.97 ± 0.20 μM/ms in 0-nm configuration; Fig. 2.3E). These results suggest that the slowing we observe in synaptic delay as a result of increasing distances

between vesicle release sensors and VGCCs may be explained by the lower peak calcium concentration and slower accumulation of calcium ions around synaptic vesicles triggered to fuse as channels are moved further from release sensors, a hypothesis that was raised in another study of presynaptic structure-function relationships at the frog NMJ (Jung et al., 2016).

To gain a deeper understanding of the AZ transmitter release dynamics that were created by this spatiotemporal calcium profile, we again analyzed the functional coupling of VGCCs to vesicle fusion. In comparing the average percentage of ions contributed by the main channel (the VGCC directly associated with the vesicle triggered to fuse) in each of our displacement manipulations, we found that as distances between VGCCs and release sensors on vesicles increased, the main channel provided a significantly lower percentage of the calcium ions required for fusion [74.3% (SD = 1.5) in 0-nm displacement configuration vs. 51.0% (SD = 2.8) in 20-nm displacement configuration]. Accordingly, as VGCC-to-release sensor distances increased, more distant channels provided an increasingly greater percentage of the calcium ions bound to release sensors on vesicles compared with the control model (Fig. 2.3F). The buffered diffusion coefficient was measured as 2×10^{-7} cm^2/s and was found to be linearly related to distance (data not shown). Thus, it follows that the slowing we observe in synaptic delay is likely a result of increased diffusional times from calcium ions originating from more distant calcium sources, including a more distant main channel. Additionally, the average number of VGCCs participating in triggering vesicle fusion (contributing any calcium ions) increased from 2.05 ± 0.01 VGCCs in the control configuration (0 nm) to 2.41 ± 0.02 VGCCs in the 20-nm displaced configuration (Table 2.1), further supporting these conclusions.

2.3.4 Role of VGCC density in synaptic delay

Next, we sought to understand whether variations in VGCC density could contribute to heterogeneity in synaptic delay. We first varied the density of VGCCs within our AZ model to determine how the number of calcium sources in the AZ could influence synaptic delay (Fig. 2.4A). In control configurations, our frog AZ model had two rows of 13 VGCCs flanked by 26 docked synaptic vesicles (Ma et al., 2015). When we reduced the number of VGCCs in our model by 50% or 85%, leaving 13 or 4 VGCCs in the AZ, respectively, we found that average synaptic delay trended toward slowing, but the difference between the 26 VGCC control model [1.67 ms (SD = 0.39)] and the 4 VGCC model [1.72 ms (SD = 0.04)] was not statistically significant (note that the Bonferroni correction accounted for all manipulations in the parameter search, yielding a more conservative statistical analysis). Conversely, when we doubled the number of VGCCs in the AZ (52 channels) we observed a significantly faster synaptic delay that averaged 1.59 ms (SD = 0.04) (Fig. 2.4B).

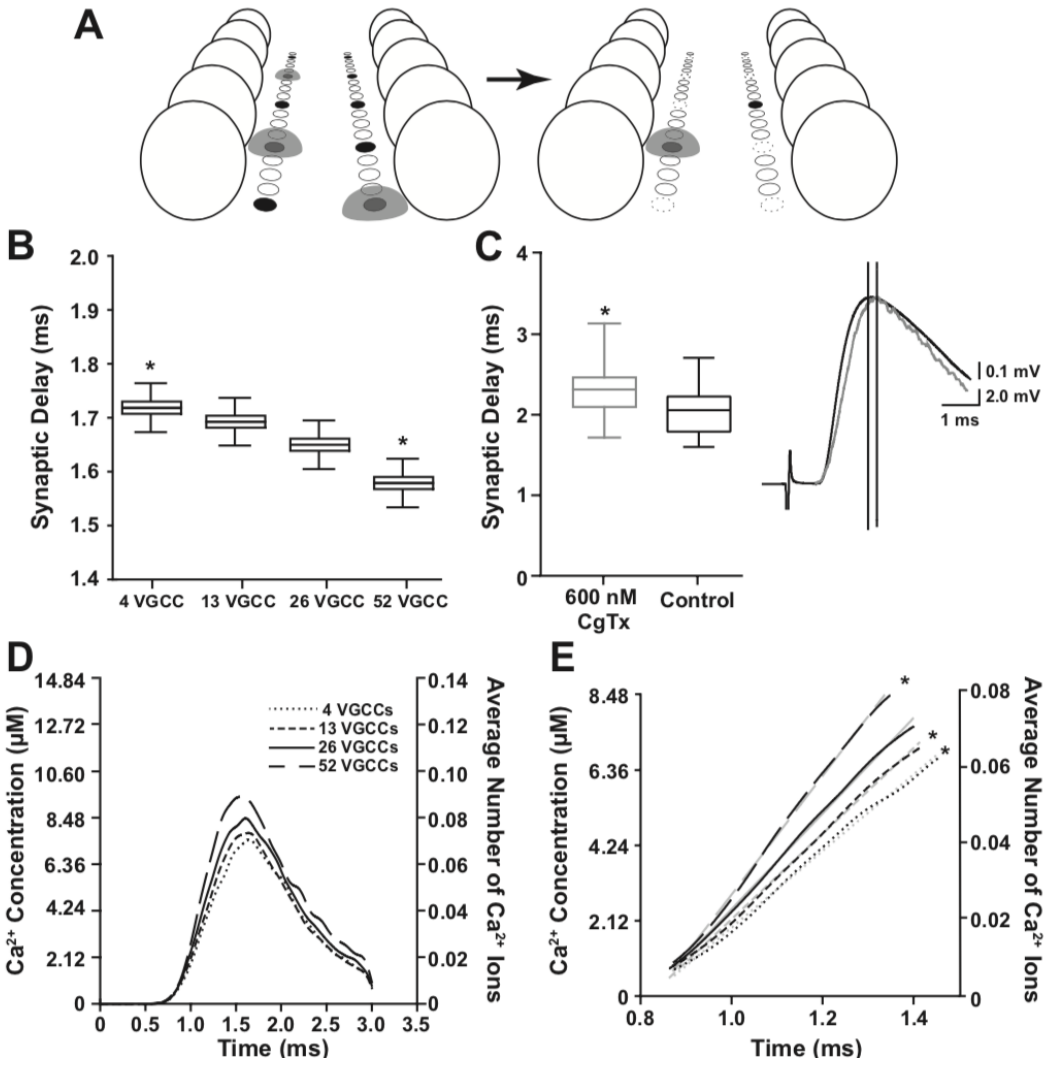
A
B
Synaptic Delay (ms)
2.0
1.9
1.8
1.7
1.6
1.5
1.4
*
*
4 VGCC
13 VGCC
26 VGCC
52 VGCC
C
Synaptic Delay (ms)
4
3
2
1
0
*
600 nM CgTx
Control
0.1 mV
2.0 mV
1 ms
D
Ca2+ Concentration (μM)
14.84
12.72
10.60
8.48
6.36
4.24
2.12
0
4 VGCCs
13 VGCCs
26 VGCCs
52 VGCCs
0 0.5 1.0 1.5 2.0 2.5 3.0 3.5
Time (ms)
Average Number of Ca2+ Ions
0.14
0.12
0.10
0.08
0.06
0.04
0.02
0
E
Ca2+ Concentration (μM)
8.48
6.36
4.24
2.12
0
*
*
*
0.8 1.0 1.2 1.4
Time (ms)
Average Number of Ca2+ Ions
0.08
0.06
0.04
0.02
0

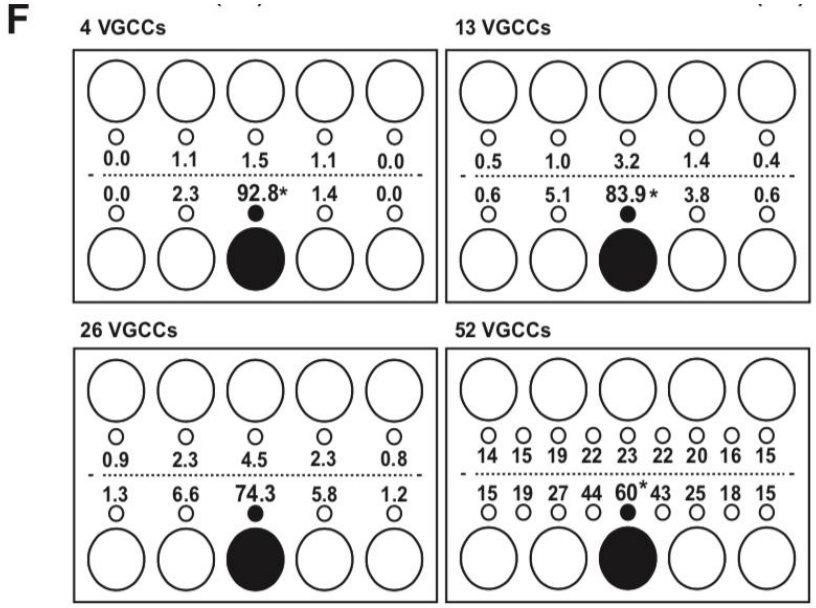

Figure 2.4 Role of VGCC density on synaptic delay.

A: Schematic representing manipulation of the density of VGCCs. B: Average simulated synaptic delays when there are 52, 26 (control model), 13, or 4 VGCCs in the model AZ. All comparisons made to the 26 VGCC configuration: 52 VGCCs: $P < 0.001$; 13 VGCCs: $P = 0.035$; 4 VGCCs: $P = 0.002$; 2-sided bootstrap test, $\alpha = 0.001$ with Bonferroni correction; n = 100,000 bootstrap repetitions of average simulated synaptic delay. C: Average synaptic delays measured from an ex vivo frog NMJ preparation before and after application of 600 nM conotoxin (CgTx) GVIA; $P < 0.05$, 2-sided paired t-test, $\alpha = 0.05$, degrees of freedom = 31; n = 32 pairs. D: Spatiotemporal calcium profile within the sampling box beneath synaptic vesicles triggered to fuse. E: Expansion of the time base to illustrate the 10–90% rise of the calcium profile plotted in D with best fit lines in light gray. Comparisons were made to the best fit line to the control (26 VGCC displacement) model, 2-sided sum of squares F-test with Bonferroni correction: 52 VGCCs: $P < 0.001$; 13 VGCCs: $P < 0.001$; 4 VGCCs: $P < 0.001$; $\alpha = 0.001$, n = 2,000 seeds for each condition. F: % calcium ion contributions from specific VGCCs to total bound calcium ions on vesicles triggered to fuse (denoted by large filled circle) for simulations with 4, 13, 26 (control model), or 56 VGCCs in the AZ (calculated as described for Fig. 2.2). All comparisons made to the main channel in the 26 VGCC configuration: 52 VGCCs: $P < 0.001$; 13 VGCCs: $P = 0.004$; 4 VGCCs: $P < 0.001$; 2-sided bootstrap test with Bonferroni correction, $\alpha = 0.001$, n = 100,000 bootstrap repetitions of average ratio of calcium ions contributed to release. *Significant difference.

In understanding the sub-AZ calcium dynamics that could contribute to these changes in synaptic delay, we again compared the calcium profile under synaptic vesicles triggered to fuse. We found that as the number of VGCCs was reduced, the peak calcium concentration under each vesicle that fused decreased within the sampling box from 8.48 μM in the 26 VGCC (control) model to 7.47 μM in the 4 VGCC model (Fig. 2.4D). Furthermore, the slopes of lines fit to the rise of the calcium profile were significantly slower [126.97 ± 0.20 μM/ms in 26 VGCC (control) configuration vs. 101.66 ± 0.17 μM/ms in 4 VGCC configuration; Fig. 2.4E], potentially providing an explanation for the slowing trend we observed in synaptic delay. Conversely, we found that as the number of VGCCs in the AZ was doubled from 26 to 52, the peak calcium concentration increased to 9.39 μM and the slope of the best fit line to the rise of the calcium profile in the sampling box was significantly faster (157.57 ± 0.33 μM/ms; Fig. 2.4E). While there was only a significant change in synaptic delay when the number of VGCCs was doubled, each manipulation led to a faster rise in the calcium profile around a synaptic vesicle triggered to fuse. These data suggest that changes to the calcium profile may not be the only mechanism that influences synaptic delay.

We next analyzed whether the functional coupling of VGCCs to vesicle fusion was altered in each of the VGCC density manipulations. We found that as the number of VGCCs in the model was decreased to just four channels, the main channel provided an increasingly greater percentage of the calcium ions required for vesicle fusion [92.8% (SD = 0.93) in 4 VGCC configuration vs. 74.3% (SD = 1.5) in 26 VGCC configuration; Fig. 2.4F]. Conversely, as the number of channels was increased, we found that the main channel provided a significantly lower proportion of the calcium ions that bound to the nearby vesicle when it was triggered to fuse [60.0% (SD = 1.7) in 52 VGCC configuration; Fig. 2.4F]. This trend is reflected in the average number of VGCCs

contributing calcium ions to release, with 2.05 ± 0.01 VGCCs contributing ions to release in the control model (26 VGCCs), 3.11 ± 0.02 VGCCs in the 52 VGCC configuration, and 1.11 ± 0.02 channels in the 4 VGCC configuration (Table 2.1). These data suggest that at the frog NMJ, while a single channel (main channel) can provide all of the necessary calcium ions for release, release proceeds more quickly when nearby channels also contribute. Additionally, for seeds in which the main channel contributes all of the calcium ions required for vesicle fusion in the control model configuration, synaptic delay also slows (1.71, SD = 0.39 ms when the main channel provides all of the ions for fusion vs. 1.67, SD = 0.32 ms when neighboring channels also contribute ions for fusion; $\alpha = 0.05$, 2-sided unpaired t-test, $P < 0.05$), providing further evidence for this hypothesis.

Using the results from our computational model as a guide, we also performed recordings in an *ex vivo* frog NMJ preparation to determine whether variations in VGGC density led to similar changes in synaptic delay. We reduced the number of functional VGCCs by using a specific antagonist for CaV2.2 channels, the primary subtype of VGCCs at the frog NMJ. Specifically, we used a 30-min exposure to 600 nM ω-conotoxin GVIA to block ~95% of transmitter release. As predicted by our modeling simulations (Fig. 2.4B), we found that reducing the number of available CaV2.2 VGCCs led to a significant slowing in synaptic delay from 2.04 ± 0.05 ms before application of conotoxin to 2.33 ± 0.06 ms after application of conotoxin (Fig. 2.4C). Therefore, when most VGCCs are pharmacologically blocked in the AZ, synaptic delay slows, with trends similar to what we observed in our modeling simulations (especially the 4 VGCC model configuration). These results suggest that VGCC density can be an important factor in shaping synaptic delay at the frog NMJ.

2.3.5 Role of buffer concentration in synaptic delay

Finally, we investigated the role of manipulation of fixed calcium buffer concentration within our model (see Ma et al., 2015) in synaptic delay (Fig. 2.5A). We first reduced the fixed buffer concentration from 2 mM in control simulations to either 1 or 0.2 mM. However, only when fixed buffer concentration was reduced to 0.2 mM was synaptic delay significantly faster, from 1.67 ms (SD = 0.04) in the 2 mM buffer simulations to 1.55 ms (SD = 0.31) in the 0.2 mM buffer simulations. Conversely, if the buffer concentration was increased to 8 mM, synaptic delay was significantly slower [1.82 ms (SD = 1.0); Fig. 2.5B].

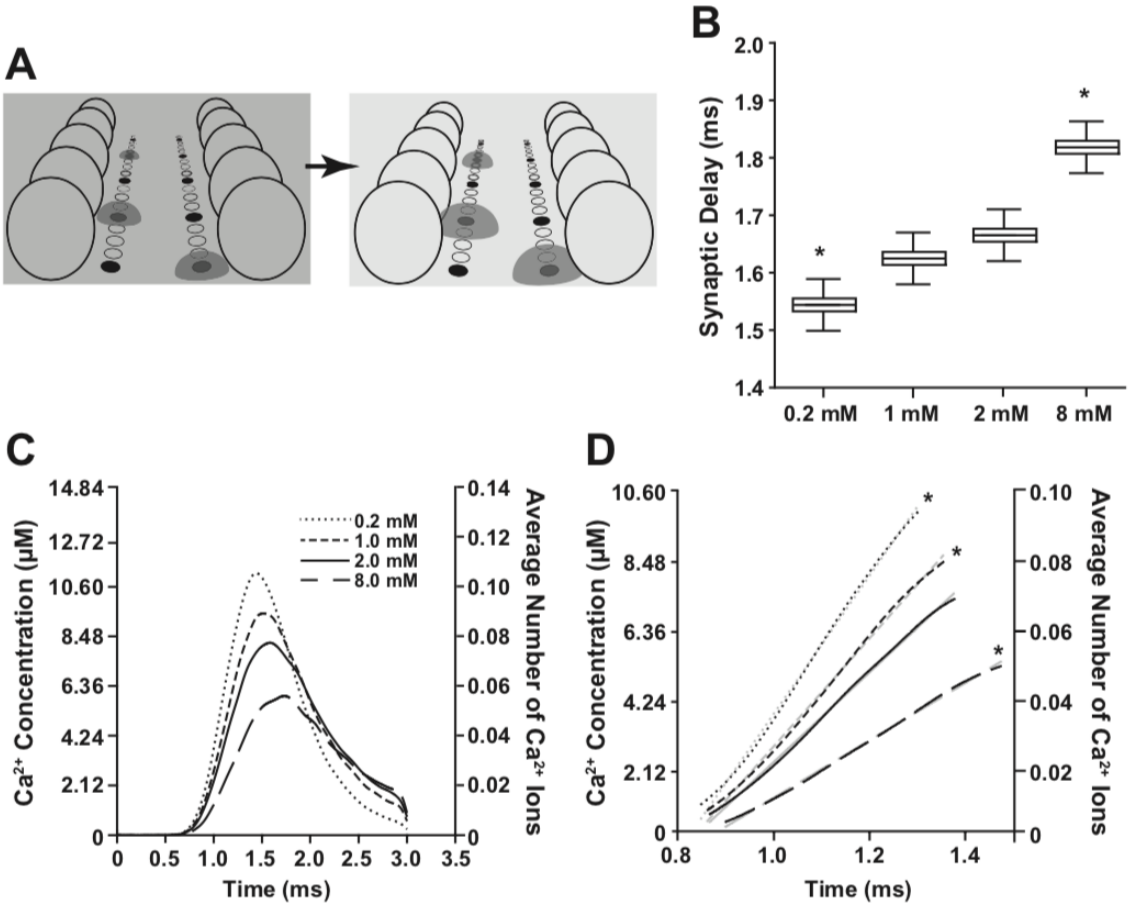
A
B
Synaptic Delay (ms)
2.0
1.9
1.8
1.7
1.6
1.5
1.4
0.2 mM
1 mM
2 mM
8 mM
C
Ca2+ Concentration (μM)
Average Number of Ca2+ Ions
Time (ms)
0.2 mM
1.0 mM
2.0 mM
8.0 mM
D
Ca2+ Concentration (μM)
Average Number of Ca2+ Ions
Time (ms)

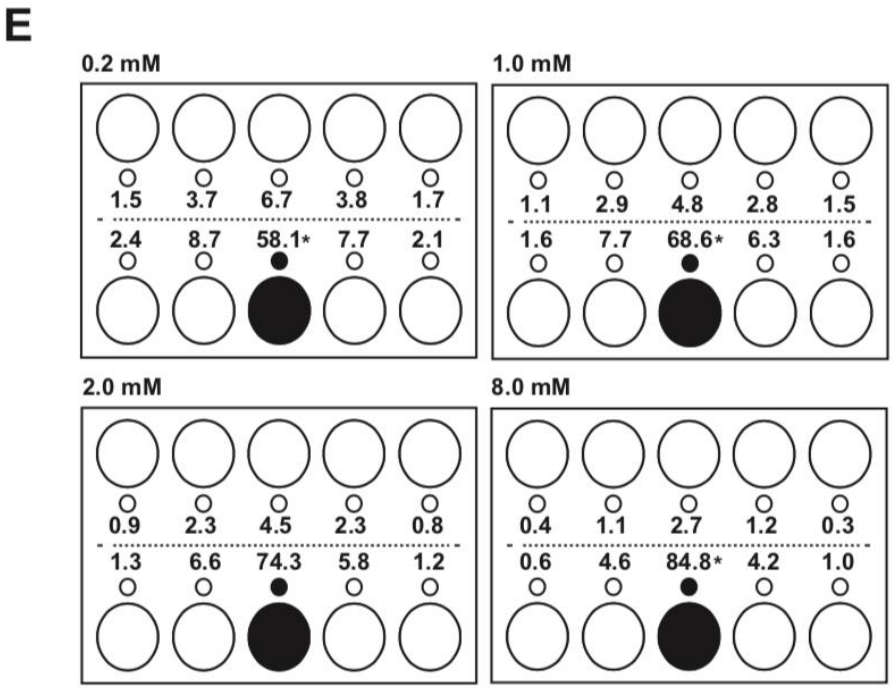
E
0.2 mM
1.5 3.7 6.7 3.8 1.7
2.4 8.7 58.1* 7.7 2.1
1.0 mM
1.1 2.9 4.8 2.8 1.5
1.6 7.7 68.6* 6.3 1.6
2.0 mM
0.9 2.3 4.5 2.3 0.8
1.3 6.6 74.3 5.8 1.2
8.0 mM
0.4 1.1 2.7 1.2 0.3
0.6 4.6 84.8* 4.2 1.0

Figure 2.5 Role of fixed buffer concentration on synaptic delay.

A: Schematic representing modulation of buffer concentration (light gray background depicts lower calcium buffer than dark gray background). B: Average simulated synaptic delays with 0.2, 1.0, 2.0 (control), and 8.0 mM fixed buffer. All comparisons made to the 2.0 mM manipulation: 0.2 mM: $P < 0.001$; 1.0 mM: $P = 0.035$; 8.0 mM: $P = 0.002$; 2-sided bootstrap test, $\alpha = 0.001$ with Bonferroni correction; n = 100,000 bootstrap repetitions of average simulated synaptic delay. C: Spatiotemporal calcium profile within the sampling box beneath synaptic vesicles triggered to fuse. D: Expansion of the time base to illustrate the 10–90% rise of the calcium profile plotted in C with best fit lines in light gray. Comparisons were made to the best fit line to the control (2 mM) configuration, 2-sided sum of squares F-test with Bonferroni correction: 0.2 mM: $P < 0.001$; 1.0 mM: $P < 0.001$; 8 mM: $P < 0.001$; $\alpha = 0.001$, n = 2,000 seeds for each condition. E: % calcium ion contributions from specific VGCCs to total bound calcium ions on vesicles triggered to fuse (denoted by large filled circle) for simulations with 0.2, 1.0, 2.0 (control model), or 8.0 mM in the AZ (calculated as described for Fig. 2.2). All comparisons made to the main channel in the 2.0 mM configuration: 0.2 mM: $P < 0.001$; 1.0 mM: $P < 0.001$; 8.0 mM: $P < 0.001$; 2-sided bootstrap test with Bonferroni correction, $\alpha = 0.001$, n = 100,000 bootstrap repetitions of average ratio of calcium ions contributed to release. *Significant difference.

To understand the sub-AZ calcium dynamics that could shape these changes in synaptic delay, we again analyzed the calcium profile under synaptic vesicles triggered to fuse. When buffer was reduced to either 1 or 0.2 mM, the peak amplitude of the calcium profile increased from 8.48 µM in control to 9.49 µM in 1 mM buffer and 11.21 µM in 0.2 mM buffer. The slope of the lines fit to the 10–90% rise of the profile also were significantly faster than control (128.66 µM/ms) in both conditions (154.94 µM/ms in 1 mM buffer simulations and 198.28 µM/ms in 0.2 mM buffer simulations; Fig. 2.5, C and D). Conversely, when buffer was increased from 2 mM to 8 mM, the amplitude of the calcium profile was reduced, from 8.48 to 5.96 µM, and the slope of the line fit to the 10–90% rise of the calcium profile was slower (2 mM: 128.66 µM/ms, 8 mM: 82.47 µM/ms; Fig. 2.5, C and D). These data indicate that buffer concentration is critical in shaping

spatiotemporal calcium dynamics within the AZ at the time of vesicle fusion and likely contributes to shaping synaptic delay.

To understand how buffer concentration affects the functional coupling of VGCCs to vesicle fusion, we analyzed the average percentage of ions contributed by each VGCC to fusion in the different concentrations of fixed buffer. When buffer concentration was reduced to either 1.0 or 0.2 mM, the main channel provided a significantly lower percentage of ions for release [74.3 ± 1.5% in control (2 mM), 68.6 ± 2.6% in 1.0 mM, and 58.1 ± 2.9% in 0.2 mM] while more distant channels provided an increasingly greater percentage. Conversely, when buffer concentration was increased to 8.0 mM, the main channel contributed a significantly greater percentage of ions for vesicle fusion [84.8% (SD = 2.5); Fig. 2.5E]. Furthermore, the number of VGCCs contributing ions to vesicles triggered to fuse increased significantly (from 2.05 ± 0.01 to 2.57 ± 0.10) when buffer was reduced to 0.2 mM and decreased significantly (from 2.05 ± 0.01 to 1.63 ± 0.10) when buffer was increased to 8.0 mM (Table 2.1). These data suggest that as calcium buffer concentration is increased calcium ions triggering fusion are derived primarily from the channel most closely associated with the vesicle triggered to fuse.

2.4 Discussion

Using our computational model of a frog NMJ AZ, we explored the impact of several parameters on synaptic delay. Synaptic delay appeared to be most sensitive to changes in extracellular calcium concentration, which was underpinned by significant changes in the spatiotemporal calcium profile (Fig. 2.2). Manipulating buffer concentration also appeared to have a strong impact on synaptic delay while also causing large shifts in the spatiotemporal calcium profile (Fig. 2.5). However,

increasing the distance between VGCCs and synaptic vesicles or removing significant numbers of VGCCs from the AZ led to more modest slowing of synaptic delay and smaller shifts in the spatiotemporal calcium profile (Fig. 2.3 and Fig. 2.4). These data suggest that AZ changes that lead to the largest changes in calcium dynamics around a vesicle at the time of release may be most likely to influence synaptic delay. Furthermore, predictions made from our model were validated by similar experimental manipulations (Fig. 2.2C, Fig. 2.4C), providing evidence that the variability we observe in synaptic delay across synapses could, in part, be due to differences in the average concentration of buffer within AZs and/or in the density and organization of VGCCs. The modeling approach taken here does not allow us to determine which specific mechanisms are responsible for the wide variability in synaptic delay observed between individual NMJs but rather to predict the sensitivity of synaptic delay to such AZ changes. With this information in hand, it is possible to explore these predictions in future experiments where the combinatorial effect of these parameters on synaptic delay may be studied in greater depth. Furthermore, our data impact several issues in the field that have been proposed regarding the organization of AZ proteins and their effect on the properties of calcium-triggered transmitter release.

2.4.1 AZ structure and functional coupling of VGCCs to vesicle fusion

A large effort has been made in the field to classify vesicle release at a synapse as either single domain (gated primarily by a single VGCC) or multidomain (gated by a collection of channels in the AZ) gated (Stanley, 2016). Furthermore, it has been tempting to ascribe general synaptic characteristics to each release-gating scheme. For example, synapses where vesicle release is gated primarily by a single, closely associated VGCC are often described as “fast” synapses. Conversely,

synapses where release is gated by a collection of nearby VGCCs are described as having greater potential for plasticity (Eggermann et al., 2012). Our results demonstrate that at the frog neuromuscular synapse, when a single channel (single-domain gating) provides nearly all of the ions for fusion, that vesicle fusion is actually slower than when nearby channels are able to contribute (Fig. 2.4F and Table 2.1; 4 VGCC model). We have previously demonstrated in our frog NMJ AZ model that the main channel provides only 75% of the ions required for vesicle fusion (Luo et al., 2015), with other nearby channels providing a small but critical proportion. These data suggest that the frog NMJ may exhibit single-domain- "like" gating, where transmitter release is triggered more quickly and efficiently when one channel predominates but a collection of nearby VGCCs also contribute ions.

Our data also demonstrate that the functional coupling exhibited by a synapse depends in part on the structure and organization of its AZs. We show that the density and organization of VGCCs in the AZ can lead to significant changes in the contribution of ions provided by the main VGCC, as well as the number of VGCCs contributing any ions to vesicle fusion (Fig. 2.3F, Fig. 2.4F, Table 2.1). However, manipulating either extracellular calcium or buffer concentration did not affect the functional coupling of VGCCs to vesicle fusion as dramatically as manipulating VGCC density or organization (Fig. 2.2F, Fig. 2.5E). Even when calcium was reduced to 0.9 mM, there was no significant change in either the number of VGCCs contributing ions to vesicle fusion or the percentage of ions contributed by the main channel. These data suggest that understanding how VGCCs gate vesicle release (and how that correlates to functional relevance for the synapse) requires an understanding of both AZ structure and the spatiotemporal calcium profile that arises from that structure.

2.4.2 Plasticity of structure-function relationships at AZs

Presynaptic AZs are highly plastic with respect to the number and distribution of ion channels and release machinery proteins, which influences a variety of measurements beyond synaptic delay, including the probability of release and short-term plasticity (Baur et al., 2015; Sheng et al., 2012). Thus, it is likely that the density and organization of VGCCs within AZs may vary as a mechanism by which a synapse is able to finely control a variety of physiological functions. With regard to synaptic delay, this form of structural plasticity may be important at synapses that have high-temporal fidelity demands including those in motor and sensory systems, where the precise timing of postsynaptic activation is critical to function of the synapse as a whole.

3.0 Transmitter release site organization can predict synaptic function at the neuromuscular junction[3]

3.1 Introduction

Chemical transmitter release from presynaptic nerve terminals is triggered by the influx of calcium ions (Ca^{2+}) through voltage-gated Ca^{2+} channels (VGCCs), which bind to Ca^{2+} sensor proteins on docked synaptic vesicles, triggering vesicle fusion with the plasma membrane. These events occur within specialized active zone (AZ) regions of the nerve terminal where presynaptic VGCCs colocalize with proteins that regulate synaptic vesicle docking and fusion. Historically, several preparations have been used to investigate the significance of AZ structure for synaptic function (Zhai and Bellen, 2004), but the results from these studies have not been in agreement. For example, studies of phasic and tonic synapses in the crayfish neuromuscular junction (NMJ) concluded that AZ structure was not a critical determinant of synaptic function (Millar and Atwood, 2004; Walrond and Reese, 1985). However, more recent studies have pointed to the importance of AZ organization for synaptic function. For example, studies of hippocampal synapses in the rodent central nervous system (CNS) characterized the structure and organization of AZs (Rollenhagen et al., 2007) and showed that release probability scales with AZ size

[3] This chapter was published as: Laghaei R, Ma, J, Tarr TB, Homan AE, Kelly L, Tilvawala MS, Vuocolo BS, Rajasekaran HP, Meirney SD, Dittrich M. Transmitter release site organization can predict synaptic function at the neuromuscular junction. *J Neurophysiol* 119, 2018. Reproduced with permission from the American Physiological Society.

(Holderith et al., 2012). Scimemi and Diamond (2012) also predicted that sub-AZ organization and the number of presynaptic VGCCs at hippocampal synapses could critically influence synaptic function. Similarly, recent investigations at the large calyx of Held synapse in the rodent brain stem have shown that VGCC number and position relative to synaptic vesicle release sites regulate synaptic strength and plasticity (Han et al., 2011; Sheng et al., 2012). At neuromuscular synapses, AZ structure has long been a focus of investigation (Harlow et al., 2001; Heuser and Reese, 1974, 1981; Nagwaney et al., 2009; Pawson et al., 1998; Propst et al., 1986), and previous studies have sought to link VGCC number and position within AZs to synaptic function (Bennett et al., 1997; Chen et al., 2011; Luo et al., 2015; Shahrezaei et al., 2006). Furthermore, several groups have used computer modeling to explore the spatiotemporal profile of Ca^{2+} influx and the importance of this dynamic process on synaptic vesicle fusion within AZs (Bennett et al., 2000a, 2000b, 2004; Dittrich et al., 2013; Fogelson and Zucker, 1985; Matveev et al., 2011).

Here we further investigated the relationship between AZ structure and synaptic function using a previously published MCell (Monte Carlo Cell) computer model of the well-defined and highly ordered frog NMJ AZ (validated by the ability of this model to predict a large number of physiological phenomena at this synapse; Dittrich et al., 2013; Ma et al., 2015) and a simple rearrangement of the VGCCs and docked synaptic vesicles in this model into the organization predicted at the mouse NMJ AZ. Recent electron microscopy tomography studies have highlighted significant differences in the highly ordered fine structure of frog and mouse NMJ AZs (Harlow et al., 2001; Nagwaney et al., 2009). Frog AZs are tightly organized into long linear structures consisting of two double rows of presynaptic proteins (thought to include VGCCs) sandwiched between a double row of ~30 docked synaptic vesicles (Fig. 3.1A). In contrast, AZs at the mouse NMJ are characterized by relatively short AZ segments consisting of two synaptic vesicles and a

double row of synaptic proteins on either side (Fig. 3.1B). We have taken advantage of the well-known and highly ordered structures of neuromuscular AZs to investigate if the characteristic structural differences between frog and mouse NMJ AZs are important determinants of synaptic function. We demonstrate, using a combination of physiological recordings, anatomical investigations, and MCell computer simulations, that differential organization of neuromuscular AZs between frog and mouse could indeed explain the observed differences in probability of release and short-term plasticity characteristics at these synapses. We conclude that our MCell computer model predicts that the differential assembly of the basic building blocks of synapses (presynaptic VGCCs and docked synaptic vesicles within presynaptic AZs) can result in synapses with significantly different functional properties.

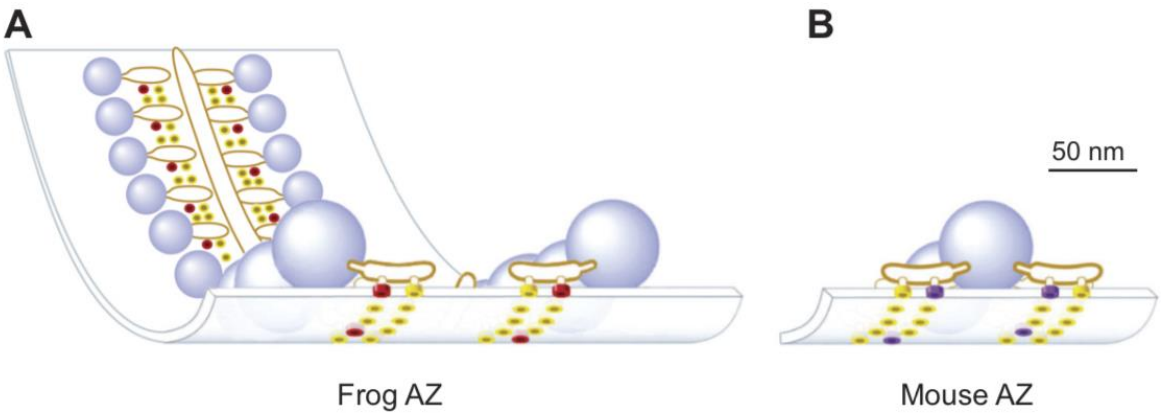

Figure 3.1 Schematic diagrams of single active zone (AZ) organization within the frog (A) and mouse (B) neuromuscular junction (NMJ).

Blue spheres = docked synaptic vesicles. Yellow disks = AZ membrane proteins of unknown identity. Red disks = Cav 2.2 type VGCCs. Purple disks = Cav 2.1 type VGCCs. [Adapted from Urbano et al., 2003 with permission from National Academy of Sciences. Copyright (2003) National Academy of Sciences, U.S.A.]

3.2 Materials and Methods

3.2.1 Intracellular recordings at frog NMJs

Adult male and female northern frogs (*Rana pipiens*) were obtained in the winter and anesthetized in 0.6% tricaine methane sulfonate (Sigma-Aldrich, St. Louis, MO) in normal frog saline (NFR; 116 mM NaCl, 2 mM KCl, 5mM dextrose, 10 mM HEPES, 1 mM $MgCl_2$, 1.8 mM $CaCl_2$, pH 7.3–7.4) and double pithed. The cutaneous pectoris nerve-muscle preparation was dissected, the nerve was stimulated with a suction electrode, and muscle contractions were blocked by exposure to 1 μM μ-conotoxin PIIIA (Alomone Laboratories, Jerusalem, Israel), a peptide toxin that specifically blocks sodium channels on frog muscle fibers (Shon et al., 1998). All recordings were made at room temperature unless otherwise noted.

Since the time course of multiquantal release during action potential stimuli is distributed slightly in time, quantal content is most accurately calculated as the ratio of the integrals of end-plate currents (EPCs) to the integrals of miniature end-plate currents (mEPCs). To make these accurate measurements of quantal content, two-electrode voltage clamp was used. Voltage-clamp recordings were performed as described previously (supplement of Dittrich et al., 2013). Briefly, microelectrodes were pulled to a resistance of 5–10 MΩ and filled with 3 M potassium chloride. Spontaneous miniature synaptic currents (mEPCs) were collected for 1–2 min in each muscle fiber, and 10–20 single nerve-evoked synaptic currents (EPCs) were collected with an interstimulus interval of 5 s. All voltage-clamp recordings at frog NMJs were made using a holding potential of −85 mV. To calculate quantal content, the integral of the average EPC waveform was divided by the integral of the average mEPC waveform recorded from each muscle fiber. This ratio calculates the average number of quanta that are released following each nerve stimulation.

For measurements of short-term plasticity where relative changes in evoked end-plate potential (EPP) amplitude were measured, current-clamp recordings were performed as described previously (Douthitt et al., 2011; Meriney and Grinnell, 1991). Briefly, postsynaptic receptors were partially blocked (using a 10-min exposure to 10 μg/ml alpha-bungarotoxin) such that the amplitude of evoked responses (EPPs) was less than 15 mV. Intracellular recordings of EPPs were made using ~40–60 MΩ borosilicate electrodes filled with 3 M potassium acetate. For these experiments, a pair of EPPs or a train of 5–10 EPPs with varying interstimulus intervals (10–100 Hz) was collected, and relative changes in EPP amplitude were normalized by dividing the amplitude of the second EPP in a pair, or each EPP in a train, by the amplitude of the first EPP in the pair or train.

3.2.2 Intracellular recordings at mouse NMJs

Since the size of the NMJ, and therefore the number of AZs, increases with age (Chen et al., 2012), we restricted the age window of mice used in our study to 1- 2 months of age for both estimations of quantal content and AZ counting (bassoon immunohistochemistry). Female mice (outbred Swiss Webster) were euthanized by CO_2 inhalation followed by thoracotomy, and intracellular recordings of transmitter release were made from the epitrochleoanconeus (ETA) *ex vivo* nerve-muscle preparation as previously described (Tarr et al., 2013a). Briefly, the extracellular saline (normal mammalian Ringer; NMR) contained 150 mM NaCl, 5 mM KCl, 11 mM dextrose, 10 mM HEPES, 1 mM $MgCl_2$, and 2 mM $CaCl_2$ (pH 7.3–7.4). The nerve was stimulated with a suction electrode, and muscle contractions were blocked by exposure to 1 μM μ-conotoxin GIIIB (Alomone Laboratories), a peptide toxin that specifically blocks sodium channels on mouse muscle fibers (Hong and Chang, 1989). All measurements were made at room temperature (except as

noted). For all experiments using mouse neuromuscular synapses, the tissue was oxygenated throughout the dissection and recording period.

For measurements of quantal content, two-electrode voltage-clamp was used (as described above). Spontaneous mEPCs were collected for 1–2 min in each muscle fiber, and then 10–20 EPCs were collected with an interstimulus interval of 5 s. All voltage-clamp recordings at mouse NMJs were made using a holding potential of −90 mV. Quantal content was calculated as described above.

For measurements of short-term plasticity, current-clamp microelectrode recordings were performed using ~40–60 MΩ borosilicate electrodes filled with 3 M potassium acetate. To evaluate effects on short-term synaptic plasticity, either a pair of EPPs or a train of 10 EPPs with varying interstimulus intervals (10–100 Hz) was collected, and relative changes in EPP amplitude were calculated as described above.

3.2.3 Analysis of electrophysiology data

All electrophysiology data from frog and mouse preparations were collected using an Axoclamp 900A and digitized at 10 kHz for subsequent analysis using pClamp 10 software. All recordings (voltage and current clamp) were corrected for nonlinear summation (McLachlan and Martin, 1981). For voltage-clamp recordings, EPCs were also corrected by considering the driving force [DF = membrane potential – equilibrium potential for acetylcholine receptor channels (Eq_{AChR} was set to 0 mV)] and voltage error [VE; where $EPC_{corrected} = EPC_{measured} \times (DF / (DF - VE))$].

3.2.4 Quantification of active zones at frog NMJs

To quantify the number of presynaptic AZs in frog NMJs, the postsynaptic acetylcholine receptor bands were labeled because this has been established as a highly predictive method for identifying the location of presynaptic AZs at the frog NMJ (Cohen et al., 1991; Robitaille et al., 1990). For these experiments, the cutaneous pectoris *ex vivo* nerve-muscle preparation was dissected and placed in an extracellular saline (NFR as described above) containing 3 μg/ml Alexa 594-conjugated α-bungarotoxin (BTX; Thermo Fisher Scientific, Pittsburgh, PA) for 30 min to label the postsynaptic acetylcholine receptors. This was followed by a 30-min incubation in 5 μg/0.1 ml Alexa 488-peanut lectin (PNA; Thermo Fisher Scientific) to label the extracellular matrix around the nerve terminals and identify the spatial extent of each synapse. The tissue was then washed and fixed in 2% (wt/vol) paraformaldehyde in phosphate-buffered saline (PBS) for 20 min at room temperature and mounted on glass slides under no. 1.5 cover glass using Prolong Gold mounting media (Thermo Fisher Scientific).

3.2.5 Quantification of active zones at mouse NMJs

To count the number of AZs in mouse NMJs, labeling of the presynaptic protein bassoon has been shown to be an effective and highly localized marker (Nishimune et al., 2004; Nishimune, 2012). For these experiments, the ETA *ex vivo* nerve-muscle preparation was dissected and placed in an extracellular saline (NMR as described above) containing ~3 μg/ml Alexa 594-conjugated α-BTX for 30 min to label the postsynaptic acetylcholine receptors. The tissue was then washed and fixed in 2% (wt/vol) paraformaldehyde in phosphate-buffered saline (PBS) for 20 min at room temperature. The fixed tissue was then permeabilized and blocked in a PBS solution containing

2% (wt/vol) bovine serum albumin (BSA), 2% (vol/vol) normal goat serum, and 0.5% Triton X-100. After block, the tissue was incubated in the primary antibody (1:600 dilution of SAP7F407 clone of mouse anti-bassoon IgG subtype 2a; Assay Designs no. VAM-PS003) for 12–16 h on a rocker platform at room temperature. Following washout of the primary antibody, the tissue was incubated in the secondary antibody (1:1,000 dilution of Alexa-488 goat anti-mouse IgG 2a; Molecular Probes no. A21131) for 4–6 h on a rocker platform at room temperature. Finally, after washing in PBS, the tissue was mounted on glass slides under no. 1.5 cover glass using Prolong Gold mounting media.

3.2.6 Confocal imaging

Mounted tissue was imaged on a Leica TCS SP5 spectral confocal microscope. Alexa-488 labeling was imaged using 488-nm laser excitation and photon collection between 498 and 560 nm. Alexa 594 labeling was imaged using 564-nm laser excitation and photon collection between 571 and 750 nm. Confocal scanning was performed using a resonance scanner at 8,000 Hz, and images were collected using line-scan averaging after 96 sweeps. Regions of interest were scanned using image stacks at 0.25- to 0.5-μm intervals sufficient to include the entire NMJ (typically 10–40 optical slices). Brightest projection images were made from these stacks, and photon collections from both wavelengths were superimposed in pseudocolor to generate composite images. The number of bassoon puncta (representing AZs) within each mouse NMJ was counted by hand within α-bungarotoxin-stained regions of the image. The number of bungarotoxin bands (representing AZs) within each frog NMJ was counted by hand within PNA stained regions of the image. For all AZ counting, each NMJ was counted by at least three individuals and their counts averaged. For purposes of display, some images were processed for deconvolution using the blind

deconvolution method within the Slidebook software (Intelligent Imaging Innovations, Ringsby, CT).

3.2.7 MCell simulations

For our computational investigation, we used MCell version 3.1 (www.mcell.org) to study action potential-triggered vesicle release at the frog and mouse NMJs. MCell is a particle-based, stochastic diffusion-reaction simulator which excels at modeling biological systems with complex 3D geometries (Kerr et al., 2008). Our MCell simulations comprised a spatially realistic model of an AZ region of the frog or mouse NMJ including VGCCs, Ca^{2+} buffer, and synaptic vesicles, with synaptotagmin and second sensor sites responsible for triggering vesicle release (Dittrich et al., 2013; Ma et al., 2015). During a MCell run of a single or train of APs, VGCCs open stochastically and admit Ca^{2+} ions into the terminal at a rate determined by the instantaneous driving force. Diffusing Ca^{2+} ions then bind to Ca^{2+} buffer molecules distributed throughout the terminal or to Ca^{2+} sensor sites on synaptic vesicles (synaptotagmin or second sensor sites). Individual synaptic vesicles were then determined to be "released" once they bound sufficient Ca^{2+} ions in accordance with our excess Ca^{2+} binding site and energy-based second sensor mechanism (Dittrich et al., 2013; Ma et al., 2015).

3.2.7.1 Frog NMJ model

In this study, we employed the same MCell model of the frog NMJ AZ as described in Dittrich et al. (2013) and Ma et al. (2015), including key geometric parameters. Briefly, the model consists of 26 synaptic vesicles of 50-nm diameter arranged in a double row (Fig. 3.1). Located between the double row of vesicles is a trough containing 26 VGCCs at a 1:1 channel to vesicle

stoichiometry (Luo et al., 2011) and at locations suggested by published estimates (Heuser et al., 1979; Pawson et al., 1998; Stanley et al., 2003). The bottom surface of each synaptic vesicle contains 8 synaptotagmin molecules, each with 5 Ca^{2+} binding sites, as well as 16 second Ca^{2+} sensor sites ("Y sites"). Vesicle fusion occurs according to the 16-Y-site energy model as previously described (Ma et al., 2015). VGCCs open stochastically with voltage-dependent channel kinetics and have a ~20% open probability (Luo et al., 2011) such that on average ~5 VGCCs open per action potential (AP) stimulation event within the AZ. The Ca^{2+} binding kinetics to sensor sites on synaptic vesicles, and to the 2 mM of static Ca^{2+} buffer located throughout the terminal, were identical to the values used previously (Ma et al., 2015).

3.2.7.2 Mouse NMJ model

Since we wanted to investigate the impact of AZ structure on NMJ function, our mouse NMJ AZ comprised the same molecular elements used in the frog model (synaptic vesicles with synaptotagmin and second sensor sites, VGCCs, Ca^{2+} buffers) with identical kinetic parameters. Thus we built the mouse NMJ model by rearranging the frog NMJ molecular elements into a mouse NMJ AZ organization based on published structural estimates for the mouse (Nagwaney et al., 2009; Fig. 3.1). It is estimated that each mouse NMJ AZ contains two docked synaptic vesicles and a double row of transmembrane particles, some of which are thought to be VGCCs, on either side of docked synaptic vesicles (Nagwaney et al., 2009). Our MCell model contains six AZs spaced ~500 nm apart on the presynaptic membrane to be consistent with previously reported AZ distributions (Chen et al., 2012; Fukunaga et al., 1983; Fukuoka et al., 1987; Ruiz et al., 2011). We included six AZs in the mouse model compared with the single AZ in the frog model since this enabled us to study possible Ca^{2+} mediated cross-talk between these small AZs, and also enhanced our sampling ability of release events during a single simulation run. Each mouse AZ in

our model contains four VGCCs, two each on either side of the two docked synaptic vesicles. The distance between the center of each channel and the bottom of its closely-associated vesicle is ~32 nm (Nagwaney et al., 2009). The details of each synaptic vesicle in the mouse model, including their number, arrangement, and the binding kinetics of synaptotagmin and second sensor sites, are identical to the frog NMJ model. Similarly, the opening kinetics of VGCCs, as well as the number and binding kinetics of Ca^{2+} buffer molecules, are identical to the frog model. Finally, vesicle release was determined according to the 16-Y-site energy model as described in Ma et al. (2015).

3.2.7.3 Runtime logistics

For our simulations, we used MCell version 3.1 with a custom-compressed binary reaction data output format to enable efficient storage and analysis of the large simulation output files. The simulation algorithms used in MCell have been described previously (Kerr et al., 2008). For each simulation condition, we typically conducted a large number of statistically independent runs (5,000–10,000) and used these to compute statistical averages and errors. Our simulations used a small time step of 10 ns to ensure that diffusing ions could properly sample the confined spaces in the AZs models, especially in the vicinity of synaptic vesicles. With our simulations, we are able to track Ca^{2+} ions entering the presynaptic space from individual VGCCs and could thus determine the origin of Ca^{2+} ions that contributed to the release of specific synaptic vesicles. The simulations were analyzed using custom scripts written in Go and Python. All simulations were conducted on the Axon cluster at the Pittsburgh Supercomputing Center (64 quad-core, 2.5-GHz Intel Xeon E5420 CPUs) and analyzed on several large-memory workstations at the Pittsburgh Supercomputing Center.

3.2.8 Statistical analysis

Statistical analysis was performed using either GraphPad Prism Version 5.0 (GraphPad Software, La Jolla, CA) or Origin 7 (OriginLab, Northampton, MA). Data are presented as means ± SE unless otherwise noted; $\alpha = 0.05$ for all statistical tests. For the MCell simulation outputs, data analysis was performed using Python and Go scripts.

3.3 Results

3.3.1 Average probability of release per active zone and synaptic vesicle

We started our exploration of AZ structure and function relationships by quantifying several key functional differences between the mouse and frog NMJ. In particular, we measured the average probability of vesicle release per AZ (Pr-AZ) and per synaptic vesicle within each AZ (Pr-SV), and the characteristics of short-term plasticity. To determine Pr-AZ and Pr-SV at the frog and mouse NMJ, we measured both the quantal content and the number of AZs at synapses in both preparations (Fig. 3.2).

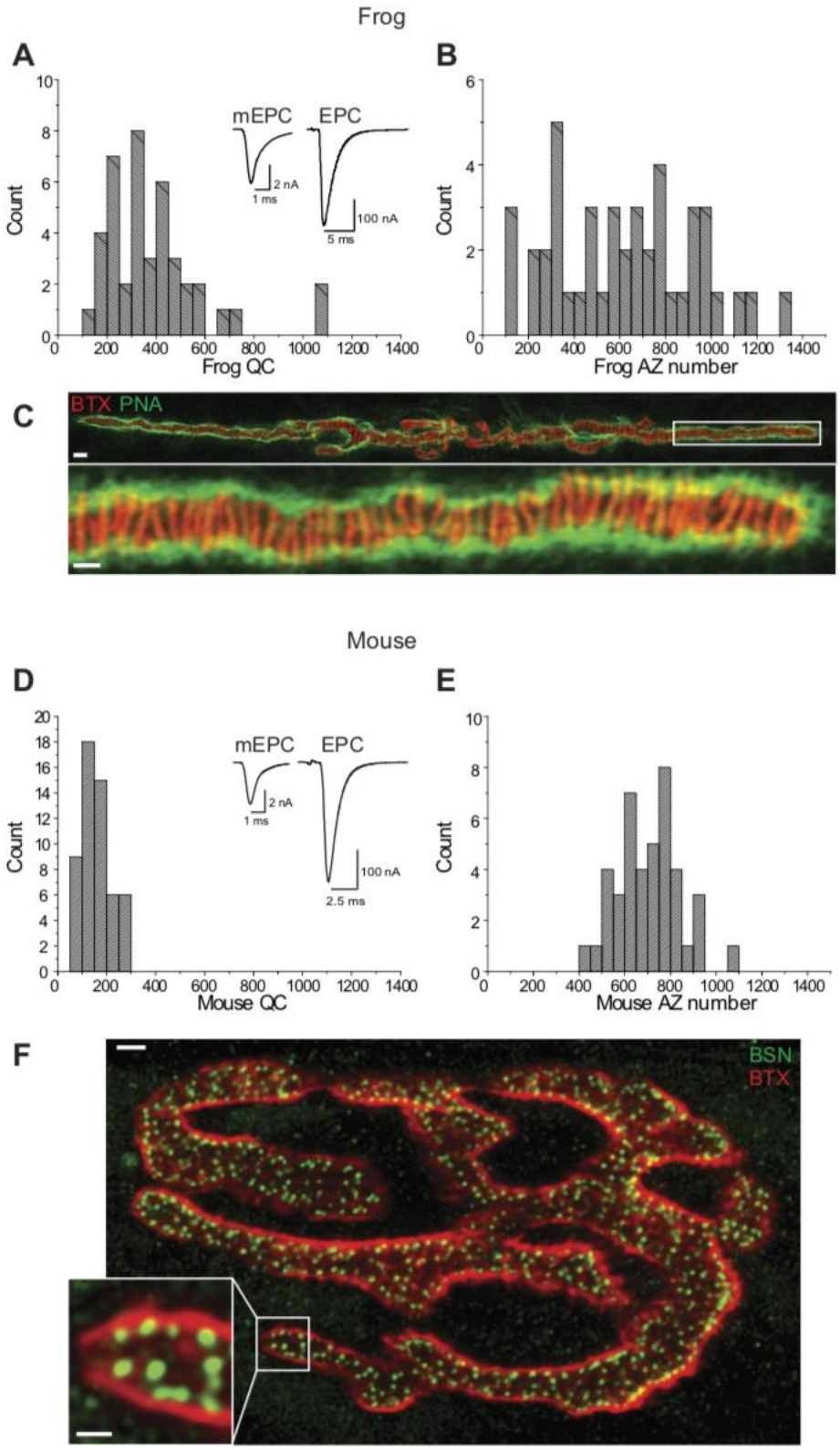
Frog
A
B
mEPC
EPC
2 nA
1 ms
100 nA
5 ms
Count
Frog QC
Frog AZ number
C
BTX PNA
Mouse
D
E
mEPC
EPC
2 nA
1 ms
100 nA
2.5 ms
Count
Mouse QC
Mouse AZ number
F
BSN
BTX

Figure 3.2 Quantal content and AZ number at frog and mouse NMJs.

A: Histogram plot of the distribution of quantal content (QC) measurements determined using two-electrode voltage clamp at frog NMJs. Inset shows sample mEPP (left; average of 300 events) and EPP (right; average of 15 events) recordings. B: Histogram plot of the distribution of AZ numbers measured across frog NMJs. C: Representative image of a frog NMJ stained with Alexa-488 peanut lectin (PNA, green) to outline synapses, and Alexa-594 α-bungarotoxin (BTX, red) to stain postsynaptic acetylcholine receptors and predict the location of AZs (red stripes). White box in the top image identifies the region that is enlarged in the bottom image. Scale bars = 5 μm (top) and 2 μm (bottom). D: Histogram plot of the distribution of quantal content measurements determined using two-electrode voltage clamp at mouse NMJs. Inset shows sample mEPP (left; average of 300 events) and EPP (right; average of 15 events) recordings. E: Histogram plot of the distribution of AZ numbers measured across mouse NMJs. F: Representative image of a mouse NMJ stained with Alexa-488 conjugated secondary antibody that recognized an anti-bassoon primary antibody to identify the location of AZs (BSN, green), and Alexa-594 α-bungarotoxin (BTX, red) to stain postsynaptic acetylcholine receptors and identify the extent of each NMJ. White box in the larger image identifies the region that is enlarged in the inset image. Scale bars = 5 μm (large image) and 2 μm (inset).

At the frog NMJ, average quantal content was 414.9 ± 40.4 (n = 43 synapses from 5 frogs; Fig. 3.2A). We determined an average AZ number per terminal of 616.4 ± 45.6 (n = 44 synapses from 10 frogs; Fig. 3.2, B and C). The large range in values (AZ number and quantal content) observed between synapses is likely due to the large range of postsynaptic muscle fiber diameters across this preparation as presynaptic nerve terminals scale in length (and AZ number) to compensate. Previous reports have shown that quantal content is linearly correlated with AZ number (Dorlöchter et al., 1993). Assuming functional homogeneity across AZs, we calculated an average Pr-AZ of 0.67 (the ratio of average quantal content to average AZ count). Since the number of vesicles that are docked at a frog NMJ averages 30 (Heuser et al., 1979; Pawson et al., 1998; Rizzoli and Betz, 2005), dividing the Pr-AZ by 30 synaptic vesicles yields an average Pr-SV of

0.022. Therefore, these data lead to the conclusion that the average Pr-SV is very low at the frog NMJ.

At the mouse NMJ, we measured a quantal content of 157.8 ± 7.9 (n = 54 synapses from 6 mice; Fig. 3.2D). We calculated an average number of AZs per terminal of 703.5 ± 22 (n = 42 synapses from 6 mice; Fig. 3.2, E and F). Assuming functional homogeneity across AZs, we could then calculate the average Pr-AZ to be 0.22 (the ratio of average quantal content to average number of AZs). Since the number of vesicles that are docked at a mouse NMJ AZ averages 2 (Nagwaney at al., 2009), the average Pr-SV at the mouse NMJ equals 0.11, and thus is five times higher than at the frog NMJ.

3.3.2 Short-term plasticity characteristics at the frog and mouse NMJ

Using both paired stimuli and short trains of stimuli at the frog NMJ we observed relatively strong facilitation across synapses. The paired pulse ratio (PPR) averaged 1.51 ± 0.015 (n = 325 synapses from 31 frogs) when measured with a 10-ms interstimulus interval and gradually declined as the interstimulus interval was lengthened, with a time constant of ~40 ms (Fig. 3.3A). At a 100-ms interstimulus interval there was little change in the second synaptic response as compared with the first (PPR = 1.06 ± 0.015 n = 47 synapses from 6 frogs; Fig. 3.3A). When the magnitude of transmitter release was measured during a short stimulus train from 10 to 100 Hz, facilitation was mild at 10 Hz (maximum 1.09 ± 0.03 at the 4th pulse in a train), and increased in magnitude to a maximum of 2.51 ± 0.16 at the 5th pulse in a 100-Hz train (n = 23 synapses from 3 frogs; Fig. 3.3, B and C). These observations are consistent with previous observations of strong facilitation at the frog NMJ when measured under physiological conditions (Meriney and Grinnell, 1991; Sosa and Zengel, 1993). As northern frogs are cold-blooded animals whose NMJs function in ambient

environmental temperatures, we also examined tetanic potentiation during 100-Hz trains at 10–12°C and found a similar facilitatory response (n = 31 synapses from 2 frogs; Fig. 3.3, B and C), indicating that facilitation at frog AZs is present at room temperature (20–22°C) and at colder temperatures (10–12°C).

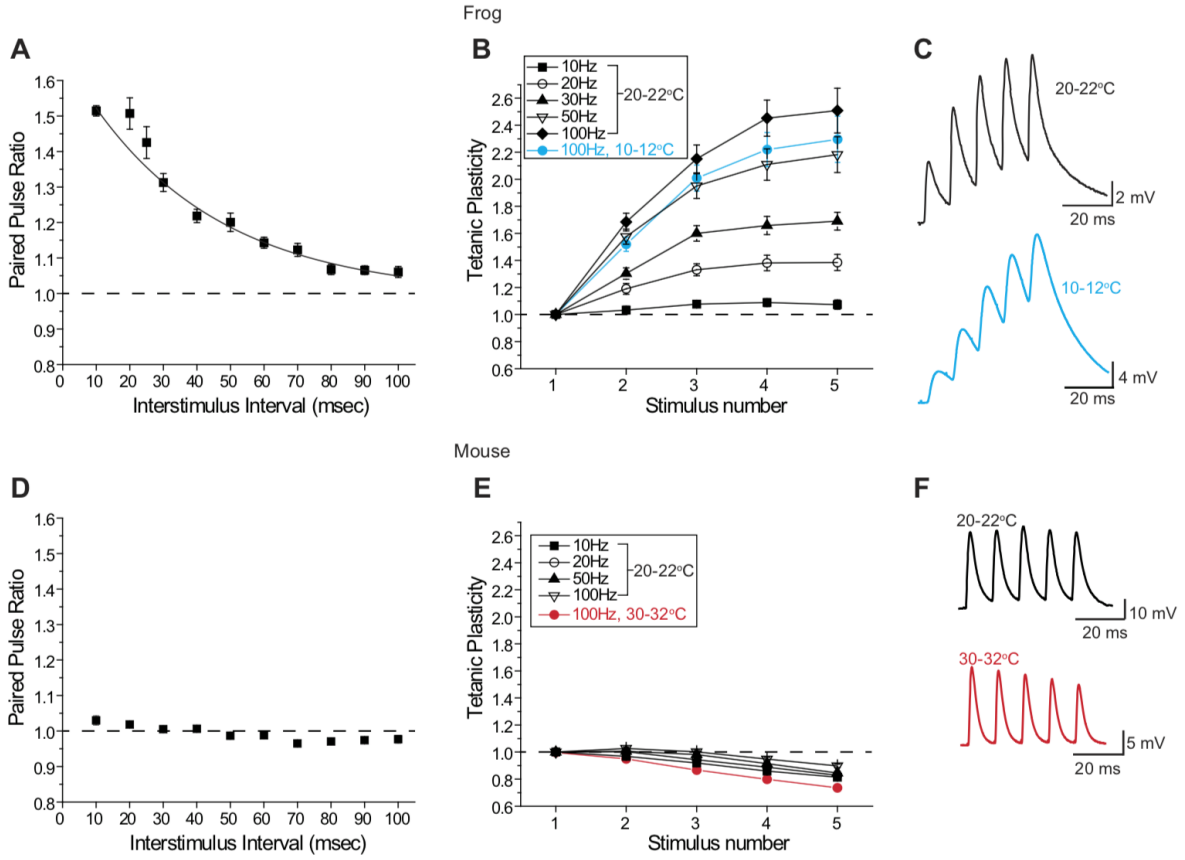

Figure 3.3 Short-term plasticity measured at frog (A-C) and mouse (D-F) NMJs.

A: Plot of the changes in paired-pulse ratio (EPP2/EPP1) at the frog NMJ when 2 stimuli were delivered at varying interstimulus intervals (10–100 ms). Paired-pulse facilitation is very sensitive to interstimulus interval at the frog NMJ. B: Plot of tetanic potentiation, normalized to the amplitude of the first EPP (EPPx/EPP1), when 5 stimuli were delivered to the frog motor nerve at varying frequencies (10–100 Hz). Data plotted in black were collected at room temperature (20–22°C); data plotted in blue were recorded at 10–12°C. The magnitude of tetanic potentiation is very sensitive to stimulus frequency at the frog NMJ. C: Sample EPPs recorded from a frog NMJ during a 100-Hz stimulus

train at 20–22°C (black) and 10–12°C (blue). D: Plot of the changes in paired-pulse ratio (EPP2/EPP1) at the mouse NMJ when 2 stimuli were delivered at varying interstimulus intervals (10–100 ms). Paired-pulse facilitation is minimal and relatively insensitive to interstimulus interval at the mouse NMJ. E: Plot of tetanic potentiation, normalized to the amplitude of the first EPP (EPPx/EPP1), when 5 stimuli were delivered to the mouse motor nerve at varying frequencies (10–100 Hz). Data plotted in black were collected at room temperature (20–22°C); data plotted in red were recorded at 30–32°C. At the mouse NMJ, mild tetanic potentiation gives way to mild depression at room temperature, and this form of short-term plasticity is relatively insensitive to stimulus frequency. Mild depression persists even at warmer temperatures (30–32°C). F: Sample EPPs recorded from a mouse neuromuscular junction during a 100-Hz stimulus train at 20–22°C (black) and 30–32°C (red).

Next, we sought to determine the short-term plasticity characteristics at the mouse NMJ using both paired-pulse and high-frequency train protocols with varying interstimulus intervals. Figure 3.3D shows a plot of the paired-pulse ratio (PPR) for each of the 10 interstimulus intervals tested. We observed little variability in PPR regardless of the interstimulus interval (maximum 1.03 ± 0.01 at a 10-ms interstimulus interval; n = 37 synapses from 5 mice; Fig. 3.3D). Similarly, there was little variability in short-term plasticity during trains of 5 stimuli at varying frequencies (Fig. 3.3E). Trains at 10, 20, 50, and 100 Hz were remarkably similar to one another, showing very little to no facilitation during the first few pulses (maximum 1.03 ± 0.01 at the second pulse in a 100-Hz train) and mild depression to 80–90% of the first EPP by the 5th stimulus in the train (n = 27 synapses from 3 mice). Therefore, unlike the frog NMJ, which shows strong frequency-dependent short-term facilitation (see above; Ma et al., 2015), the mouse NMJ consistently lacks significant facilitation, followed by mild depression, irrespective of stimulus frequency. These observations are consistent with previous reports at the mouse NMJ when short-term synaptic plasticity is studied in healthy synapses with physiological levels of extracellular Ca^{2+} (David and Barrett, 2003; Flink and Atchison, 2002), unlike the nonphysiological, low-extracellular-Ca^{2+}

conditions that are often used to strongly reduce the probability of release, inducing facilitation (e.g., Hirata et al., 1999; Nanou et al., 2016b; Urbano et al., 2003). Furthermore, because mice are warm-blooded animals whose NMJs function in a temperature-controlled environment, we also examined tetanic potentiation during 100-Hz stimulus trains at 30–32°C and found a similar mild depression (n = 29 synapses from 3 mice; Fig. 3.3, E and F). Therefore, mild depression during short stimulus trains at the mouse NMJ is not restricted to measurements at room temperature, and also occurs at warmer temperatures.

3.3.3 Using MCell to study AZ structure-function relationships

Since Pr-SV and the short-term synaptic plasticity described above are thought to emerge from characteristics within AZs, and the fine structure of frog and mouse AZs are well known, we wondered to what extent AZ organization alone could contribute to these physiological properties. To explore these structure-function relationships we used 3D diffusion-reaction simulations via MCell to examine the physiological impact of AZ geometry, in particular the number and position of presynaptic VGCCs relative to docked synaptic vesicles.

We had previously developed an MCell-based spatially realistic model of AZ function at the frog NMJ (Dittrich et al., 2013; Luo at al., 2015; Ma et al., 2015). Our simulations provided insight into many experimentally inaccessible aspects of synaptic function and the microscopic mechanisms underlying Ca^{2+}-triggered synaptic vesicle release. In particular, we were able to propose an excess Ca^{2+} binding site model of vesicle release (Dittrich et al., 2013), which integrated well-known synaptic physiology with recent biochemical and structural insights into the nature of the vesicle release machinery. In addition, we found that short-term synaptic facilitation

could be faithfully modeled by a second Ca^{2+} sensor protein with lower affinity and slower kinetics (Ma et al., 2015; similar to what has recently been reported in the CNS; Jackman et al., 2016).

The structure of our previous frog AZ model (Fig. 3.4, A and B) is based on extensive experimental data, and consists of two rows of 13 synaptic vesicles on each lateral edge of the AZ. Freeze-fracture and EM tomography provide evidence for the presence of ~200 transmembrane particles within each AZ arranged into two double rows between these vesicles (Harlow et al., 2001; Heuser and Reese, 1981; Pawson et al., 1998). We previously showed that only a small fraction of these transmembrane proteins are likely to be VGCCs and that each synaptic vesicle is on average associated with only a single VGCC (Luo et al., 2011; 2015). Therefore, in this study in which we sought to evaluate in isolation the impact of AZ organization on synaptic function, we did not change any of the inherent properties of the elements in the frog model (including VGCC biophysical properties, release sensor sensitivity, etc.) when making rearrangements that represented mouse AZ organization. By not changing the intrinsic properties of the AZ elements in our model, we could investigate, in isolation, the role that structure could play on function. The typical AZ at the mouse NMJ is structurally quite distinct (Nagwaney et al., 2009). Each mouse AZ is relatively short and consists of approximately two synaptic vesicles, with ~20–25 transmembrane particles arranged in two double rows on either side of the two vesicles (Nagwaney et al., 2009). Because we wanted to conserve the conclusions regarding VGCC distribution within AZs previously established in our frog NMJ studies (Dittrich et al., 2013; Luo et al., 2011; 2015), we assumed in our mouse MCell model that only a small fraction of AZ particles observed in EM studies would correspond to functional VGCCs. The organizational differences between frog and mouse NMJ AZs are highlighted in Figs. 3.1 and 3.4. Again, to maintain consistency between frog and mouse model properties, synaptic vesicles in each model contained 8 synaptotagmin molecules

(each with 5 Ca^{2+} ion binding sites), and 16 second Ca^{2+} sensor sites as described in our previously frog MCell model that most closely matched physiological properties of the frog NMJ (Ma et al., 2015; Fig. 3.4E).

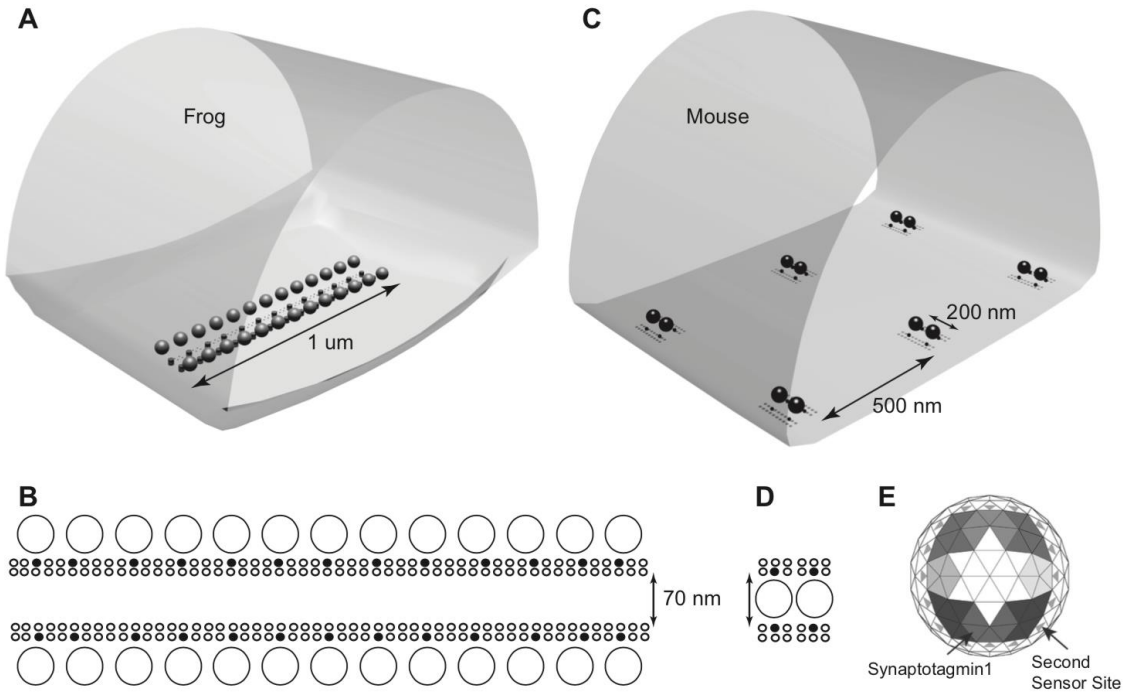

Figure 3.4 Diagrams of MCell models used for frog and mouse active zones.

A: Visualization output of the geometry used for the frog AZ MCell model. A single AZ is modeled along with the surrounding intraterminal space. The walls of this space are reflective to simulate the potential contribution from neighboring AZs. B: Organization of elements within the modeled frog AZ. A total of 26 docked synaptic vesicles (large circles) are positioned laterally and adjacent to two double rows of membrane proteins (small circles), some of which (filled circles) are VGCCs. C: Visualization output of the geometry used for the mouse AZ MCell model. A total of six AZs are modeled along with the surrounding intraterminal space. The walls of this space are reflective to simulate the potential contribution from neighboring AZs. D: Organization of elements within the modeled mouse AZ. A total of 2 docked synaptic vesicles (large circles) are positioned between two double rows of membrane proteins (small circles), some of which (filled circles) are VGCCs. E: The undersurface of each docked synaptic vesicle is populated with the Ca^{2+} binding sites of eight synaptotagmin 1 molecules (shaded large triangles; differences in

shading depict the 5 binding sites for each of the 8 synaptotagmin 1 molecules), and 16 second Ca^{2+} sensor sites (small gray triangles). The kinetic values for Ca^{2+} ion binding to these sites are reported in Ma et al., 2015.

Given that our MCell model of the frog NMJ AZ could accurately predict frog NMJ function (Dittrich et al., 2013; Luo et al., 2015; Ma et al., 2015), we hypothesized that our modeling approach could shed light on the impact of AZ structure on synaptic function. In particular, we wanted to investigate the degree to which the structural differences in the frog and mouse AZs, as described above and shown in Fig. 3.4, could explain their functional differences. We started our investigation by assembling an initial model of a mouse NMJ AZ based on the basic synaptic building blocks taken from the frog AZ. Specifically, we assembled a mouse AZ from two single vesicle release sites taken from our frog model, each consisting of a synaptic vesicle and two closely associated VGCCs, one on either side at positions constrained by the experimentally observed locations of transmembrane particles identified in electron microscopy images (Fig. 3.4, C and D). At the frog NMJ, freeze-fracture electron microscopic data leads to the conclusion that AZs have ~200 transmembrane particles (Pawson et al., 1998), ~30 of which are predicted to be functional VGCCs (Luo et al., 2011). In contrast, the mouse AZ has ~20–25 transmembrane particles (Nagwaney et al., 2009) and if the same fraction of these particles represents VGCCs, we would thus expect about four functional VGCCs, which we arranged bilaterally next to vesicles. The distance between the closest VGCC and synaptic vesicle was set at 32 nm, which agrees with experimental estimates for the distance of transmembrane particles (Nagwaney et al., 2009). Figure 3.4D shows a schematic view of our final mouse AZ model.

Apart from the structural rearrangement of single vesicle release sites from the frog into a mouse AZ configuration, we made no additional changes to any property of the model components. In particular, we left the properties of the key molecular machinery involved in

vesicle release unchanged, including the gating properties of the VGCCs (which are P/Q-type in the mouse vs. N-type in the frog), synaptotagmin Ca^{2+} sensors, facilitation sensors, Ca^{2+} buffer, and the vesicle release model. In summary, all properties of the elements within our mouse AZ model were identical to what has been reported previously for our frog model (Ma et al., 2015).

3.3.4 MCell simulations of mouse NMJ AZ model during single action potential stimuli

We then ran MCell simulations of single AP-triggered vesicle release within our mouse AZ model and found good qualitative agreement with all our experimental constraints. Our simulations resulted in a Pr-AZ of 0.13. Dividing this value by the two synaptic vesicles in each mouse AZ resulted in a Pr-SV = 0.065. In our mouse AZ model, the presence of two VGCCs close to each synaptic vesicle increased the release probability per vesicle (Pr-SV) following each action potential in our MCell model from 0.017 in the frog to 0.065 in the mouse, a roughly fourfold increase, which is a similar relationship to what we observed in our ex vivo recordings, where we calculated that the mouse AZ has a fivefold higher average Pr-SV than estimated in frog. This difference in Pr-SV between frog and mouse likely results from a difference in the number of VGCC per docked synaptic vesicle (twice as many in the mouse), coupled with the known nonlinear relationship between Ca^{2+} ion concentration and transmitter release magnitude (Dodge and Rahamimoff, 1967). The precise difference between our measured Pr-AZ in *ex vivo* recordings (Pr-AZ = 0.22) and our MCell model of mouse AZ organization that was created as a simple rearrangement of the elements in the frog MCell model (Pr-AZ = 0.13) may reflect specific differences in the properties or numbers of some of the AZ elements between frog and mouse NMJs. However, for the purposes of this study that focused on the defined impact of a simple

rearrangement of AZ organization on synaptic function, those specific differences are beyond the scope of this report.

In addition, our mouse AZ model also predicted two key known properties of this synapse. Figure 3.5A shows the simulated distribution of transmitter release events following an AP, which is in good agreement with previously published experimental data regarding the distribution of synaptic latencies (Wang et al., 2010) and synaptic delay (Bukharaeva et al., 2007; Katz and Miledi, 1965). Last, the known steep dependence of transmitter release on the external Ca^{2+} concentration (Ca^{2+} release relationship, CRR) is also predicted by this mouse model (Fig. 3.5B). Our simulated value for CRR was 3.8, which is in good agreement with previously published experimental data (Smith, 1988). Thus, under a single action potential stimulus paradigm, a simple rearrangement of frog AZ elements into a mouse AZ structure closely recapitulates the experimentally observed probability of vesicle release, CRR, and distribution of release events at the mouse NMJ.

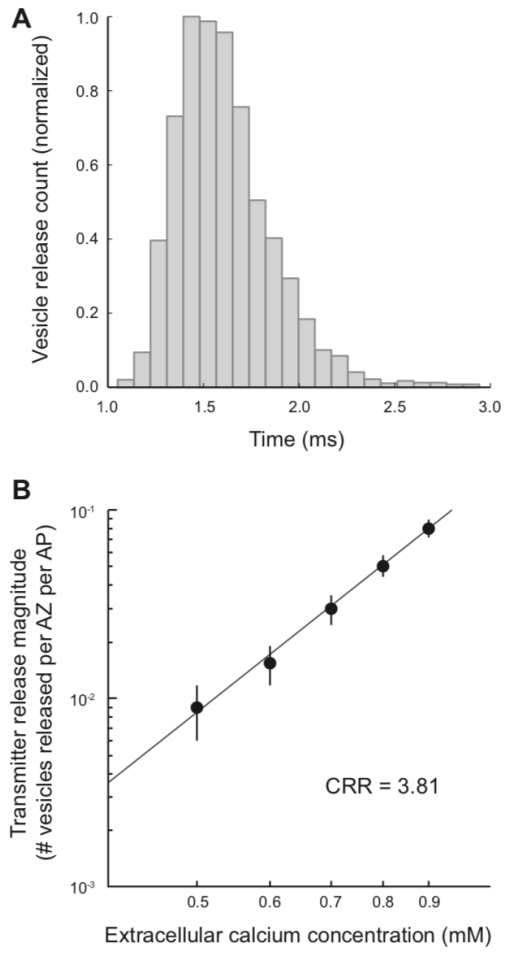

Figure 3.5 Distribution of transmitter release latencies and the Ca^{2+}-release relationship (CRR) predicted by the mouse MCell model.

A: Histogram plot of the time course of single vesicle release events in the mouse MCell model following a presynaptic action potential closely matching previously published physiology data (Wang et al., 2010). B: Plot of the changes in the magnitude of transmitter release (number of vesicles released per AZ per AP) as the extracellular Ca^{2+} concentration was varied in the mouse MCell model. When plotted on a log scale, these data are fit by line with a slope of 3.81, closely matching the known 4th-order relationship between extracellular Ca^{2+} and transmitter release.

3.3.5 Mouse AZ model exhibits no short-term facilitation

Since our mouse AZ model provided good agreement with experimental observations following a single action potential stimulus, we next wondered if we could also model the dramatic difference in short-term plasticity observed experimentally when comparing frog and mouse NMJs. Indeed, when simulating paired-pulse plasticity at different interstimulus intervals, our MCell-based frog and mouse models recapitulated the striking experimental difference between these two synapses (Fig. 3.6, A and B). Furthermore, when using high-frequency trains of stimuli (5 pulses at 100 Hz), our MCell simulations closely predicted the strong potentiation at the frog NMJ in contrast to mild depression at the mouse NMJ (Fig. 3.6C). Thus, a simple reorganization of single vesicle release sites from a frog AZ configuration into a mouse AZ configuration resulted in significantly different short-term plasticity properties that matched what we observed experimentally.

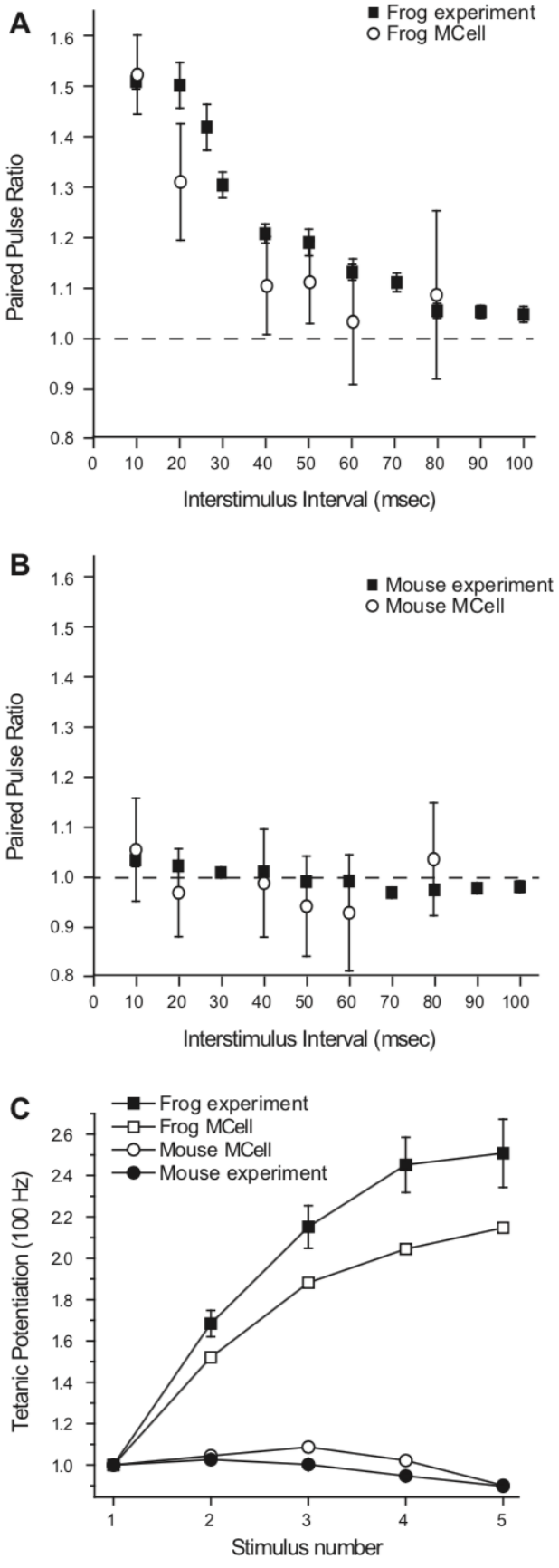
A
Frog experiment
Frog MCell
Paired Pulse Ratio
Interstimulus Interval (msec)
B
Mouse experiment
Mouse MCell
Paired Pulse Ratio
Interstimulus Interval (msec)
C
Frog experiment
Frog MCell
Mouse MCell
Mouse experiment
Tetanic Potentiation (100 Hz)
Stimulus number

Figure 3.6 Differences in short-term plasticity observed between frog and mouse NMJs are reproduced by a simple rearrangement in the organization of elements in the frog MCell model into the organization observed in the mouse AZ.

A and B: Plot of changes in the paired-pulse ratio at the frog (A) and mouse (B) NMJ when the interstimulus interval is changed. The experimental data collected (filled squares) are closely matched by the MCell simulation data (open circles) in both cases. C: Plot of tetanic potentiation at 100 Hz in the frog (filled squares) and mouse (filled circles) is closely matched by MCell simulation of the frog AZ (open squares) and the mouse AZ (open circles) models.

These data raise the question of the sub-AZ mechanisms responsible for this dramatic change in synaptic function. Using MCell, we tracked each Ca^{2+} ion within our simulations and determined when and where they bound during vesicle fusion events. During a short train of APs at 100 Hz within the frog model, we plotted the number of vesicle fusion events that were triggered completely by de novo Ca^{2+} ion binding (binding that occurred only during the particular stimulus in which the vesicle fused) compared with vesicle fusion events that were triggered in part by Ca^{2+} ions that remained bound from a previous stimulus event, so-called residual bound Ca^{2+}. These later events thus represented the fusion of synaptic vesicles that had partially bound Ca^{2+} from a previous stimulus event (Fig. 3.7). This persistent Ca^{2+} binding occurred via binding of Ca^{2+} ions to second-sensor sites on vesicles which had a slower off rate than our synaptotagmin 1 sites (see Ma et al., 2015) and were thus more likely to remain bound during a subsequent stimulation event. At the frog AZ, a large amount of persistent Ca^{2+} binding to vesicles played an important role in the observed short-term plasticity (Fig. 3.7A). In contrast, in our mouse AZ model, the relatively small amount of persistent bound Ca^{2+} resulted in little to no facilitation, and slight depression later in the pulse sequence (Fig. 3.7B).

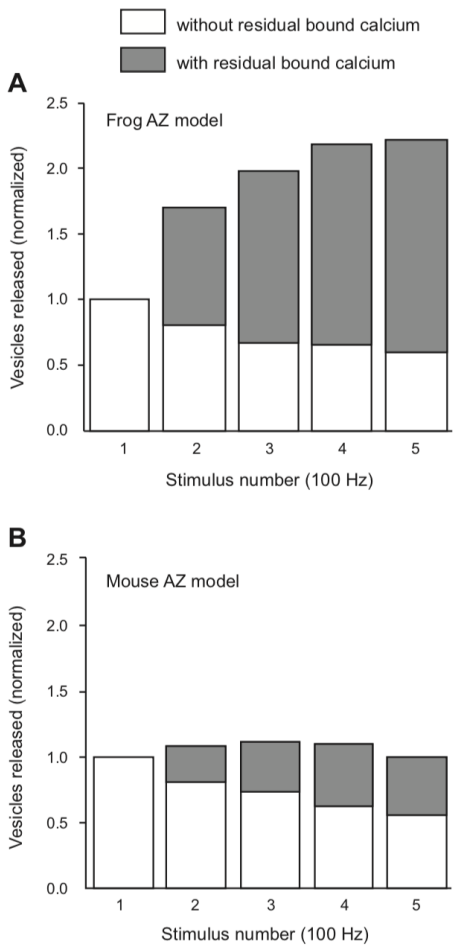

Figure 3.7 Differenecs between frog and mouse MCell AZ models in the fraction of vesicle fusion events that included residual bound Ca^{2+} ions.

A: In the frog AZ model, the vesicles that fuse during a train of action potentials at 100 Hz have a strongly increasing fraction of Ca^{2+} ions that remain bound from a prior action potential stimulus. B: In the mouse AZ model, there are fewer vesicle fusion events that are partially triggered by residual bound Ca^{2+} ions than observed in the frog model (A).

In assessing the underlying reason for these differences between frog and mouse AZs, we made several additional observations. We determined the number of VGCCs that opened during each action potential in the frog and mouse models. Even though both models employed the same

VGCC gating scheme, and thus each channel in these AZs opened with a probability of ~0.2, the large difference in the total number of VGCCs in frog and mouse AZs led to a corresponding difference in the number of Ca^{2+} channels that opened with each action potential (Fig. 3.8). Importantly, whereas frog AZs almost always experienced multiple VGCC openings per action potential (mean ± SD = 4.8 ± 1.0) with only rare failures (Fig. 3.8A), at the mouse AZ, more than 40% of action potential stimuli failed to open any VGCC in a single AZ, and most of the time only a single VGCC opened in each AZ (Fig. 3.8B). Because the frog AZ experienced multiple VGCC openings per stimulation event, and contained tens of vesicles, this resulted in significant persistent Ca^{2+} bound vesicles, whereas vesicle fusion remained relatively rare (Pr-AZ = 0.67; Luo et al., 2015). In effect, during a stimulation event, each synaptic vesicle in the frog AZ bound Ca^{2+} ions from several VGCCs at varying distances from its location. In contrast, the few VGCC openings in the mouse AZ per stimulation event, combined with only two docked vesicles, resulted in little docked vesicle persistent Ca^{2+} binding. Furthermore, in the mouse we found very little diffusion of Ca^{2+} ions between neighboring AZs separated by 500 nm from each other. Thus, individual AZs in the mouse NMJ acted essentially as isolated units. The above data provide an explanation of why there was significantly more release of persistently Ca^{2+} bound synaptic vesicles in frog AZs resulting in strong facilitation compared with mouse AZs (Fig. 3.7).

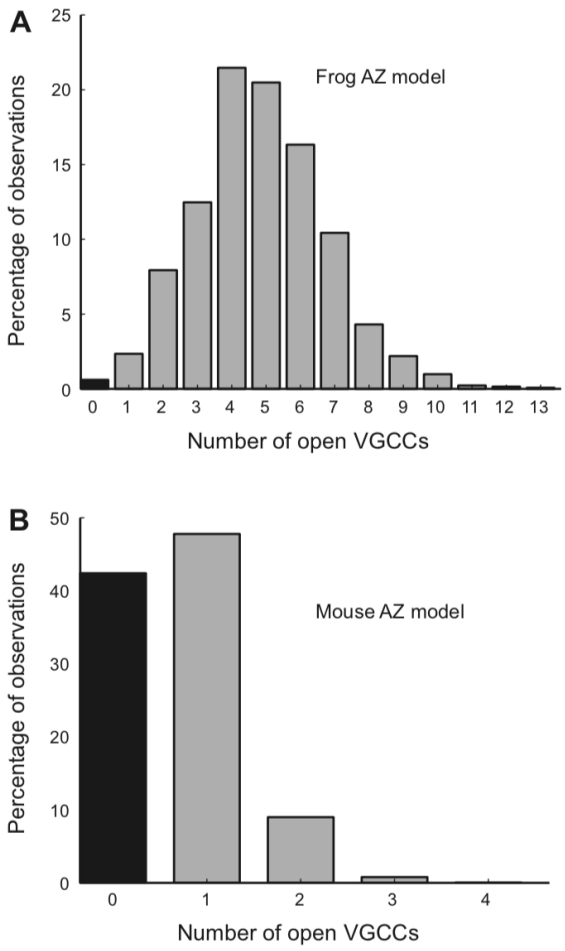

Figure 3.8 The number of VGCCs that open in frog and mouse AZ MCell models.

Although both frog and mouse AZ models have VGCCs with a Po during an action potential of ~0.2, since the frog AZ has 26 VGCCs, the average number of VGCCs that open during an action potential in the frog AZ model (A) is much greater than in the mouse AZ model (B). Within one AZ in the mouse model, more than 40% of action potentials do not open any VGCCs (black bar; B), and most action potentials open only one VGCC. Within the frog AZ model, most action potential stimuli open 3–7 VGCCs, and failures (black bar; A) are rare.

To further explore the impact of the mouse AZ organization on short-term synaptic plasticity, we tested the role of AZ spacing. To examine this issue, we varied the distance between each of the small AZs in the mouse model from 500 nm in our control model to a 250-, 200-, 150-

, and 100-nm spacing (Fig. 3.9). We found that as the mouse AZs were positioned closer to one another, tetanic stimulation resulted in little change, with only mild facilitation (less than 20%) observed at 250-, 200-, and 150-nm AZ spacing, and mild depression that was similar to control (500-nm AZ spacing) when AZs were only 100 nm apart from one another (Fig. 3.9, A and B). We next examined the proportion of release events derived from docked vesicles that either had residual bound Ca^{2+} from prior action potentials in the train, or did not have any residual bound Ca^{2+} (Fig. 3.9C). We found that as AZ spacing was decreased in the mouse model, there was an increase in release of residual bound vesicles, but there was also a decrease in release of vesicles that did not have any residual bound Ca^{2+} These data lead to the conclusion that close AZ spacing in the mouse model nerve terminal resulted in both an increase in vesicle depletion (depression), and vesicles with residual bound Ca^{2+} (facilitation). Therefore, closely positioning mouse AZs together does not create the strong facilitation observed in the frog AZ.

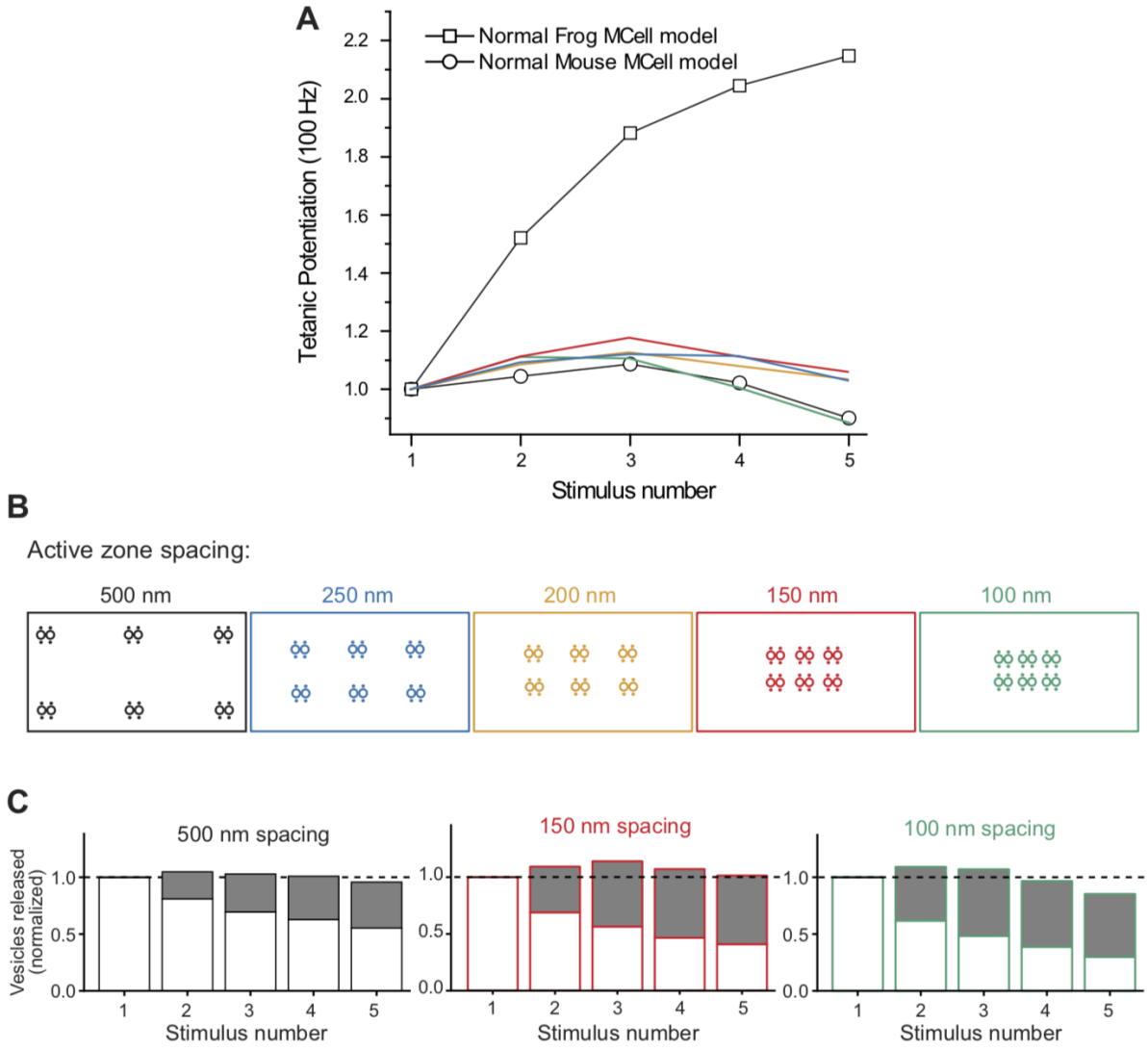

Figure 3.9 The impact on tetanic potentiation of moving modeled mouse AZs closer together.

A: Plot of tetanic potentiation during a 100-Hz action potential train. Open squares and circles recapitulate the control MCell model data for frog and mouse AZs (see Fig. 3.6C). Plots in blue, yellow, red, and green represent short-term plasticity for the model in which the 6 modeled AZs are 250, 200, 150, and 100 nm apart from one another as color coded in the diagrams in B. C: Plots of the fraction of vesicle fusion events that included residual bound Ca^{2+} ions (as described in Fig. 3.7) for 3 AZ spacing arrangements that resulted in the extremes in short-term synaptic plasticity at the modeled mouse AZ (500, 150, and 100 nm AZ spacing, and color coded as in A and B).

The difference in short-term plasticity observed when AZs were organized in a frog or mouse arrangement might also be due to the number of VGCC-docked synaptic vesicle complexes (single vesicle release sites) present in the linear array, and the stoichiometry between VGCCs and docked synaptic vesicles. To explore these issues, we either varied the length of the frog AZ by removing VGCC-vesicle complexes, or varied the number of VGCCs available near the long linear array of docked synaptic vesicles by removing only VGCCs from the AZ (Fig. 3.10, A and B). Both manipulations resulted in less facilitation during a 100-Hz train. However, even shortening the frog AZ to only 2 vesicles (the same as in a mouse AZ) resulted in more facilitation than was observed in the mouse NMJ (Fig. 3.10B). The difference between this shortened frog AZ (with only 2 vesicles) and the control mouse AZ (that also contains 2 vesicles) is that there are fewer VGCCs per docked synaptic vesicle in the frog AZ (only 1) compared with the mouse (where there are 2 VGCCs per docked vesicle). The importance of the stoichiometric relationship between VGCCs and docked synaptic vesicles was also evident when only VGCCs were removed from the frog AZ (Fig. 3.10A). Under these conditions, two VGCCs surrounded by excess docked synaptic vesicles resulted in more facilitation during a 100-Hz stimulus train than when both VGCCs and docked synaptic vesicles were reduced to only two (compare light blue data plotted in Fig. 3.10, A and B).

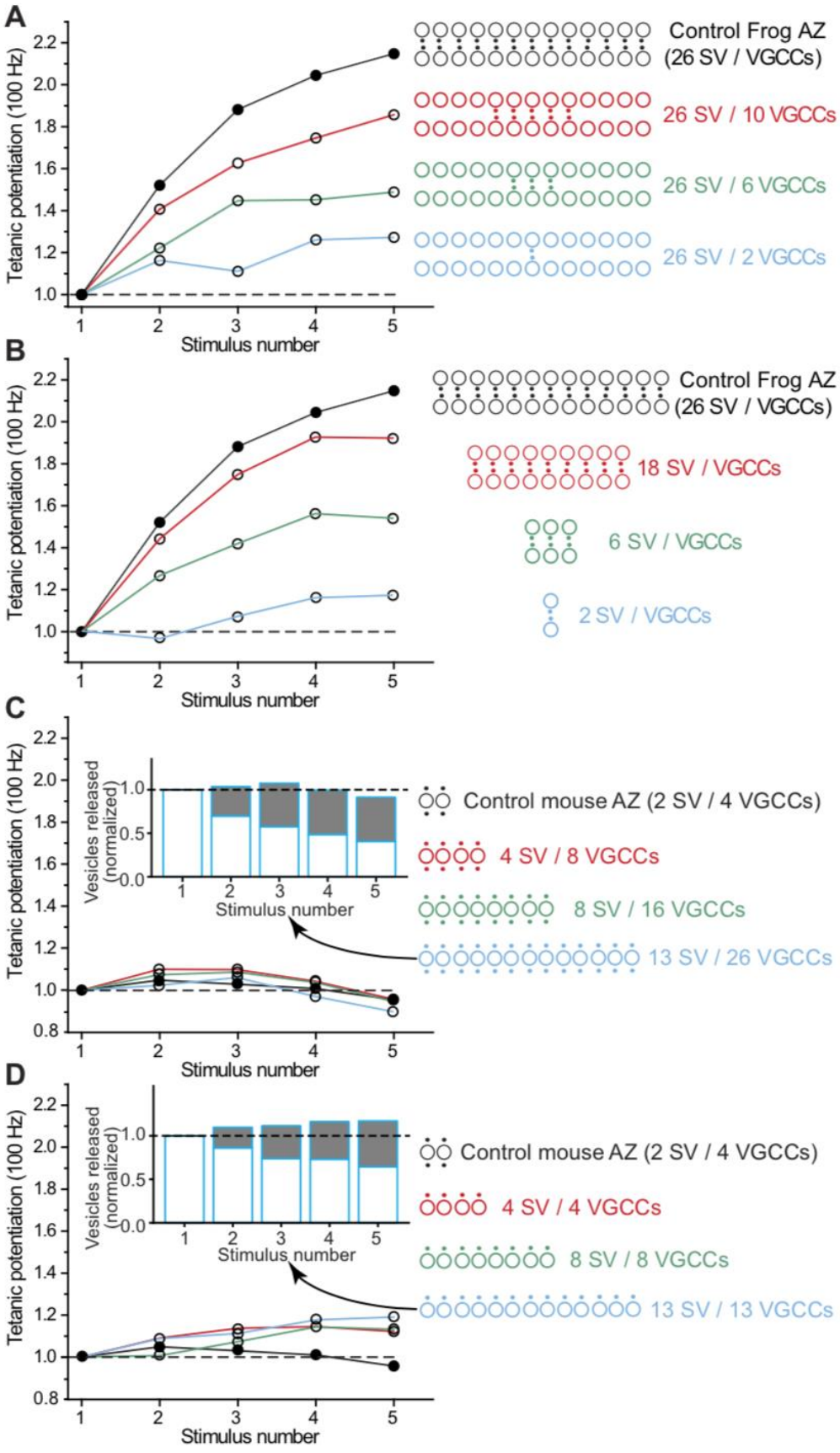
A
Tetanic potentiation (100 Hz)
Stimulus number
Control Frog AZ
(26 SV / VGCCs)
26 SV / 10 VGCCs
26 SV / 6 VGCCs
26 SV / 2 VGCCs
B
Tetanic potentiation (100 Hz)
Stimulus number
Control Frog AZ
(26 SV / VGCCs)
18 SV / VGCCs
6 SV / VGCCs
2 SV / VGCCs
C
Tetanic potentiation (100 Hz)
Vesicles released (normalized)
Stimulus number
Control mouse AZ (2 SV / 4 VGCCs)
4 SV / 8 VGCCs
8 SV / 16 VGCCs
13 SV / 26 VGCCs
D
Tetanic potentiation (100 Hz)
Vesicles released (normalized)
Stimulus number
Control mouse AZ (2 SV / 4 VGCCs)
4 SV / 4 VGCCs
8 SV / 8 VGCCs
13 SV / 13 VGCCs

Figure 3.10 The impact on tetanic potentiation of altering the length of modeled frog and mouse AZs.

A: The control frog model (filled circles) generates strong tetanic potentiation during a 100-Hz stimulus train, but this potentiation significantly weakens as the number of VGCCs is reduced (open circles). The diagrams at the right depict the organization of VGCCs (black dots) relative to synaptic vesicles (large open circles) as VGCCs are removed (plots and diagrams are color coded for clarity). B: The control frog model (filled circles) generates strong tetanic potentiation during a 100-Hz stimulus train, but this potentiation significantly weakens as the number of both VGCCs and docked synaptic vesicles are reduced. The diagrams at the right depict the organization of VGCCs (black dots) and synaptic vesicles (large open circles) as both are removed (plots and diagrams are color coded for clarity). C: The control mouse model (filled circles) generates mild tetanic depression during a 100-Hz stimulus train, and this mild depression does not change significantly as the mouse AZ arrangement is lengthened (adding two VGCCs for each additional docked synaptic vesicle). The diagrams at the right depict the organization of VGCCs (black dots) and docked synaptic vesicles (large open circles) as both are added (plots and diagrams are color coded for clarity). Inset: plot of the fraction of vesicle fusion events that included residual bound Ca^{2+} ions for the longest AZ plotted in blue. D: The control mouse model (filled circles) generates mild tetanic depression during a 100-Hz stimulus train, but this mild depression reverses to mild tetanic potentiation when the mouse AZ arrangement is changed and lengthened by only adding one VGCC for each docked synaptic vesicle. The diagrams at the right depict the organization of VGCCs (black dots) and docked synaptic vesicles (large open circles) as both are added (plots and diagrams are color coded for clarity). Inset: plot of the fraction of vesicle fusion events that included residual bound Ca^{2+} ions for the longest AZ plotted in blue.

We also took the approach of lengthening the control mouse AZ to examine effects on tetanic potentiation during a 100-Hz train of action potentials (Fig. 3.10, C and D). Interestingly, we found that lengthening the mouse AZ did not increase tetanic potentiation during a 100-Hz action potential train (Fig. 3.10C), and this was reminiscent of the effects when AZ spacing was reduced (Fig. 3.9). We speculated that this might be due to the presence of twice as many VGCCs per synaptic vesicle (increasing the probability of release) compared with the VGCC-synaptic vesicle arrangement in the frog AZ. To reduce the number of VGCCs in this lengthened mouse

AZ, we removed half of the VGCCs such that there was only one VGCC per docked synaptic vesicle (Fig. 3.10D). This arrangement resulted in an increase in tetanic potentiation as this AZ arrangement was lengthened; however, the tetanic potentiation measured did not reach the level observed in the control frog AZ. Therefore, the organization of VGCCs and docked synaptic vesicles in a frog AZ appears to be optimized for strong tetanic potentiation. These experiments demonstrate that the structural organization of AZs, in particular the number and arrangement of VGCCs with respect to docked synaptic vesicles, can have a major impact on AZ function.

3.4 Discussion

In the current study, we have explored the functional significance for the differential assembly of single vesicle release sites and demonstrate that the arrangement of these presynaptic elements can regulate specific aspects of synaptic function. Taking advantage of the well-known differences in function and structural organization between the highly ordered AZs at frog and mouse neuromuscular synapses, we demonstrated that the arrangement of presynaptic VGCCs and docked synaptic vesicles within neuromuscular AZs significantly determines the probability of transmitter release and short-term synaptic plasticity at these synapses. Here, we have looked at AZ organization alone, with no changes to the functional properties of any of the AZ elements. For example, we did not alter the gating properties of the Ca^{2+} channels in frog (N-type channels) and mouse MCell models (P/Q-type channels), even though it is possible that they are different (future studies can examine the impact of these specific differences). The approach of keeping the properties of AZ elements unchanged was purposeful so that we could examine in isolation the impact of AZ organization. Because we could predict the differences between frog and mouse

physiology with this approach, our results add to the growing evidence that presynaptic AZ structure has a major impact on synaptic function. In particular, we show that differential assembly of single vesicle release sites can in fact be used to tune key synaptic properties like short-term facilitation. This raises the interesting prospect that such a mechanism could be used to tune synaptic transmission by adding or removing single vesicle release sites or by changing the intrinsic spatial relationship between VGCCs and synaptic vesicles.

The critical dependence of short-term synaptic plasticity on AZ organization has not previously been appreciated, and frog and mouse neuromuscular synapses provide an opportunity to explore these relationships carefully. Our study highlights the importance of single vesicle release site organization on the spatiotemporal profile of presynaptic Ca^{2+} ions during action potential activity, a critical determinant of short-term synaptic plasticity. Furthermore, we show that a high docked synaptic vesicle-to-VGCC ratio appears to favor facilitation during short tetanic trains of stimulation (see Fig. 3.10). In this report, we have exclusively focused on these AZ structure-function relationships and have not explored the other mechanisms that have been shown to shape short-term synaptic plasticity. It is clear from a variety of reports that short-term synaptic plasticity can also be regulated by changes in action potential shape that alters the probability of release (reviewed in von Gersdorff and Borst, 2002), neuronal Ca^{2+}-sensor proteins (Nanou et al., 2016a; 2016b; Sippy et al., 2003), the expression of various synaptotagmin types (Jackman et al., 2016; Tejero et al., 2016), intraterminal Ca^{2+} buffer concentration and distribution (Blatow et al., 2003; Jackson and Redman, 2003; Matveev et al., 2004), the phosphorylation state of AZ proteins (Srinivasan et al., 2008), and a variety of metaplasticity and neuromodulatory events (Becker et al., 2013; Goussakov et al., 2000; Li et al., 1998; Lozovaya et al., 2011). Here, we do not intend to suggest that these factors are less important than AZ organization, but rather study in isolation

the impact of the number and position of presynaptic Ca^{2+} channels and docked synaptic vesicles, and the resultant differences in the spatiotemporal profile of presynaptic Ca^{2+} during action potential activity, with the knowledge that short-term synaptic plasticity can be further affected by the other mechanisms listed above.

In considering the species-specific benefits of arranging VGCCs and docked synaptic vesicles within AZs at the NMJ in different organizational structures, it is useful to consider the environmental conditions of both frogs and mice. In all species, the function of the NMJ is to release sufficient transmitter to reliably bring the postsynaptic muscle cell to threshold for triggering an action potential and eliciting a muscle twitch. The "safety factor" at neuromuscular synapses (releasing more transmitter than is required to bring the postsynaptic muscle cell to threshold) ensures that most synapses reliably trigger an action potential in the postsynaptic muscle cell (Wood and Slater, 2001). When comparing frogs and mice in the context of the data presented in this report, one issue that might be relevant is the range of temperatures within which the NMJ needs to function reliably. The mouse is a warm-blooded animal, and as such, the mouse NMJ does not experience variation in temperature. Under these conditions, a relatively stable amount of transmitter release during a brief burst of action potential activity maintains release above the safety factor for eliciting a postsynaptic action potential. In contrast, the cold-blooded frog NMJ is required to maintain effective function over a wide range of environmental temperatures. The magnitude of transmitter released from the frog NMJ has been reported to be sensitive to temperature, especially at very cold temperatures where transmitter release decreases (Adams, 1989; Barrett et al., 1978). In fact, at the frog sartorius NMJ there are very few NMJs that do not release enough transmitter to bring the postsynaptic muscle to threshold at room temperature (only ~6%), but this number increases to 42% at 5°C and 59% at 2.5°C (Adams, 1989). Therefore, at

cold temperatures, tetanic potentiation of transmitter release during short trains of activity might be required at the frog NMJ to recover reliable communication between nerve and muscle. It is possible that the frog AZ has evolved an organizational structure that creates strong facilitation during short trains of action potential activity that serves to aid in bringing the postsynaptic membrane to threshold even at colder temperatures when quantal content is low.

Finally, in this report, we have restricted our modeling of the mouse NMJ AZ to the simple rearrangement of elements from our frog NMJ AZ model, with no modifications to the properties of elements. We used this approach to make the point that organization of AZ elements was the primary determinant of function, but we recognize that the mouse AZ might have additional refinements that are likely required to more closely match finer details of synaptic function, and to recapitulate all aspects of mouse NMJ function (particularly after pharmacological or disease manipulation). These refinements remain as the subject of future investigations.

3.4.1 Author contributions

R.L., J.M., T.B.T., A.E.H., L.K., M.S.T., B.S.V., H.P.R., S.D.M., and M.D. performed experiments; R.L., J.M., T.B.T., A.E.H., L.K., M.S.T., B.S.V., H.P.R., S.D.M., and M.D. analyzed data; R.L., A.E.H., and S.D.M. prepared figures; R.L., T.B.T., A.E.H., S.D.M., and M.D. edited and revised manuscript; R.L., J.M., T.B.T., A.E.H., L.K., M.S.T., B.S.V., H.P.R., S.D.M., and M.D. approved final version of manuscript; T.B.T., A.E.H., S.D.M., and M.D. conceived and designed research; T.B.T., A.E.H., S.D.M., and M.D. interpreted results of experiments; S.D.M. drafted manuscript.

4.0 Conclusions[4]

4.1 Summary

We provide evidence that structure can inform function at the vertebrate neuromuscular presynapse and that the organization and stoichiometry of VGCCs relative to synaptic vesicle release sensors is a critical determinant of the magnitude and dynamics of neurotransmitter release. Importantly, we demonstrate that heterogeneity in neurotransmitter release can be produced by heterogeneity in the density and distribution of VGCCs, and that these variable arrangements lead to differences in the spatio-temporal calcium profile at the time of vesicle fusion. Interestingly, we observe species-related differences in presynaptic structure that could correlate to the different environmental demands on each species, suggesting that each species may tune intracellular calcium to precisely regulate neurotransmitter release. While these conclusions have been raised previously across a number of different preparations (Zhai and Bellen, 2004), we demonstrate here with unparalleled resolution that an appreciation of the micro-environment of the presynaptic release site, specifically the behavior of calcium ions (the trigger for neurotransmitter release) at the time of vesicle fusion, is paramount for understanding presynaptic physiology.

---

[4] An excerpt of this chapter was published as: Laghaei R, Ma, J, Tarr TB, Homan AE, Kelly L, Tilvawala MS, Vuocolo BS, Rajasekaran HP, Meirney SD, Dittrich M. Transmitter release site organization can predict synaptic function at the neuromuscular junction. *J Neurophysiol* 119, 2018. Reproduced with permission from the American Physiological Society.

4.2 Structure determines function at the NMJ

The transmitter release site at synapses displays a remarkable diversity in structural forms (Zhai and Bellen, 2004). Over the last decade, a number of common themes relating synaptic structure to function have emerged.

The first theme relates to how the number of AZs within individual synapses correlates with their strength. Small mammalian CNS synapses often contain a single or a small number of AZs (Clarke et al., 2012), each of which is organized into a disk-shaped array that is often characterized by a "particle web" (Dresbach et al., 2001; Phillips et al., 2001). Functionally, these small synapses are often also characterized by a low probability of transmitter release (Goda and Südhof, 1997; Tarr et al., 2013b). On the other hand, large synapses like the NMJ or the calyx of Held in the auditory brain stem contain hundreds of AZs, which result in highly reliable transmitter release and synaptic strength (Dondzillo et al., 2010; Sätzler et al., 2002; Tarr et al., 2013b; Taschenberger et al., 2002). Studies of frog NMJs have shown that AZ size and number are better indicators of transmitter release magnitude than total synapse size (Herrera et al., 1985; Propst and Ko, 1987). Thus, synaptic strength appears to be positively correlated with an increase in the number and size of AZs within terminals.

A second theme in synaptic structure and function pertains to the internal organization of individual AZs. Recent freeze-fracture immunoelectron microscopy has revealed that presynaptic VGCCs within AZs at both small CNS boutons and at large calyx of Held synapses are arranged into small clusters (Althof et al., 2015; Nakamura et al., 2015). In addition to this conservation of AZ nanoarchitecture across synapse types, there appears to be heterogeneity in the size of individual AZs at large synapses like the calyx of Held. This, in turn, results in significant variability in the number of VGCCs within each AZ and corresponding variations in vesicular

release probability (Nakamura et al., 2015; Sheng et al., 2012) and short-term synaptic plasticity (Sheng et al., 2012). Therefore, variations in sub-AZ organization within the calyx of Held appear to significantly impact their functional output. Similar structure-function relationships have been described across small CNS boutons where VGCC number appears to scale with AZ area and significantly influences transmitter release probability (Holderith et al., 2012). Furthermore, it was recently shown that the coupling of VGCCs and docked synaptic vesicles tightens during the development of small cortical synapses, and that these changes correlate with predicted alterations in probability of transmitter release and short-term synaptic plasticity (Baur et al., 2015). Overall, it appears that heterogeneity in the organization within AZs, especially with respect to the number and spatial localization of VGCCs and docked synaptic vesicles, can be a strong determinant of synaptic function.

Recent studies have used a combination of electrophysiology, imaging, and computer modeling to suggest that AZs of synapses may be constructed by differential assembly of unitary building blocks, so-called single vesicle release sites (Tarr et al., 2013b) akin to the "secretosome" described by Bennett (1996). These single vesicle release sites consist of a synaptic vesicle and a small number of associated VGCCs (Luo et al., 2015; Tarr et al., 2013b), and their arrangement into AZs directly affects synaptic release and facilitation. It is possible that AZs are arranged in different organizational structures that might be fine-tuned to construct individual synapses with properties that are appropriate for each synapse physiologically.

4.3 Limitations and future directions

There has been considerable effort to identify the players involved neurotransmitter release and ascribe defined roles to each of these various proteins. While important discoveries have provided context for some of these proteins, there has been less appreciation for the nature to which the organization, density, and arrangement of these proteins relative to calcium sources and release sensors may influence their function as well as neurotransmitter release as a whole. A recent study suggested there may be a dynamic interaction of proteins at the AZ, such that these proteins exist in a functional network and make transient interactions according to the needs of the release site or synapse (Calloway et al., 2015).

While we have focused primarily on studying the arrangement of VGCCs relative to release sensors, there are other ion channels in the presynaptic AZ that are also important for shaping neurotransmitter release. Calcium-activated potassium channels have been shown to be localized to the presynaptic release site and gate in response to a cooperative action of calcium ions from VGCCs and depolarization. Further, these calcium-activated potassium channels may exist in functional complexes (Berkefeld et al., 2006) with VGCCs, providing a powerful mechanism for controlling presynaptic excitability and neurotransmitter release. We have begun studies to investigate the contribution of these calcium-activated potassium channels to neurotransmitter release at the frog and mouse neuromuscular junction (Ginebaugh et al., 2018) and will use these investigations to refine our computational AZ models and begin to parse out how other channels in the AZ can shape the spatio-temporal calcium profile and subsequent release.

While we have made the case for structure influencing function, we have necessarily ignored possible molecular heterogeneity within the AZ. In fact, various isoforms of proteins such as synaptotagmin (Jackman and Regehr, 2017) have been ascribed to functional heterogeneity in

release and plasticity, raising the notion that differences in function may also be due to differences in the composition of release sites. While we do not deny that these factors are certainly at play, the necessity to study structure in isolation has led to our simplified model. In the future, we hope to include more players in our investigations to gain a fuller sense of how structure may influence function.

Furthermore, we have assumed functional homogeneity across the hundreds of AZs at a single NMJ synapse. However, growing evidence from the Drosophila and mouse NMJs suggests that AZs are likely functionally heterogeneous and may be specially tuned for different modes of release (Gaffield et al., 2009a; 2009b; Melom et al., 2013; Peled et al., 2014; Tabares et al., 2007; Wyatt and Balice-Gordon, 2008). Thus, future studies investigating how AZ structure may influence vesicle release and plasticity on a single-AZ level will provide further insight into how the structure of presynaptic AZs may be heterogeneous across single synapses, and how this contributes to the function of the synapse as a whole.

Bibliography

Adams BA. Temperature and synaptic efficacy in frog skeletal muscle. J Physiol 408: 443–455, 1989.

Adler EM., Augustine GF, Duffy SN, Charlton MP. Alien intracellular calcium chelators attenuate neurotransmitter release at the squid synapse. J Neurosci 11: 1496– 1507, 1991.

Allana TN, Lin JW. Relative distribution of Ca^{2+} channels at the crayfish inhibitory neuromuscular junction. J Neurophysiol 92: 1491– 1500, 2004.

Althof D, Baehrens D, Watanabe M, Suzuki N, Fakler B, Kulik Á. Inhibitory and excitatory axon terminals share a common nano-architecture of their Cav2.1 (P/Q-type) Ca^{2+} channels. Front Cell Neurosci 9: 315, 2015.

Araque A, Clarac F, Buño W. P-type Ca^{2+} channels mediate excitatory and inhibitory synaptic transmitter release in crayfish muscle. PNAS 91: 4224– 4228, 1994.

Atwood HL, Karunanithis S. Diversification of synaptic strength: Presynaptic elements. Nat Rev 3: 497– 516, 2002.

Barrett EF, Barrett JN, Botz D, Chang DB, Mahaffey D. Temperature-sensitive aspects of evoked and spontaneous transmitter release at the frog neuromuscular junction. J Physiol 279: 253–273, 1978.

Baur D, Bornschein G, Althof D, Watanabe M, Kulik A, Eilers J, Schmidt H. Developmental tightening of cerebellar cortical synaptic influx-release coupling. J Neurosci 35: 1858–1871, 2015.

Becker B, Klein EM, Striepens N, Mihov Y, Schlaepfer TE, Reul J, Goossens L, Schruers K, Kendrick KM, Hurlemann R. Nicotinic acetylcholine receptors contribute to learning-induced metaplasticity in the hippocampus. J Cogn Neurosci 25: 986–997, 2013.

Bennett MR. Neuromuscular transmission at an active zone: the secretosome hypothesis. J Neurocytol 25: 869–891, 1996.

Bennett MR, Farnell L, Gibson WG. The probability of quantal secretion near a single calcium channel of an active zone. Biophys J 78: 2201–2221, 2000a.

Bennett MR, Farnell L, Gibson WG. The probability of quantal secretion within an array of calcium channels of an active zone. Biophys J 78: 2222–2240, 2000b.

Bennett MR, Farnell L, Gibson WG. The facilitated probability of quantal secretion within an array of calcium channels of an active zone at the amphibian neuromuscular junction. Biophys J 86: 2674–2690, 2004.

Bennett MR, Gibson WG, Robinson J. Probabilistic secretion of quanta and the synaptosecretosome hypothesis: evoked release at active zones of varicosities, boutons, and endplates. Biophys J 73: 1815–1829, 1997.

Berkefeld H, Sailer CA, Bildl W, Rohde V, Thumfart JO, Eble S, Klugbauer N, Reisinger E, Bischofberger J, Oliver D, Knaus HG, Schulte U, Fakler B. BKCa-Cav channel complexes mediate rapid localized Ca^{2+}-activated K+ signaling. Science 314: 615-620, 2006.

Birks R, Huxley HE, Katz B. The fine structure of the neuromuscular junction of the frog. J Physiol 150: 134–144, 1960.

Blatow M, Caputi A, Burnashev N, Monyer H, Rozov A. Ca^{2+} buffer saturation underlies paired pulse facilitation in calbindin-D28k-containing terminals. Neuron 38: 79–88, 2003.

Blundon JA, Wright SN, Brodwick MS, Bittner GD. Residual free calcium is not responsible for facilitation of neurotransmitter release. PNAS 90: 9388– 9392, 1993.

Borst JG, Sakmann B. Calcium influx and transmitter release in a fast CNS synapse. Nature 383: 431–434, 1996.

Bradacs H, Cooper R, Msghina M, Atwood H. Differential physiology and morphology of phasic and tonic motor axons in a crayfish limb extensor muscle. J Exp Biol 200: 677– 691, 1997

Bukharaeva EA, Samigullin D, Nikolsky EE, Magazanik LG. Modulation of the kinetics of evoked quantal release at mouse neuromuscular junctions by calcium and strontium. J Neurochem 100: 939–949, 2007.

Calloway N, Gouzer G, Xue M, Ryan TA. The active-zone protein Munc13 controls the use-dependence of presynaptic voltage-gated calcium channels. Elife 4, 2015.

Chen J, Billings SE, Nishimune H. Calcium channels link the muscle-derived synapse organizer laminin β2 to Bassoon and CAST/Erc2 to organize presynaptic active zones. J Neurosci 31: 512–525, 2011.

Chen J, Mizushige T, Nishimune H. Active zone density is conserved during synaptic growth but impaired in aged mice. J Comp Neurol 520: 434–452, 2012.

Clarke GL, Chen J, Nishimune H. Presynaptic active zone density during development and synaptic plasticity. Front Mol Neurosci 5: 12, 2012.

Cohen MW, Jones OT, Angelides KJ. Distribution of Ca^{2+} channels on frog motor nerve terminals revealed by fluorescent omega-conotoxin. J Neurosci 11: 1032–1039, 1991.

Cooper AS, Cooper RL. Historical view and physiology demonstration at the NMJ of the crayfish opener muscle. Journal of Visualized Experiments: JoVE 3: 1595, 2009.

Cooper RL, Harrington CC, Marin L, Atwood HL. Quantal release at visualized terminals of a crayfish motor axon: Intraterminal and regional differences. J Comp Neurol 375: 583– 600, 1996.

Cooper RL, Marin, L, Atwood HL. Synaptic differentiation of a single motor neuron: Conjoint definition of transmitter release, presynaptic calcium signals, and ultrastructure. J Neurosci 15: 4209– 4222, 1995.

Cooper RL, Stewart BA, Wojtowicz JM, Wang S, Atwood HL. Quantal measurement and analysis methods compared for crayfish and Drosophila neuromuscular junctions, and rat hippocampus. J Neurosci Methods 61: 67– 78, 1995.

Cooper RL, Winslow JL, Govind CK, Atwood HL. Synaptic structural complexity as a factor enhancing probability of calcium-mediated transmitter release. J Neurophysiol 75: 2451–2466, 1996.

Couteaux R, Pécot-Dechavassine M. Specialized areas of presynaptic membranes. C R Acad Sci Hebd Seances Acad Sci D 278: 291– 293, 1974.

David G, Barrett EF. Mitochondrial Ca^{2+} uptake prevents desynchronization of quantal release and minimizes depletion during repetitive stimulation of mouse motor nerve terminals. J Physiol 548: 425–438, 2003.

Dittrich M, Pattillo JM, King JD, Cho S, Stiles JR, Meriney SD. An excess-calcium-binding-site model predicts neurotransmitter release at the neuromuscular junction. Biophys J 104: 2751–2763, 2013.

Dodge FA Jr, Rahamimoff R. Co-operative action a calcium ions in transmitter release at the neuromuscular junction. J Physiol 193: 419–432, 1967.

Dondzillo A, Sätzler K, Horstmann H, Altrock WD, Gundelfinger ED, Kuner T. Targeted three-dimensional immunohistochemistry reveals localization of presynaptic proteins Bassoon and Piccolo in the rat calyx of Held before and after the onset of hearing. J Comp Neurol 518: 1008–1029, 2010.

Dorlöchter M, Meurer S, Wernig A. Acetylcholine receptor bars and transmitter release in frog neuromuscular junctions. Neuroscience 52: 987–999, 1993.

Douthitt HL, Luo F, McCann SD, Meriney SD. Dynasore, an inhibitor of dynamin, increases the probability of transmitter release. Neuroscience 172: 187–195, 2011.

Dresbach T, Qualmann B, Kessels MM, Garner CC, Gundelfinger ED. The presynaptic cytomatrix of brain synapses. Cell Mol Life Sci 58: 94–116, 2001.

Eggermann E, Bucurenciu I, Goswami SP, Jonas P. Nanodomain coupling between Ca^{2+} channels and sensors of exocytosis at fast mammalian synapses. Nat Rev Neurosci 13: 7–21, 2012.

Ellisman MH, Rash JE, Staehelin LA, Porter KR. Studies of excitable membranes. II. A comparison of specializations at neuromuscular junctions and nonjunctional sarcolemmas of mammalian fast and slow twitch muscle fibers. J Cell Biol 68: 752– 774, 1976.

Fedchyshyn MJ, Wang LY. Developmental transformation of the release modality at the calyx of Held synapse. J Neurosci 25: 4131–4140, 2005.

Flink MT, Atchison WD. Passive transfer of Lambert-Eaton syndrome to mice induces dihydropyridine sensitivity of neuromuscular transmission. J Physiol 543: 567–576, 2002.

Fogelson AL, Zucker RS. Presynaptic calcium diffusion from various arrays of single channels. Implications for transmitter release and synaptic facilitation. Biophys J 48: 1003–1017, 1985.

Fukunaga H, Engel AG, Lang B, Newsom-Davis J, Vincent A. Passive transfer of Lambert-Eaton myasthenic syndrome with IgG from man to mouse depletes the presynaptic membrane active zones. PNAS 80: 7636–7640, 1983.

Fukoka T, Engel AG, Lang B, Newsom-Davis J, Prior C, Wray DW. Lambert-eaton myasthenic syndrome: I. Early morphological effects of IgG on the presynaptic membrane active zones. Ann Neurol 22, 193– 199, 1987.

Fukuoka T, Engel AG, Lang B, Newsom-Davis J, Vincent A. Lambert-Eaton myasthenic syndrome: II. Immunoelectron microscopy localization of IgG at the mouse motor end-plate. Ann Neurol 22: 200–211, 1987.

Gaffield MA, Tabares L, Betz WJ. The spatial pattern of exocytosis and post-exocytic mobility of synaptopHluorin in mouse motor nerve terminals. J Physiol 587: 1187–1200, 2009a.

Gaffield MA, Tabares L, Betz WJ. Preferred sites of exocytosis and endocytosis colocalize during high- but not lower-frequency stimulation in mouse motor nerve terminals. J Neurosci 29: 15308–15316, 2009b.

Garcia JW, Bartol TM, Spencer DJ, Sejnowski TJ. An improved event-driven model of presynaptic dynamics for large-scale simulations. Program No. 503.16. 2016 Neuroscience Meeting Planner. San Diego, CA: Society for Neuroscience.

Ginebaugh SP, Ojala K, Homan AE, Miller E, Meriney SD. Characterisitics of the action potential waveform at mammalian and amphibian neuromuscular junctions. Program No 203.17. 2018 Neuroscience Meeting Planner. San Diego, CA: Society for Neuroscience.

Goda Y, Südhof TC. Calcium regulation of neurotransmitter release: reliably unreliable? Curr Opin Cell Biol 9: 513–518, 1997.

Goussakov IV, Fink K, Elger CE, Beck H. Metaplasticity of mossy fiber synaptic transmission involves altered release probability. J Neurosci 20: 3434–3441, 2000.

Govind CK, Atwood HL, Pearce J. Inhibitory axoaxonal and neuromuscular synapses in the crayfish opener muscle: Membrane definition and ultrastructure. J Comp Neurol 351: 476–488, 1995.

Govind CK, Pearce J. Active zones and receptor surfaces of freeze-fractured crayfish phasic and tonic motor synapses. J Neurocytol 32: 39– 51, 2003.

Govind CK, Pearce J, Wojtowicz JM, Atwood HL. "Strong" and "weak" synaptic differentiation in the crayfish opener muscle: Structural correlates. Synapse 16: 45– 58, 1994.

Grinnell AD, Herrera AA. Physiological regulation of synaptic effectiveness at frog neuromuscular junctions. J Physiol 307: 301–317, 1980.

Hadley D, Murphy T, Valladares O, Hannenhalli S, Ungar L, Kim J, Bućan M. Patterns of sequence conservation in presynaptic neural genes. Genome Biol 7: R105, 2006.

Han Y, Kaeser PS, Südhof TC, Schneggenburger R. RIM determines Ca^{2+} channel density and vesicle docking at the presynaptic active zone. Neuron 69: 304–316, 2011.

Harlow ML, Ress D, Stoschek A, Marshall RM, McMahan UJ. The architecture of active zone material at the frog's neuromuscular junction. Nature 409: 479–484, 2001.

Heidelberger R, Heinemann C, Neher E, Matthews G. Calcium dependence of the rate of exocytosis in a synaptic terminal. Nature 371: 513–515, 1994.

Herrera AA, Grinnell AD, Wolowske B. Ultrastructural correlates of naturally occurring differences in transmitter release efficacy in frog motor nerve terminals. J Neurocytol 14: 193–202, 1985.

Heuser JE, Reese TS. Morphology of synaptic vesicle discharge and reformation at the frog neuromuscular junction. In: Synaptic Transmission and Neuronal Interaction, edited by Bennett MVL, editor. New York: Raven, 1974, vol. 28, chapt. 4, p. 59–78. Soc. Gen. Physiol. Series

Heuser JE, Reese TS, Dennis MJ, Jan Y, Jan L, Evans L. Synaptic vesicle exocytosis captured by quick freezing and correlated with quantal transmitter release. J Cell Biol 81: 275–300, 1979.

Heuser JE, Reese TS. Structural changes after transmitter release at the frog neuromuscular junction. J Cell Biol 88: 564–580, 1981.

Hirata K, Nakagawa M, Urbano FJ, Rosato-Siri MD, Moreira JE, Uchitel OD, Sugimori M, Llinás R. Reduced facilitation and vesicular uptake in crustacean and mammalian neuromuscular junction by T-588, a neuroprotective compound. Proc Natl Acad Sci USA 96: 14588–14593, 1999.

Holderith N, Lorincz A, Katona G, Rózsa B, Kulik A, Watanabe M, Nusser Z. Release probability of hippocampal glutamatergic terminals scales with the size of the active zone. Nat Neurosci 15: 988–997, 2012.

Homan AE, Laghaei R, Dittrich M, Meriney SD. Impact of spatiotemporal calcium dynamics within presynaptic active zones on synaptic delay at the frog neuromuscular junction. J Neurophysiol 119: 688– 699, 2018.

Hong SJ, Chang CC. Use of geographutoxin II (mu-conotoxin) for the study of neuromuscular transmission in mouse. Br J Pharmacol 97: 934–940, 1989.

Jackman SL, Turecek J, Belinsky JE, Regehr WG. The calcium sensor synaptotagmin 7 is required for synaptic facilitation. Nature 529: 88–91, 2016.

Jackman SL, Regehr WG. The mechanisms and functions of synaptic facilitation. Neuron 94: 447–464, 2017.

Jackson MB, Redman SJ. Calcium dynamics, buffering, and buffer saturation in the boutons of dentate granule-cell axons in the hilus. J Neurosci 23: 1612–1621, 2003.

Jahromi SS. Atwood HL. Three-dimensional ultrastructure of the crayfish neuromuscular apparatus. J Cell Biol 63: 599– 613, 1974.

Jones RA, Harrison C, Eaton SL, Llavero Hurtado M, Graham LC, Alkhammash L, Oladiran OA, Gale A, Lamont DJ, Simpson H, Simmen MW, Soeller C, Wishart TM, Gillingwater TH. Cellular and molecular anatomy of the human neuromuscular junction. Cell Rep 21: 2348–2356, 2017.

Jung JH, Szule JA, Marshall RM, McMahan UJ. Variable priming of a docked synaptic vesicle. Proc Natl Acad Sci USA 113: E1098–E1107, 2016.

Kamiya H, Zucker RS. Residual Ca^{2+} and short-term synaptic plasticity. Nature 371: 603– 606, 1994.

Katz B, Kuffler SW. Excitation of the nerve-muscle system in Crustacea. Proc R Soc Lond B Biol Sci 133: 374– 389, 1946.

Katz B, Miledi R. The measurement of synaptic delay, and the time course of acetylcholine release at the neuromuscular junction. Proc R Soc Lond B Biol Sci 161: 483–495, 1965.

Katz B, Miledi R. Spontaneous and evoked activity of motor nerve endings in calcium Ringer. J Physiol 203: 689–706, 1969.

Kennedy KM, Piper ST, Atwood HL. Synaptic vesicle recruitment for release explored by Monte Carlo simulation at the crayfish neuromuscular junction. Can J Physiol Pharm 77: 634–650, 1999.

Kerr RA, Bartol TM, Kaminsky B, Dittrich M, Chang JC, Baden SB, Sejnowski TJ, Stiles JR. Fast Monte Carlo simulation methods for biological reaction-diffusion systems in solution and on surfaces. SIAM J Sci Comput 30: 3126–3149, 2008.

King MJ, Atwood HL. Govind CK. Structural features of crayfish phasic and tonic neuromuscular terminals. J Comp Neurol 372: 618– 626, 1996.

Laghaei R, Ma J, Tarr TB, Homan AE, Kelly L, Tilvawala MS, Vuocolo BS, Rajasekaran HP, Meriney SD, Dittrich M. Transmitter release site organization can predict synaptic function at the neuromuscular junction. J Neurophysiol 119: 1340– 1355, 2018.

Li H, Weiss SR, Chuang DM, Post RM, Rogawski MA. Bidirectional synaptic plasticity in the rat basolateral amygdala: characterization of an activity-dependent switch sensitive to the presynaptic metabotropic glutamate receptor antagonist 2S-alpha-ethylglutamic acid. J Neurosci 18: 1662–1670, 1998.

Lozovaya N, Mukhtarov M, Tsintsadze T, Ledent C, Burnashev N, Bregestovski P. Frequency-dependent cannabinoid receptor-independent modulation of glycine receptors by endocannabinoid 2-AG. Front Mol Neurosci 4: 13, 2011.

Luo F, Dittrich M, Cho S, Stiles JR, Meriney SD. Transmitter release is evoked with low probability predominately by calcium flux through single channel openings at the frog neuromuscular junction. J Neurophysiol 113: 2480–2489, 2015.

Luo F, Dittrich M, Stiles JR, Meriney SD. Single-pixel optical fluctuation analysis of calcium channel function in active zones of motor nerve terminals. J Neurosci 31: 11268–11281, 2011.

Ma J, Kelly L, Ingram J, Price TJ, Meriney SD, Dittrich M. New insights into short-term synaptic facilitation at the frog neuromuscular junction. J Neurophysiol 113: 71–87, 2015.

Matveev V, Bertram R, Sherman A. Calcium cooperativity of exocytosis as a measure of Ca^{2+} channel domain overlap. Brain Res 1398: 126–138, 2011.

Matveev V, Zucker RS, Sherman A. Facilitation through buffer saturation: constraints on endogenous buffering properties. Biophys J 86: 2691–2709, 2004.

Matveev V, Bertram R, Sherman A. Residual bound Ca^{2+} can account for the effects of Ca^{2+} buffers on synaptic facilitation. J Neurophysiol 96: 3389– 3397, 2006.

McLachlan EM, Martin AR. Non-linear summation of end-plate potentials in the frog and mouse. J Physiol 311: 307–324, 1981.

Melom JE, Akbergenova Y, Gavornik JP, Littleton JT. Spontaneous and evoked release are independently regulated at individual active zones. J Neurosci 33: 17253–17263, 2013.

Meriney SD, Grinnell AD. Endogenous adenosine modulates stimulation-induced depression at the frog neuromuscular junction. J Physiol 443: 441–455, 1991.

Millar AG, Atwood HL. Crustacean phasic and tonic motor neurons. Integr Comp Biol 44: 4–13, 2004.

Msghina M, Govind CK, Atwood HL. Synaptic structure and transmitter release in crustacean phasic and tonic motor neurons. J Neurosci 18: 1374– 1382, 1998.

Msghina M, Millar AG, Charlton MP, Govind CK, Atwood HL. Calcium entry related to active zones and differences in transmitter release at phasic and tonic synapses. J Neurosci 19: 8419– 8434, 1999.

Mukhamedyarov MA, Grishin SN, Zefirov AL, Palotás A. The mechanisms of multi-component paired-pulse facilitation of neurotransmitter release at the frog neuromuscular junction. Pflügers Archiv 458: 563– 570, 2009.

Nagwaney S, Harlow ML, Jung JH, Szule JA, Ress D, Xu J, Marshall RM, McMahan UJ. Macromolecular connections of active zone material to docked synaptic vesicles and presynaptic membrane at neuromuscular junctions of mouse. J Comp Neurol 513: 457–468, 2009.

Nakamura Y, Harada H, Kamasawa N, Matsui K, Rothman JS, Shigemoto R, Silver RA, DiGregorio DA, Takahashi T. Nanoscale distribution of presynaptic Ca^{2+} channels and its impact on vesicular release during development. Neuron 85: 145–158, 2015.

Nanou E, Sullivan JM, Scheuer T, Catterall WA. Calcium sensor regulation of the CaV2.1 Ca^{2+} channel contributes to short-term synaptic plasticity in hippocampal neurons. Proc Natl Acad Sci USA 113: 1062–1067, 2016a.

Nanou E, Yan J, Whitehead NP, Kim MJ, Froehner SC, Scheuer T, Catterall WA. Altered short-term synaptic plasticity and reduced muscle strength in mice with impaired regulation of presynaptic CaV2.1 Ca^{2+} channels. Proc Natl Acad Sci USA 113: 1068–1073, 2016b.

Nishimune H. Active zones of mammalian neuromuscular junctions: formation, density, and aging. Ann N Y Acad Sci 1274: 24–32, 2012.

Nishimune H, Sanes JR, Carlson SS. A synaptic laminin-calcium channel interaction organizes active zones in motor nerve terminals. Nature 432: 580–587, 2004.

Nishimune,H, Badawi Y, Mori S, Shigemoto K. Dual-color STED microscopy reveals a sandwich structure of Bassoon and Piccolo in active zones of adult and aged mice. Sci Rep 6: 27935, 2016.

Pan B, Zucker RS. A general model of synaptic transmission and short-term plasticity. Neuron 62: 539– 554, 2009.

Parnas I, Parnas H, Dudel J. Neurotransmitter release and its facilitation in crayfish muscle. Pflügers Archiv 395: 261– 270, 1982.

Pawson PA, Grinnell AD. Post-tetanic potentiation in strong and weak neuromuscular junctions: physiological differences caused by a differential Ca^{2+}-influx. Brain Res 323: 311–315, 1984.

Pawson PA, Grinnell AD. Seasonal changes in the normal variability in release properties of motor nerve terminals in Rana pipiens. Brain Res 495: 182–188, 1989.

Pawson PA, Grinnell AD. Physiological differences between strong and weak frog neuromuscular junctions: A study involving tetanic and post-tetanic potentiation. J Neurosci 10: 1769–1778, 1990.

Pawson PA, Grinnell AD, Wolowske B. Quantitative freeze-fracture analysis of the frog neuromuscular junction synapse. I. Naturally occurring variability in active zone structure. J Neurocytol 27: 361–377, 1998.

Peled ES, Newman ZL, Isacoff EY. Evoked and spontaneous transmission favored by distinct sets of synapses. Curr Biol 24: 484–493, 2014.

Phillips GR, Huang JK, Wang Y, Tanaka H, Shapiro L, Zhang W, Shan WS, Arndt K, Frank M, Gordon RE, Gawinowicz MA, Zhao Y, Colman DR. The presynaptic particle web: ultrastructure, composition, dissolution, and reconstitution. Neuron 32: 63–77, 2001.

Propst JW, Herrera AA, Ko CP. A comparison of active zone structure in frog neuromuscular junctions from two fast muscles with different synaptic efficacy. J Neurocytol 15: 525–534, 1986.

Propst JW, Ko C-P. Correlations between active zone ultrastructure and synaptic function studied with freeze-fracture of physiologically identified neuromuscular junctions. J Neurosci 7: 3654–3664, 1987.

Pumplin DW, Reese TS, Llinás, R. Are the presynaptic membrane particles the calcium channels? Proc Natl Acad Sci USA 78: 7210– 7213, 1981.

Rash JE, Ellisman MH. Studies of excitable membranes I. Macromolecular specializations of the neuromuscular junction and the nonjunctional sarcolemma. J Cell Biol 63: 567– 586, 1974.

Rizzoli SO, Betz WJ. Synaptic vesicle pools. Nat Rev Neurosci 6: 57–69, 2005.

Robitaille R, Adler EM, Charlton MP. Strategic location of calcium channels at transmitter release sites of frog neuromuscular synapses. Neuron 5: 773–779, 1990.

Rollenhagen A, Sätzler K, Rodríguez EP, Jonas P, Frotscher M, Lübke JHR. Structural determinants of transmission at large hippocampal mossy fiber synapses. J Neurosci 27: 10434–10444, 2007.

Ruiz R, Cano R, Casañas JJ, Gaffield MA, Betz WJ, Tabares L. Active zones and the readily releasable pool of synaptic vesicles at the neuromuscular junction of the mouse. J Neurosci 31: 2000–2008, 2011.

Sabatini BL, Regehr WG. Timing of neurotransmission at fast synapses in the mammalian brain. Nature 384: 170–172, 1996.

Sabatini BL, Regehr WG. Timing of synaptic transmission. Annu Rev Physiol 61: 521–542, 1999.

Sätzler K, Söhl LF, Bollmann JH, Borst JG, Frotscher M, Sakmann B, Lübke JH. Three-dimensional reconstruction of a calyx of Held and its postsynaptic principal neuron in the medial nucleus of the trapezoid body. J Neurosci 22: 10567–10579, 2002.

Scimemi A, Diamond JS. The number and organization of Ca^{2+} channels in the active zone shapes neurotransmitter release from Schaffer collateral synapses. J Neurosci 32: 18157–18176, 2012.

Shahrezaei V, Cao A, Delaney KR. Ca^{2+} from one or two channels controls fusion of a single vesicle at the frog neuromuscular junction. J Neurosci 26: 13240–13249, 2006.

Sheng J, He L, Zheng H, Xue L, Luo F, Shin W, Sun T, Kuner T, Yue DT, Wu LG. Calcium-channel number critically influences synaptic strength and plasticity at the active zone. Nat Neurosci 15: 998–1006, 2012.

Shon KJ, Olivera BM, Watkins M, Jacobsen RB, Gray WR, Floresca CZ, Cruz LJ, Hillyard DR, Brink A, Terlau H, Yoshikami D. mu-Conotoxin PIIIA, a new peptide for discriminating among tetrodotoxin-sensitive Na channel subtypes. J Neurosci 18: 4473–4481, 1998.

Sippy T, Cruz-Martín A, Jeromin A, Schweizer FE. Acute changes in short-term plasticity at synapses with elevated levels of neuronal calcium sensor-1. Nat Neurosci 6: 1031–1038, 2003.

Smith DO. Muscle-specific decrease in presynaptic calcium dependence and clearance during neuromuscular transmission in aged rats. J Neurophysiol 59: 1069–1082, 1988.

Sosa MA, Zengel JE. Use of mu-conotoxin GIIIA for the study of synaptic transmission at the frog neuromuscular junction. Neurosci Lett 157: 235–238, 1993.

Srinivasan G, Kim JH, von Gersdorff H. The pool of fast releasing vesicles is augmented by myosin light chain kinase inhibition at the calyx of Held synapse. J Neurophysiol 99: 1810–1824, 2008.

Stanley EF. The nanophysiology of fast transmitter release. Trends Neurosci 39: 183–197, 2016.

Stanley EF, Reese TS, Wang GZ. Molecular scaffold reorganization at the transmitter release site with vesicle exocytosis or botulinum toxin C1. Eur J Neurosci 18: 2403–2407, 2003.

Stiles JR, Bartol TM. Monte Carlo methods for simulating realistic synaptic microphysiology using MCell. In: Computational Neuroscience: Realistic Modeling for Experimentalists, edited by De Schutter E, editor. Boca Raton, FL: CRC, 2001, p. 87–127.

Stiles JR, Van Helden D, Bartol TM, Salpeter ES, Salpeter MM. Miniature endplate current rise times less than 100 microseconds from improved dual recordings can be modeled with passive acetylcholine diffusion from a synaptic vesicle. Proc Natl Acad Sci USA 93: 5747–5752, 1996.

Tabares L, Ruiz R, Linares-Clemente P, Gaffield MA, Alvarez de Toledo G, Fernandez-Chacón R, Betz WJ. Monitoring synaptic function at the neuromuscular junction of a mouse expressing synaptopHluorin. J Neurosci 27: 5422–5430, 2007.

Tank DW, Regehr WG, Delaney KR. A quantitative analysis of presynaptic calcium dynamics that contribute to short-term enhancement. J Neurosci 15: 7940– 7952, 1995.

Tarr TB, Dittrich M, Meriney SD. Are unreliable release mechanisms conserved from NMJ to CNS? Trends Neurosci 36: 14–22, 2013b.

Tarr TB, Malick W, Liang M, Valdomir G, Frasso M, Lacomis D, Reddel SW, Garcia-Ocano A, Wipf P, Meriney SD. Evaluation of a novel calcium channel agonist for therapeutic potential in Lambert-Eaton myasthenic syndrome. J Neurosci 33: 10559–10567, 2013a.

Taschenberger H, Leão RM, Rowland KC, Spirou GA, von Gersdorff H. Optimizing synaptic architecture and efficiency for high-frequency transmission. Neuron 36: 1127–1143, 2002.

Tejero R, Lopez-Manzaneda M, Arumugam S, Tabares L. Synaptotagmin-2, and -1, linked to neurotransmission impairment and vulnerability in spinal muscular atrophy. Hum Mol Genet 25: 4703–4716; 2016.

Trussell LO, Grinnell AD. The regulation of synaptic strength within motor units of the frog cutaneous pectoris muscle. J Neurosci 5: 243– 254, 1985.

Urbano FJ, Piedras-Rentería ES, Jun K, Shin HS, Uchitel OD, Tsien RW. Altered properties of quantal neurotransmitter release at endplates of mice lacking P/Q-type Ca^{2+} channels. Proc Natl Acad Sci USA 100: 3491–3496, 2003.

Verma V, Reese TS. Structure and distribution of neuromuscular junctions on slow muscle fibers in the frog. Neuroscience 12: 647– 662, 1984.

von Gersdorff H, Borst JG. Short-term plasticity at the calyx of Held. Nat Rev Neurosci 3: 53–64, 2002.

Wachman ES, Poage RE, Stiles JR, Farkas DL, Meriney SD. Spatial distribution of calcium entry evoked by single action potentials within the presynaptic active zone. J Neurosci 24: 2877–2885, 2004.

Walrond JP, Reese TS. Structure of axon terminals and active zones at synapses on lizard twitch and tonic muscle fibers. J Neurosci 5: 1118–1131, 1985.

Wang LY, Augustine GJ. Presynaptic nanodomains: a tale of two synapses. Front Cell Neurosci 8: 455, 2015.

Wang LY, Neher E, Taschenberger H. Synaptic vesicles in mature calyx of Held synapses sense higher nanodomain calcium concentrations during action potential-evoked glutamate release. J Neurosci 28: 14450–14458, 2008.

Wang X, Pinter MJ, Rich MM. Ca^{2+} dependence of the binomial parameters p and n at the mouse neuromuscular junction. J Neurophysiol 103: 659–666, 2012.

Wang X, Wang Q, Engisch KL, Rich MM. Activity-dependent regulation of the binomial parameters p and n at the neuromuscular junction in vivo. J Neurophsyiol 104: 2352– 2358, 2010.

Wood SJ, Slater CR. The contribution of postsynaptic folds to the safety factor for neuromuscular transmission in rat fast and slow-twitch muscles. J Physiol 500: 165– 176, 1997.

Wood SJ, Slater CR. Safety factor at the neuromuscular junction. Prog Neurobiol 64: 393–429, 2001.

Wright SN, Brodwick MS, Bittner GD. Presynaptic calcium currents at voltage-clamped excitor and inhibitor nerve terminals of crayfish. J Physiol: 496, 347– 361, 1996,

Wu WH, Cooper RL. Physiological recordings of high and low output NMJs on the crayfish leg extensor muscle. JoVE 45: 2319, 2010.

Wyatt RM, Balice-Gordon RJ. Heterogeneity in synaptic vesicle release at neuromuscular synapses of mice expressing synaptopHluorin. J Neurosci 28: 325–335, 2008

Yamada WM, Zucker RS. Time course of transmitter release calculated from simulations of a calcium diffusion model. Biophys J 61: 671– 682, 1992.

York AL, Zheng JQ. Super-resolution microscopy reveals a nanoscale organization of acetylcholine receptors for trans-synaptic alignment at neuromuscular synapses, eNeuro 4, 2017.

Zhai RG, Bellen HJ. The architecture of the active zone in the presynaptic nerve terminal. Physiology 19: 262– 270, 2004.